Freie Universität Berlin

Transient reflectivity and coherent phonon excitation: An ultrafast probe of the metal-to-insulator transition in VO_2

Diplomarbeit

Laura Foglia

February 2011

Per la stessa ragione del viaggio, viaggiare.

ANIME SALVE - FABRIZIO DE ANDRÉ

This work has been performed in the Electron dynamiχ group

at the Physical Chemistry department

of the Fritz-Haber-Institut der Max-Planck-Gesellschafft.

Contents

List of Figures

Introduction

How many applications can you imagine for a material which is able to switch from insulator to metallic and viceversa on an ultrafast timescale? There is a lot of space for imagination: depending on how the transition between the different states is driven, for example by an electric field, one may think about ultrafast electronic switches. Temperature or pressure sensors could be designed by making use of the transition driven by heat or strain. In the case of a light-driven transition, the material could be used for building, for example, light sensors or modulators.

One example for such a material is given by VO_2. At room temperature, VO_2 is an insulator with a monoclinic lattice structure. It undergoes a reversible, first-order transition to a metallic state at 340 K. The metal-to-insulator transition is also associated with a structural distortion: the high temperature phase has a tetragonal (rutile) structure. The fact that the transition occurs close to the room temperature and is reversible, makes it an ideal candidate for the practical applications.

However, the interest in vanadium dioxide goes beyond the applied research. Ever since the discovery of its phase transition by Morin in 1959 [Mor59], VO_2 has been at the center of a controversy regarding the nature of the transition istelf. The issue is whether the lattice distortion is responsible of opening the insulating gap or the correlation effects alone are enough to drive the electronic transition, which is eventually followed by a lattice distortion. Both Peierls and Mott-Hubbard mechanisms have been proposed and vanadium dioxide historically became the prototype system for those materials where the competition between electronic localization and delocalization plays a crucial role

The discovery of the photoinduced phase transition [RB71] in VO_2 has allowed to perform pump-probe experiments on it, in order to adress the dynamics of the elec-

tronic and lattice components separately, and on an ultrafast timescale. Here, light is used both as a way to excite the system and a tool to probe the effects of this perturbation. However, all time-resolved experiments up to date still disagree in determining the leading mechanism of the transition, although they agree that the metal-to-insulator transition and the structural distortion do not occur on the same timescale [CDC+04, KLK+06, KEH+07, Bau07]. Thus, the long-lasting controversy still persists.

We tackle the problem by studying the coherent response of the lattice, which exhibits itself as a modulation of the measured transient reflectivity signal. The technique combines the intrinsic sensitivity of the phonon modes to the crystal symmetry with the femtosecond time resolution of the pump-probe experiments. This allows us to detect the fastest lattice dynamics, in opposite to the previous experiments probing the lattice, which only have a resolution of hundreds of picoseconds [CTS+01, Bau07].

The pump induced change on the reflectivity has been measured as a function of the excitation fluence. Both the incoherent background and the superimposed coherent response show a change in the dynamics across the phase transition (Sec. 3.1.1 and 3.1.2). Studying the dynamics of the coherent phonons we address the changes in symmetry occurring at the transition and show that the phonons spectrum is dramatically modified. To describe the results we propose a model where the ultrafast change in the lattice potential is due to the forces exerted by the excited electrons, long before the ions have moved to the positions of the rutile phase. To corroborate our hypothesis we perform a pump-pump-probe experiment. The obtained results demonstrate that, at least for the photoinduced transition, the excited electrons are sufficient to cause the change in the lattice potential.

The thesis is structured as follows: In chapter 1 I first outline the theoretical models for the metal-to-insulator phase transition, giving great attention to the photoinduced transitions. Then I consider in detail the response of a material to an incident electromagnetic field and explain the experimental methods used in our work: transient reflectivity and coherent phonon excitation. Finally, the chapter presents VO_2 and the controversy around its transition. To perform the experiment we use a femtosecond

laser system as a light source, which is described in 2.1, and was constructed within the framework of my diploma thesis. To improve our setup I've been working on the construction of a continuously variable *switchbox*, an optical setup described in appendix B. Chapter 2 also includes a brief description of the sample and of the experimental setup. Finally, chapter 3 reports the experimental results and their discussion.

1 Theoretical Background

This chapter begins with a description of the most important models for the metal-to-insulator transition: the Peierls and the Mott-Hubbard models. A particular attention is given to the possibility of driving the transition with light. The response of a medium to the presence of an electromagnetic field is considered in detail, focusing on the most important models of the dielectric tensor. Light is not only a way of perturbing a system but it is also a tool to probe the effects of the perturbation. From this point of view I describe the experimental methods employed in our experiments, transient reflectivity and coherent phonon excitation. Finally, the chapter presents vanadium dioxide and the controversy around the nature of its transition. Besides describing its structural, electronic and optical properties, I focus on the theoretical and experimental state-of-the-art methods, with a major emphasis on the recent work on the photoinduced phase transition.

1.1 Metal-to-Insulator Transition

Regarding to their conduction properties, materials are usually divided into four categories: metals, semimetals, semiconductors, and insulators. This distinction arises from a basic band theory approach, implying that electrons are moving in a periodic field and can be treated independently.
In this case, the solutions of the Schrödinger equation are of the Bloch form,

$$\Psi_{\mathbf{k}}(\mathbf{r}) = e^{i\mathbf{kr}} \cdot u_{\mathbf{k},n}(\mathbf{r}) \ ,$$

where $u_{\mathbf{k},n}(\mathbf{r})$ is a periodic function with the period of the lattice. The $\mathbf{k}$ vector is defined only within a Brillouin zone, labelled by the index n. The corresponding energy $\epsilon_n(\mathbf{k})$ is a continuous function of $\mathbf{k}$ for a given value of n. Given two possible spin orientations, every band consists of $2N$ independent states, with N being the number of unit cells.

The energy $\epsilon_n(\mathbf{k})$ is plotted in figure 1.1 in dependence of $\mathbf{k}$.

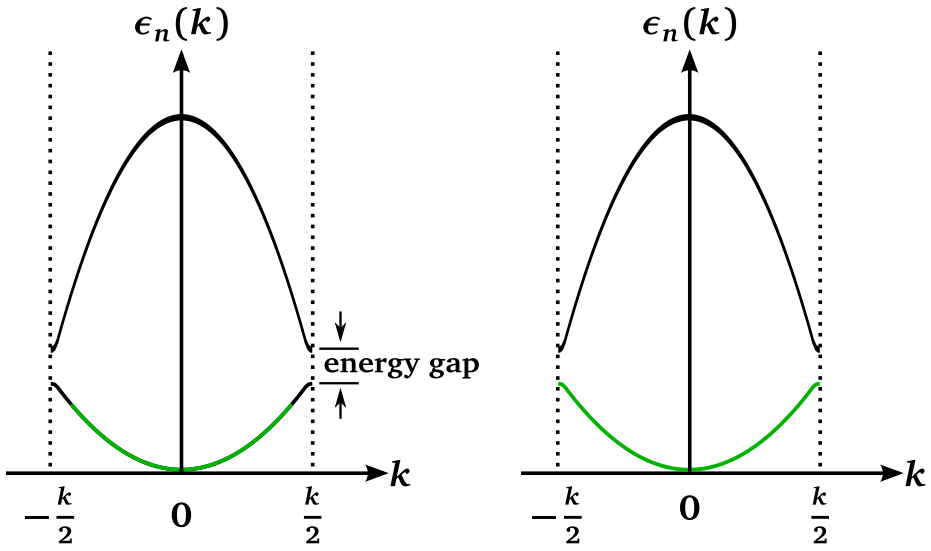

Figure 1.1: Energy levels following from the band theory displayed in the *reduced-zone scheme*. The green curve represents occupied states in the case of a metal (*left*) and of an insulator (*right*).

In 1931 Wilson described the difference between conductors, semiconductors and insulators at $T = 0$ [Wil31]. If the valence electrons fill the bands completely, as the green curve indicates in the right panel of figure 1.1, the material is an insulator, while if the bands are partially filled (figure 1.1, left panel) just a small perturbation is required to excite electrons from the valence to the conduction band and the material is a metal.

However, there is a class of materials, that, according to Wilson's scheme, are predicted to be metals but turn out to be insulators, although their conductivity can be increased by several orders of magnitude by chemical doping. For example this is the case for many antiferromagnetic oxides with partially filled d-shells, such as NiO [BV37]. In 1934 Wigner was one of the first to stress the importance of electron-electron interaction for the problem, suggesting that at low densities a free-electron gas crystallizes in a non-conducting state in order to magnify mutual separation between the electrons [Wig34].

It is worth noting that even in the approximation of non interacting electrons, a metal-to-insulator transition (MIT) can occur. This happens when the specific volume of an alloy changes in such a way that two bands cease to overlap, resulting in a full valence band and an empty conduction band. A good example is bismuth, which becomes an insulator under high pressure [SJ64].

1.1.1 The Peierls Transition

Bismuth presents another peculiarity: its lattice structure is close to the simple cubic one, but with every second atom a little displaced along the space diagonal and with the angle between the axes slightly different from 90 degree. Such a structure has the symmetry of the *fcc* Bravais lattice with two atoms in the unit cell. In 1934 Jones presented a picture where most of the states inside the Brillouin zone are occupied and most of the states outside are empty, i.e. the Fermi surface almost coincides with the Brillouin zone boundary [Jon34]. The displacement is therefore favoured by reduction of the total electron energy. If the coincidence of Fermi surface and zone boundary were exact, the valence band would be completely empty and the alloy would be an insulator. This is the concept behind the Peierls transition, after the name of the theoretician who first discussed it in 1955 [Pei55]. Peierls showed that a 1D half filled metal is unstable against a structural distortion.

Figure 1.2 (a) shows a one-dimensional lattice of period a and its dispersion relation. Supposing that each unit cell contributes with one valence electron, the band is half-filled and the material is a metal. We consider now that the lattice is distorted in such a way that the atoms pair and the lattice constant doubles, as shown in Figure 1.2 (b). Doubling of the lattice periodicity implies halving of the Brillouin zone and opening of a gap at $k = \frac{\pi}{2a} = k_F$. Hence the Fermi level resides in the middle of the gap and the material becomes an insulator. Peierls demonstrated that the elastic energy required to induce the distortion is smaller than the energy reduction for the electrons at the Fermi surface, which makes the insulating phase more stable. In a later book he also

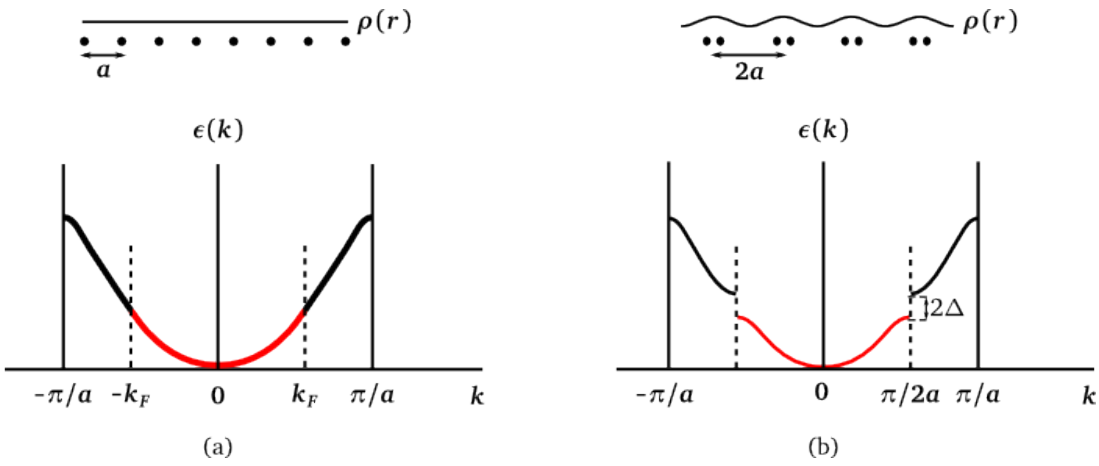

Figure 1.2: The Peierls distortion in a 1D lattice.
(a) The dispersion relation of the electrons in a lattice with period a. A half-filled band implies that the Fermi level lies in the middle of the band and the material is metallic. (b) The distortion induces halving of the Brillouin zone; E_F lies in the middle of a band gap and the material is insulator.

calculated the reduction in electronic energy to be proportional to the displacement δ as $E \propto -\delta^2 \log \delta$, for small values of δ [Pei91].

Evidence of the Peierls transition has been found in lattices with lower dimensionality, such as crystals consisting of linear chains of molecules, or in polymer chains and rings [LBB06]. In alloys of higher dimensionality one usually refers to the Peierls transition when the transition is triggered by the coupling of electronic degrees of freedom to vibrational levels of the system or when the opening of an energy gap is due to a lattice distortion.

1.1.2 The Mott-Hubbard Transition

As already mentioned in Section 1.1, the band theory may give incorrect predictions when applied to materials with strong electronic correlations. This kind of systems, which are referred to as *strongly correlated electron systems*, cannot be described in terms of non-interacting entities since many-body interactions play a crucial role. Ex-

amples are high-temperature superconductors, spin Peierls materials, Mott insulators, and other materials exhibiting unusual charge ordering, magnetic phenomena, or temperature-induced phase transitions. Discussing insulating properties of NiO, Mott and Peierls first pointed out that the Coulomb repulsion between electrons is able to prevent them from moving, thereby leading to the low conductivity observed [MP37].

Consider a cubic lattice of one-electron centres, which, according to the Wilson model, is a metallic conductor with a half-filled band, for all values of the interatomic distance b. Without electron-electron interactions the band solely originates from the overlap of the atomic orbitals. In this picture, if the overlap is small, i.e. for large values of b, conduction is expected only if one or more electrons are missing. On the other hand, if all electrons are localized at their sites close to the ions, the minority which happens to tunnel through the barrier finds itself on already occupied ions. This excited state of the system, with the electron-hole pair residing on neighbouring sites, is energetically unfavorable and the electron is rapidly attracted back by the Coulomb potential of the positive ion. Conductivity is therefore possible only if the energy given to the system suffices to overcome the attraction of the hole, thereby generating two stable free carriers. In the limit of an infinite distance between atomic sites, the energy needed for this is $\mathscr{W} = \mathscr{I} - \mathscr{E}$, where $\mathscr{I}$ is the ionization energy and $\mathscr{E}$ is the electron affinity.

On the other hand, if some of the pairs are already formed, current can be carried and no work is needed to create new electron-hole pairs. In this case the electron feels the screened Coulomb potential:

$$V(r) = -\frac{e^2}{kr} e^{-qr} \,, \qquad \text{with} \quad q^2 = \frac{4me^2 n^{1/3}}{k\hbar^2} \,,$$

and depends on the concentration n of free carriers.

In his model, Mott predicts the existence of a critical value of the lattice constant $b = b_0$ at which, at least at zero temperature, the number of free carriers increases discontinuously to the value corresponding to a metallic lattice [Mot61]. This idea is schematically illustrated in Figure 1.3, where the energy bands of the system are

reproduced as a function of the interatomic distance b. For large values of b the system is an insulator and the width of the band gap corresponds to the activation energy $\mathscr{W}$. Once the critical distance is reached, the bands overlap and the system becomes metallic.

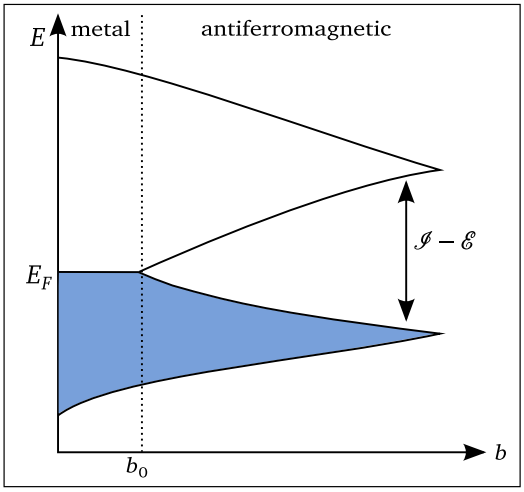

Figure 1.3: Energy bands of a system in the Mott model, as a function of the interatomic distance b. For large distances the width of the bandgap is reported. The metal to insulator transition occurs at b_0.

One of the first, and probably the most famous approach to the theoretical description of strongly correlated systems is the Hubbard model, formulated by John Hubbard in the 1960s [Hub63, Hub64a, Hub64b]. The basic idea of the Hubbard model is as follows. Electrons can hop between sites, representing atoms ordered in a crystalline pattern. An additional repulsion term accounts for the Coulomb interaction between two electrons of different spin within the same lattice site. For simplicity, interactions between electrons on different atoms are neglected and only electrons on the s-orbitals are considered. The Hamiltonian of this simplified model can be written as:

$$H = \sum_{i,j}\sum_{\sigma} t_{ij} c^{\dagger}_{i,\sigma} c_{j,\sigma} + T_0 \sum_{i,\sigma} n_{i,\sigma} + \frac{1}{2} U \sum_{i,\sigma} n_{i,\sigma} n_{i,-\sigma} \tag{1.1}$$

where $n_{i\sigma} = c^{\dagger}_{i\sigma} c_{i\sigma}$ is the number operator for electrons in the site i with spin σ and the summations are over all states and spins. Here $t_{i,j}$ is the hopping matrix, responsible for the motion of electrons between different atoms, T_0 determines the atomic binding energy, and U the intra-atomic correlation energy, related to the Coulomb repulsion. The Hubbard model is described in detail in Appendix A.

At a first sight it can be noticed that in the limit of $t_{ij} >> U$ the interaction between electrons can be neglected and the model reduces to the tight-binding case with de-

localized electrons, giving rise to the band structure. In the opposite limit, $t_{ij} << U$, the electron interaction term dominates and the electrons are localized on their lattice sites (Fig 1.4).

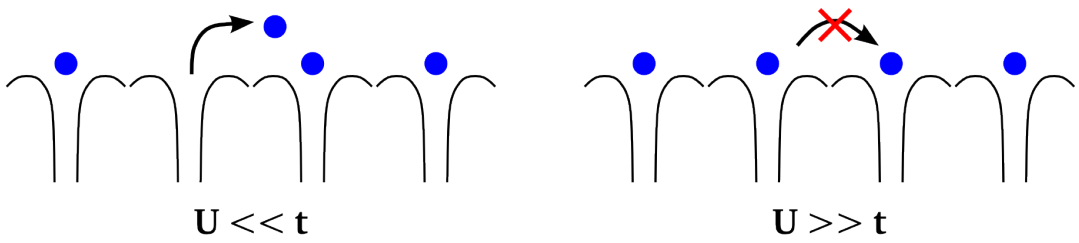

(a) (b)

Figure 1.4: Schematic illustration of the Hubbard model. (a): the hopping term dominates and the electrons are delocalized (b) the electrons are localized on their atomic sites by the Coulomb interaction

Hubbard demonstrated that for given values of the bandwidth W and of the interaction energy U the nature of the solutions for the electron energy is determined by the ratio $\frac{W}{U}$ rather than by their values separately and that the spectrum consists of one or two bands depending on this ratio [Hub64b]. In particular, there is a critical value of $\frac{W}{U}$ at which the spectrum splits. For values less than the critical one, one band is full and another one empty, leading to the insulator behaviour in the solid, while higher values of $\frac{W}{U}$ lead to metallic attributes. In the very special case of a half-filled band with s-character the critical value is given by $\Delta/U = 1.1547$.

It is worth noting that the Mott the Hubbard models lead to the same behaviour of the energy spectrum. The difference between the two models is that Mott predicts a discontinuity at the transition, while Hubbard does not. In fact the theory of Hubbard neglects the long-range interaction, which, in the Mott model, is responsible for the sharpness of the transition.

The theory of Mott and Hubbard presented in the previous section imposes that there is a critical carrier density for which the electrons in a band are able to screen the

Coulomb attraction of the atom, leading to a delocalized distribution. There are several key parameters of the system which can be controlled experimentally in order to alter the carrier density. In the Hubbard Hamiltonian, Eq. (1.1), these are the electron correlation strength, given by the ratio $\frac{U}{t}$, and the band filling n.

Figure 1.5 shows a schematic metal-insulator phase diagram in terms of these parameters. Excluding degeneracies, the cases of $n = 0$ and $n = 2$, corresponding to a completely empty or filled band, stay for a band insulator. The $n = 1$ case is the one treated in detail by both Mott and Hubbard, where the transition is driven by changes of the electron correlation strength. The idea of Mott is that the carrier density decreases with increasing ratio U/t, until it reaches the critical carrier density where the long-range Coulomb forces are not screened anymore and electron-hole bound pairs are formed. In addition, the coupling between electronic and lattice degrees of freedom can discontinuously increase the transfer amplitude t_{ij}. Both mechanisms cause a first-order transition, which is called *bandwidth-control*-MIT (BC-MIT). In this process the Coulomb interaction U is kept almost unchanged, while the controlled parameter is the transfer interaction t_{ij}, and therefore the bandwidth W. Experimentally, the electron correlation strength can be controlled by modifications of lattice parameters or chemical composition, without altering the original lattice structure. The two possible methods are application of hydrostatic pressure or changing the chemical com-

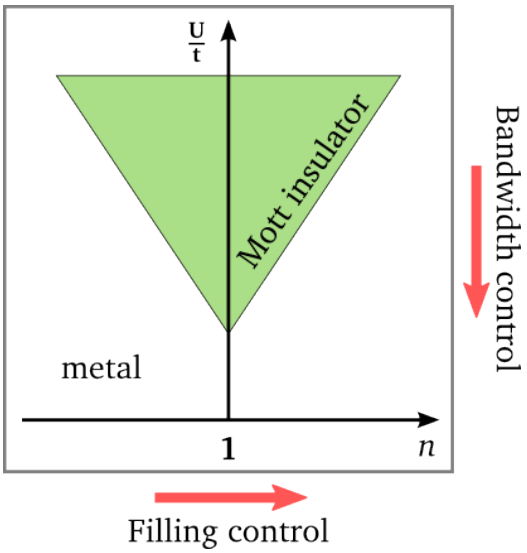

Figure 1.5: The phase diagram of the metal to insulator transition depending on the parameters $\frac{U}{t}$ and n. Control of the phase transition can be performed either by changing the correlation strength $\frac{U}{t}$ (bandwidth control-MIT) or by changing the number of free carriers in the band (filling control-MIT)

position with elements of the same valence. In the first case, the pressure shortens the interatomic distance, thereby increasing the transfer interaction. The drawback of this technique is that the structural changes induced by pressure are not so easy to determine, particularly in the case of materials with anisotropic compressibility, which significantly complicates quantitative understanding of the transition. In the second case, the substitution of an anion with another one of the same valence can change the orbital overlap, and consequently the bandwith, without affecting the band filling.

On the other hand, a system of 2N atoms having $(2N+1)$ electrons, i.e. non-integer band filling $(N+\frac{1}{2})$, is usually a metal. Therefore, an other possibility to control the MIT transition is to alter the band filling starting from the parent Mott insulator ($n = 1$). This kind of transition, called *filling-control*-MIT (FC-MIT), is not necessarily a first-order transition [IFT98]. The standard method to control the filling is to substitute the transition metal ion with another one of different valence, without distorting the lattice structure. Starting from the parent Mott insulator one refers to *hole doping* if the band filling is decreased and to *electron doping* if it is increased, irrespective of the nature of the charge carriers. For example, band filling control has been successfully applied to perovskite and related compounds, where the structure is relatively resistant to chemical modification of the larger cation site and therefore a wide range of fillings can be achieved. Similar effects can be obtained with altered stoichiometry of the original composition of the parent compound. Usually oxygen nonstoichiometry is used, since it allows to accurately vary the filling by means of post-annealing procedures under oxidizing atmosphere.

The biggest disadvantage of both BC-MIT and FC-MIT, which imply that the chemical composition or the lattice structure of the compound are altered *a priori*, is the irreversibility of the changes produced. Furthermore, the changes in the parameters cannot be observed dynamically while they occur, but rather their consequences are monitored.

1.1.3 The photoinduced transition

The previous section (1.1.2) discusses how to induce a metal-to-insulator transition by modifying the chemical composition or the structure of the compound. This implies an irreversible change to the properties of the material and the impossibility of observe the dynamics of the process. A powerful technique to study the transition without causing any permanent changes to the material, is to employ short intense laser pulses. In metals and semiconductors visible light interacts mostly with electrons, photo-exciting them to states above the Fermi energy. The excitation energy is distributed among other electrons by electron-electron scattering until a Fermi-Dirac distribution with temperature T_e is formed. Typical timescales of electron thermalisation are in the range of 10 to 1000 fs, after which the system ends up in a state where the electrons and the lattice have different temperatures, as described by the *two-temperature-model* [AKP74]. The exceeding energy is transferred from the electrons to the lattice by means of electron-phonon scattering and the resulting phonon distribution is a Bose-Einstein distribution with temperature T_{ph}. This energy transfer between the electron and the phonon bath goes on until the two reservoirs have the same temperature, typically within 0.1 to 10 ps. The two processes, electron-electron and electron-phonon scattering, are not subsequent, but simultaneous and phonons are emitted even before the electrons are thermalised. In addition, the electronic system can couple to other degrees of freedom. For example the coupling to the spin bath can lead to magnetic effects. Finally, also transport effects are present and can contribute to reduction the system temperature, on a timescale of more than 1 ps.

In metals the electron-hole recombination at the Fermi level can occur via phonon emission. This is not possible in insulators or semiconductors since most of the times the band gap is larger than typical phonon energies. Consequently, recombination in semiconductors occurs on much longer timescales, about 1 ns. In the meantime electrons and holes thermalize separately and reach the thermal equilibrium with the lattice [Kam06].

Due to the interaction with light a system can eventually end up in a macroscopic excited domain that has new structural and electronic orders quite different from the initial equilibrium phase. This process is called *photoinduced phase transition* (PIPT). Different mechanisms can induce the PIPT:

Purely Electronic Interaction Intense photo-excitation induces a change in the electron distribution such that the critical amount of carriers in the valence band is reached. Then, according to the Mott model, the band gap collapses and the system becomes metallic. In this picture the transition occurs, in terms of the potential, even before the electron and lattice temperature reach the equilibrium. For example this scenario is the one observed for the photo-excitation of the insulating phase of 1 T−TaS_2 [PLL+08].

Electron-Phonon Interaction A lattice instability related to phonon softening can be caused by the strong coupling of the electrons to few specific phonon modes [VS83]. The distortion of the nuclear structure is often associated to a modulation of the charge density, referred to as charge density wave (CDW). The electrons are periodically localized and therefore their dispersion gets flatter, corresponding to a reduced bandwidth. In this scenario the lattice vibration triggers the MIT by enhancing the amplitude of the CDW and consequently reducing the bandwidth. The coupling of lattice and electronic degrees of freedom seems to be responsible, for example, for the transition from the commensurate-CDW to the nearly commensurate-CDW of 1 T−TaS_2 reported by [HBS+10]. Electronic transition which are induced by a structural distortion are often referred to as *Peierls-like transitions*.

Electron-Spin Interaction Rapid increase of temperature of the electronic system is considered to be responsible for most of the demagnetisation processes in $3d$ and $4f$ ferromagnets as well as in binary alloys such as FeRh [RSP+10]. In this mechanism the electronic temperature, which can reach some thousands of K, overcomes the Curie temperature of the system within few hundreds of fs after

laser excitation. The subsequent excitation of the magnetic system is therefore purely thermically driven.

Coherent Phonons Generation As considered before, the lattice-driven transitions are often due to selective coupling of the electronic system to very specific phonon modes. In the coherent manipulation picture the transition is triggered by the direct excitation of the phonon mode, leaving the electronic system in its ground state. This kind of mechanism has been reported for the first time by Rini and co-workers in a manganite [RTD+07]. They observe an ultrafast transition from the stable insulating phase to a metastable metallic phase of a magnetoresistive manganite via direct excitation of a phonon mode at 17 THz It is still not clear whether the specific excited mode is directly responsible for the transition or if the redistribution of vibrational energy leads to the excitation of other modes which may strongly influence the electron charge distribution.

Requisite for the occurrence of a PIPT is an excited state of the system, whose free energy takes a local minima separated from the global one by substantial energy barriers.

Let us consider the potential energy curves drawn in Figure 1.6. The low potential curve has two local minima, $|g\rangle$ and $|f\rangle$, separated by a potential barrier. $|f\rangle$ is referred to as the high energy equilibrium phase and can be reached from $|g\rangle$ via thermal excitation. The potential curve of the excited states also shows two local minima. The one being directly above the ground state will be referred to as the intermediate state $|i\rangle$ and can be reached via a Franck-Condon transition (black arrow) from $|g\rangle$. The energy of $|i\rangle$ is higher than the one of the second local minima, which in this scheme represents the long lived non-equilibrium state related to the photoinduced phase and will be referred to as $|p\rangle$.

The relaxation of the system from $|i\rangle$ to $|p\rangle$, indicated by the green arrow, involves at least one of the mechanisms described above. From the photoinduced state the system finally relaxes to one of the equilibrium states. This final process occurs usually via heat transfer and therefore on the ps timescale.

Referring to photoinduced phase transitions, an important consideration has still to be made. Often the macroscopic properties of the photoinduced phase, such as color, lattice structure, magnetic properties, as well as the absorption and reflection spectra, are similar to the ones of the high energy equilibrium phase. Nevertheless it has been demonstrated that the photo-induced phase is a different macroscopic phase [TT01]. Furthermore, because of their nonequilibrium nature, photoinduced phases can show interactions which are normally hidden in the equilibrium phases.

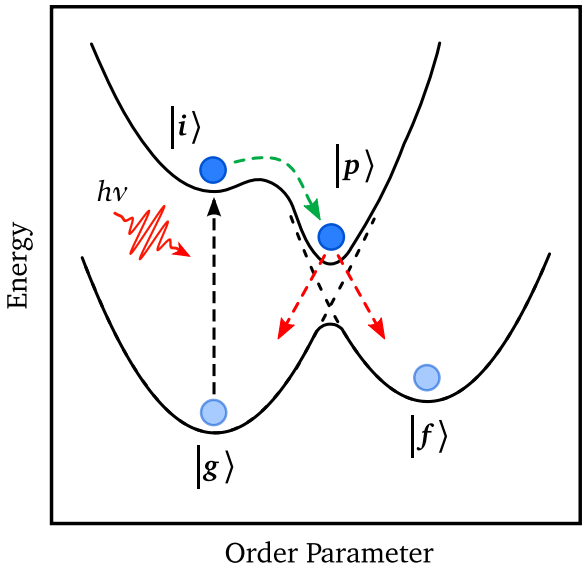

Figure 1.6: $|g\rangle$ and $|f\rangle$ are the low-energy and high-energy equilibrium states, respectively. $|i\rangle$ is an intermediate excited state and $|p\rangle$ is the long lived non-equilibrium state related to the PIPT

Therefore, it is important to remark that the metallic state I refer to below is the photo-induced metallic phase and does not necessarily coincide with the metallic phase which can be reached by heating the sample.

1.2 Light as a perturbation source and a detection instrument

When light interacts with matter, the relevant material property coupling to the radiation field is the polarization **P**, which is generally represented in the form

$$\mathbf{P} = \mathbf{P}^{(1)} + \mathbf{P}^{(2)} + \mathbf{P}^{(3)} + \cdots = \mathbf{P}^{(1)} + \mathbf{P}_{NL} \tag{1.2}$$

For weak electric fields, it can be considered as a linear function of the field magnitude. However, in the case of intense fields, such as short laser pulses, higher orders must be also considered. Processes related to $\mathbf{P}_{NL}$ are referred to as *nonlinear optics* (cf. Sec. 1.2.6).

The interaction of a variable electromagnetic with matter greatly depends on frequency and on the material considered. In a dielectric, the electric field moves the bound charges, inducing a local electric dipole moment. The macroscopic density of induced and permanent dipole moments is expressed in terms of the polarization **P**, whose divergence is related to the density of charges in the material. The electric displacement field in the material is therewith defined as

$$\mathbf{D} \equiv \epsilon_0 \mathbf{E} + \mathbf{P} \quad \Rightarrow \quad D_i = \sum_j \epsilon_{ij} E_j \,, \tag{1.3}$$

where the dielectric permittivity ϵ_{ij} is a symmetrical tensor of rank two. In a metal the presence of an electric field generates a current. The relation between the field and the current depends on the properties of the conductor but can be supposed to be linear for the majority of cases:

$$j_i = \sum_j \sigma_{ij} E_j,$$

where σ_{ij} is a symmetrical tensor of rank two, the conductivity tensor.

At this point it is useful to define some quantities which will frequently occur in this

work:

the relative permittivity	ϵ_r	$\mathbf{D} = \epsilon_0 \epsilon_r \mathbf{E}$	(1.4a)
and the susceptibility	χ	$\mathbf{P} = \epsilon_0 \chi \mathbf{E}$	(1.4b)
which are related by		$\epsilon_r = 1 + \chi$	(1.4c)

The following discussion will be restricted to isotropic materials, where ϵ and σ are scalar functions, and is equally applicable to metals and dielectrics: at optical and higher frequencies there is even no quantitative difference between the properties of metals and dielectrics [LL60]. At these frequencies the setting up of electric polarization is much slower than the changes in the electromagnetic field and the value of **D** depend generally on $\mathbf{E}(t)$ at every previous instant.

Assuming that any dependence on **H** can be neglected, the relation between the dispersion field **D** and the electric field **E** is given by

$$\mathbf{D}(t) = \mathbf{E}(t) + \int_0 f(t)\mathbf{E}(t-\tau)d\tau \tag{1.5}$$

By expressing the field in terms of a series of single frequency components by Fourier expansion, the relation (1.5) can be written as

$$\mathbf{D} = \epsilon(\omega)\mathbf{E} = \epsilon_0 \epsilon_r \mathbf{E} \tag{1.6}$$

where the dielectric permittivity $\epsilon(\omega)$ completely describes the properties of the system and its response to the external field. It is a complex quantity, depending on the frequency and on the properties of the medium, and is defined as

$$\epsilon(\omega) = \epsilon_1(\omega) + i\epsilon_2(\omega) = 1 + \int_0^\infty f(\tau)e^{iw\tau}d\tau \tag{1.7}$$

A macroscopic interpretation of the imaginary part of $\epsilon(\omega)$ can be given by applying the Poynting theorem. The time-averaged absorbed power Π in a volume V of an isotropic medium is given by

$$\left\langle \frac{d\Pi}{dV} \right\rangle = \langle \mathbf{J} \cdot \mathbf{E} \rangle = \frac{1}{2}\omega \left|E_0\right|^2 \Im\mathfrak{m}[\epsilon(\mathbf{x},\omega)] + \frac{1}{2}\left|E_0\right|^2 \Re\mathfrak{e}[\sigma(\omega)] \ , \tag{1.8}$$

see App. C. This formula shows that absorption at a given frequency ω is determined by the imaginary part of the dielectric permittivity $\epsilon(\mathbf{x}, \omega)$ and by the real part of the conductivity $\sigma(\omega)$.

To calculate the dielectric permittivity theoretically and use it to determine the optical properties of a material is generally very complicated. Therefore, models are usually used to connect the microscopic properties of the material to the measurable quantities. They need to reproduce the typical optical properties of the materials. In particular, insulators and glasses show vibrational absorption at the infrared wavelengths and electronic absorption in the ultraviolet region, while they are colourless and transparent in the visible region. Metals, on the other hand, are highly reflective in the infrared and visible region, due to the presence of free carriers, while their typical color is due to electronic interband absorption. The next sections present two basic models based on the concept of the dipole oscillator. Three sorts of dipole oscillators can be distinguished in a solid: the ones due to bound electrons, the ones due to the vibration of charged atoms and finally the ones due to free electrons.

1.2.1 Dielectric function of a harmonic oscillator: the Lorentz model

The Lorentz model considers the electrons in a solid to be bound to the atoms by an elastic force. Their interaction with an monochromatic electromagnetic wave, $E(t) = E_0 \exp(-i\omega t)$, causes a displacement x from the equilibrium position governed by the equation of motion of a damped harmonic oscillator with resonance frequency ω_j and damping rate γ_j, where j labels the different atoms in the solid. The displacement of each electron gives a time-varying dipole moment, $p(t) = -ex$. If n is the electron density, the overall polarization is given by

$$\mathbf{P} = \left(\frac{ne^2}{\epsilon_0 m} \sum_j \frac{1}{\omega_j^2 - \omega^2 - i\gamma_j \omega} \right) \mathbf{E} \,, \tag{1.9}$$

The following expression for the relative dielectric permittivity $\epsilon_r(\omega)$ follows by applying Eq. (1.4b) and (1.4c):

$$\epsilon_r(\omega) = 1 + \frac{ne^2}{\epsilon_0 m} \sum_j \frac{1}{\omega_j^2 - \omega^2 - i\gamma_j \omega} \tag{1.10}$$

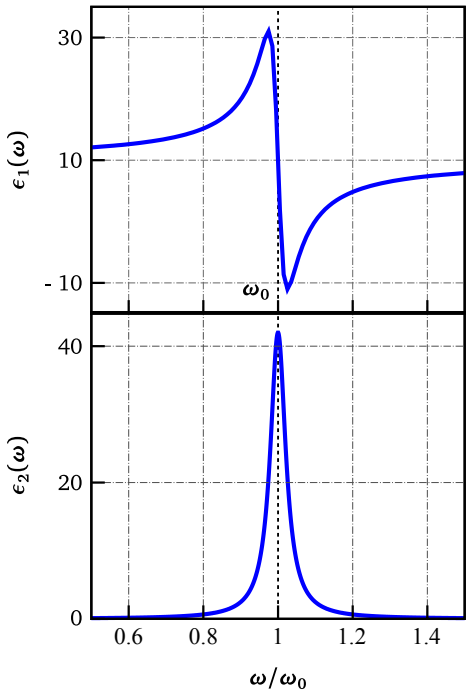

Figure 1.7: Frequency dependence of the real (*top*) and imaginary part (*bottom*) of the complex dielectric constant at frequencies close to resonance

Figure 1.7 shows the frequency dependence of ϵ_1 and ϵ_2 at frequencies close to the resonance. There is no significant absorption if the frequency is tuned far from resonance, since ϵ_2 peaks at ω_0 and has a linewidth of about γ. Instead, the dependence of ϵ_1 shows that there can still be a significant effect on the refractive index.

In a solid the individual atomic dipoles respond to a local field which is not necessarily the same as the external one. Considering this local field correction the dielectric constant assumes the form

$$\epsilon_r = 1 + \frac{\sum_j n_j \alpha_j}{\epsilon_0 + \frac{1}{3}\sum_j n_j \alpha_j} \tag{1.11}$$

where α_j is the polarization of an atom of type j.

1.2.2 Dielectric function of the free electrons: the Drude model

The electronic and atomic oscillators considered above are examples of bound oscillators. On the other hand, metals contain a large number of free electrons, which experience no restoring force when displaced. This section presents the so-called Drude model, referring to the author of the free electron model of metals.If the resonance frequency ω_0 is set to zero, the harmonic oscillator equation is still a good starting point.

By setting $\omega_0 = 0$ in Eq. (1.10), an expression for the relative permittivity in the Drude model is directly obtained:

$$\epsilon_r(\omega) = 1 - \frac{ne^2}{\epsilon_0 m}\frac{1}{(\omega^2 + i\gamma\omega)} = 1 - \frac{\omega_p^2}{(\omega^2 + i\gamma\omega)}\,, \tag{1.12}$$

where ω_p is the plasma frequency,

$$\omega_p^2 = \left(\frac{ne^2}{\epsilon_0 m}\right) \tag{1.13}$$

Otherwise, one could set $\omega_0 = 0$ in the equation of motion (See App. C), which leads to an expression for the AC conductivity

$$\sigma(\omega) = \frac{ne^2\tau}{m}\frac{1}{1 - i\omega\tau} \tag{1.14}$$

Eq. (1.14) and (1.12) are related to each other through (App. C)

$$\epsilon_r(\omega) = 1 + \frac{i\sigma(\omega)}{\epsilon_0\omega} \tag{1.15}$$

Equation (1.15) gives the expression of the dielectric function for metals, where the imaginary part is related to the conductivity.

The Drude model considers the electrons in the metal to be free and to accelerate in presence of an electric field, undergoing collisions within the characteristic scattering time τ, usually on the order of 10^{-14} s. Usual electron densities in metals are $n = 10^{28} \ldots 10^{29}\,\mathrm{m}^{-3}$, which are responsible for the high thermal and electrical conductivity. In the visible region $\omega \sim 10^{15}\,\mathrm{Hz} \gg \gamma$ and Eq. (1.12) can be symplified to

$$\epsilon_r(\omega) = 1 - \frac{\omega_p^2}{\omega^2}$$

For frequencies $\omega < \omega_p$, $\epsilon_r(w)$ is negative and therefore the complex refractive index $\tilde{n} = \sqrt{\epsilon_r}$ is purely imaginary. It becomes real and positive for $\omega > \omega_p$, going through zero exactly at the plasma frequency. The reflectivity can be calculated from $\tilde{n}$ as $R = \left|\frac{\tilde{n}-1}{\tilde{n}+1}\right|^2$. The frequency dependence of the reflectivity shows that $R = 1$ for $\omega \leq \omega_p$ and then decreases sharply, as indicated by the dotted line

in figure 1.8. Therefore, according to the Drude model, metals are expected to be perfect reflectors for frequencies lower than the plasma frequency and start transmitting at higher frequency, becoming eventually transparent if one goes far enough in the ultraviolet region. Indeed, metals are very good reflectors in the visible range, but their reflectivity is less than 100%. The solid line in Figure 1.8 shows the experimental reflectivity of Aluminium measured in [EPS63] and the dashed line shows the effects of damping[1] to the predictions of the Drude model. It is evident that including the damping is not sufficient to reproduce the experimental data, which is not only lower than predicted, but also shows a dip at around 1.5 eV. To explain this features is necessary to go beyond a classical description of the solid and consider the effects of interband electronic transitions on the dielectrical function.

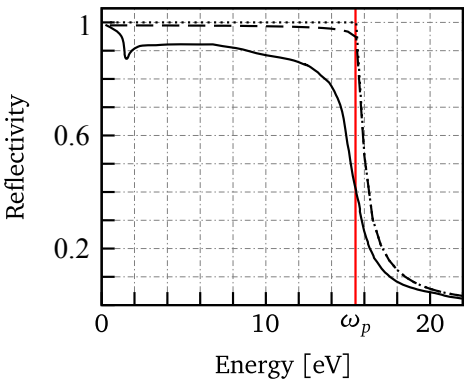

Figure 1.8: Frequency dependence of the reflectivity of a Aluminium calculated with the Drude model (*dotted line*), including the damping (*dashed line*) and the experimental data taken from [EPS63].

1.2.3 Quantum mechanical description

Quantum mechanical interpretation of the permittivity relates the absorption of light to the transition of electrons to a higher energy state. One can distinguis two kinds of optical transitions: direct (DOT) and indirect (IOT). DOT involves only the interaction between the electrons and the electric field. Therefore, due to the small momentum of the photon, the electron wavevector remains nearly unchanged, and the photon absorption in a DOT corresponds to a vertical transition in the band structure. Con-

[1]The damping $\tau = 8.0 \times 10^{-15}$ s has been calculated from Eq. (1.14) at $\omega = 0$ with a conductivity at room temperature $\sigma = 4.1 \times 10^7\,\Omega^{-1}\,\mathrm{m}^{-1}$ and an electron density of $n = 1.81 \times 10^{29}\,\mathrm{m}^{-3}$

cerning DOTs a further distinction can be made between the *interband* and *intraband* transitions. The former are resonant transtions which can occur only if the energy of the phonon corresponds to the energy difference between the two bands. The latter, instead, are non resonant transitions within the same band and affect only the real part of the dielectric function, with a typical ω^{-2} dependence. IOT takes into account the interaction with lattice imperfections and phonons, which lead to changes in the electronic wavevector, and thereby correspond to a resonant nonvertical transition in the band structure. They only contribute to the imaginary part of the dielectric function.

Optical transitions help to explain the features of the reflectivity spectrum of aluminium shown in figure 1.8. The lower reflectivity of Al compared to the predictions of the Drude model is due to electronic transitions between bands below and above E_F. Furthermore, the band structure of aluminium presents parallel occupied and unoccupied states at both the W and K points of the Brillouin zone, separated by a gap of approximately 1.5 eV [Seg61]. According to Fermi's golden rule the absorption rate is proportional to the density of states for the involved states. If two bands are parallel, transitions between them can occur for many different $\mathbf{k}$ states and the density of states at the energy difference between the two states will be high, resulting in a very high absorption at a given energy. This explains, for instance, the dip in the reflectivity of aluminium at 1.5 eV.

1.2.4 Transient reflectivity

Light can act not only as a perturbation source to drive the system in the desired state, but also as an instrument to detect the system response to the sudden change. Within the innumerable spectroscopy techniques existing nowadays, a special branch is represented by the time-resolved techniques. The majority of them are so-called pump-probe techniques: a first "pump" pulse perturbs the system, leading to a change in its optical properties. The pump-induced changes can be observed by irradiating the sample with a second "probe" pulse and measuring the response. Controlling the time

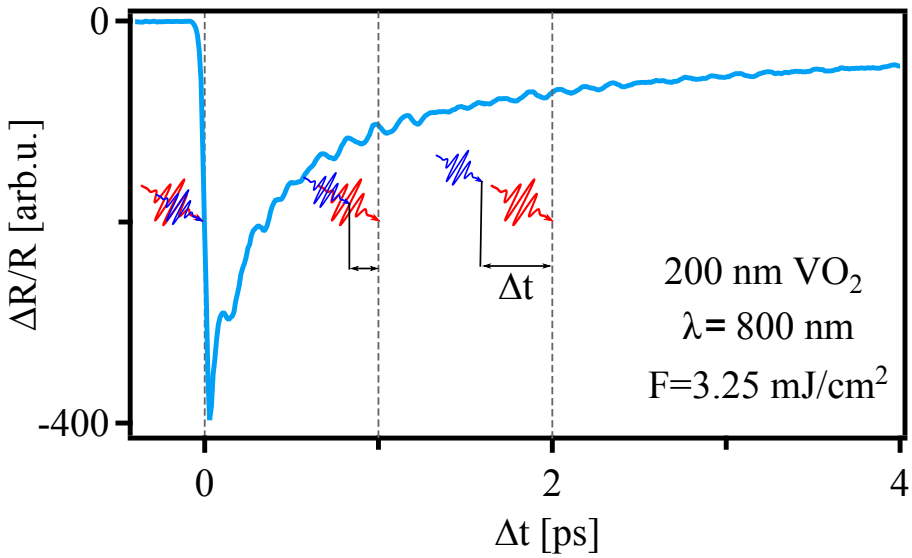

Figure 1.9: Example of a transient reflectivity trace. A sudden change in the intensity of the signal is observed for $\Delta t = 0$ as well as the subsequent exponential decay. This changes reflect the dynamics of excitation and relaxation of hot carriers.

delay Δt between the pump and the probe pulses allows to resolve the dynamics of the system in the time domain. The time resolution of the experiment is determined by the duration of the pulse. Usually, the probe pulse is chosen to be weaker than the pump pulse, in order to avoid further significant changes of the measured quantities.

Transient reflectivity is an example of a pump-probe technique. Figure 1.9 shows a transient reflectivity measurement of VO_2. A first sudden change, due to the excitation of electrons, is observed at $t = 0$ and is followed by a long-lasting exponential decay due to the relaxation of the electronic system through energy exchange with the lattice. At negative delays the probe reaches the sample before the pump and no pump-induced signal is detected. At $t = 0$ pump and probe arrive simultaneously and the measured signal is due to the instantaneous effects of the excitation, which in this case correspond to a decrease of the reflectivity due to electronic transition. At positive delays the system can start to relax during the time interval separating pump and probe and the latter measures the reflectivity associated to the state of the system at $t = \Delta t$. It is important to note that every data point corresponds to many different pairs of pump

and probe pulses, as schematized by the red (pump) and blue (probe) wave packets in the figure. Usually the system recovers within the interval between two pulse pairs and the changes induced and measured by each of them are independent of the effects induced by the previous light pair.

Many different features can be expected, depending on the properties of the studied material and the frequency of light used in the experiment. The processes described in Sec. 1.1.3 are associated with different contributions to ϵ_r (Sec. 1.2.1–1.2.3) and its pump induced changes. The relative ratio between the free carrier excitation and light absorption due to resonant processes determines the intensity and the sign of the transient reflectivity signal. Furthermore, if the material is excited with a pulse shorter than the period of lattice vibrations, large amplitude oscillations can be observed in the time dependent trace. These indicate that a large number of lattice vibrations are excited coherently (Sec. 3.1.2).

1.2.5 Coherent Phonons: probing coupling mechanisms in the time domain

Laser pulses whose duration is shorter than the period of a lattice vibration allow to excite this vibration with a high degree of spatial and temporal coherence. The presence of such a strong excited mode induces a modulation of the dielectric tensor, which can lead to the superposition of large amplitude oscillations on the time dependent reflectivity signal. Historically, two kinds of mechanisms have been considered for the generation of coherent phonons: the *impulsive stimulated raman scattering* (ISRS) and the *displacive excitation of coherent phonons* (DECP). The two processes are schematically illustrated in figure 1.10.

In ISRS the excitation is produced via inelastic Raman scattering and the ions oscillate in the ground state around the equilibrium coordinate Q_0 (Panel (a)). The driving force depends on the Raman tensor and on the two components of the field involved

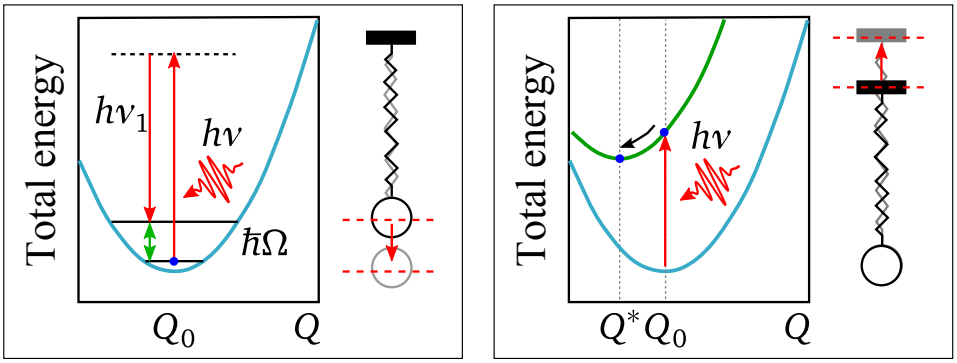

Figure 1.10: Comparison between the coherent phonon excitation mechanisms. (a) Impulsive Stimulated Raman Scattering (b) Displacive Excitation of Coherent Phonons. The springs schematize the driving forces. The mechanisms are described in terms of potential energy surfaces: in ISPS the excitation occurs in the ground state, while in DECP the laser is promotes the system to an excited state (Fig. adapted from [Rad06]).

in the Raman process. In the case of a short pulse it is an impulsive force and the initial phase of the motion is sine-like.

The electronic population excited upon light absorption is, instead, at the origin of DECP (Panel (b)). Indeed the electronic system modifies the electron-ion potential instantaneously (on the timescale of the pulse duration) , thereby exerting a force on the lattice. Thus, the system evolves to a new potential curve, where the minimum Q^* is displaced with respect to the original coordinate. This sets oscillations of the ions around the new coordinate. The change in the potential occurs step wise and the oscillations begin at the maximum, in a cosine-like motion.

In 2002, Stevens *et al.* described both theories in a more general theoretical framework that includes an excitation term based on two Raman tensors having similar real components but different imaginary parts [SKM02]. The real part is related to the ISRS mechanism while the imaginary part is associated with the displacive mechanism.

1.2.6 Nonlinear optical processes

If the field strength in the medium is of the same order of magnitude as the local field, the nonlinear therms in equation (1.2) have to be taken into account. The n-th order polarization can be written as

$$\begin{aligned}\mathbf{P}^{(n)}(\mathbf{r},t) = \int_0^\infty dt_1 \dots dt_n \int_{-\infty}^\infty \epsilon_0 \chi^{(n)}(\mathbf{r}-\mathbf{r}_1,\dots,\mathbf{r}-\mathbf{r}_n,t-t_1,\dots,t-t_n)\cdot \\ \mathbf{E}(\mathbf{r}_1,t_1)\dots\mathbf{E}(\mathbf{r}_n,t_n)d\mathbf{r}_1\dots d\mathbf{r}_n\end{aligned} \tag{1.16}$$

where the susceptibility $\chi^{(n)}$ is a tensor of rank n which depends on the symmetry of the medium.

If the electric field contains two different frequency components, $E(t) = E_1 e^{-i\omega_1 t} + E_2 e^{-i\omega_2 t}$, the second order term becomes[2]

$$\begin{aligned} P^{(2)}(t) = \epsilon_0 \chi^{(2)} \big[& 2E_1^* E_1 + 2E_2^* E_2 + && \text{(OR)} \\ & + E_1^2 e^{-i(2\omega_1)t} + E_2^2 e^{-i(2\omega_2)t} + c.c.\big] && \text{(SHG)} \\ & + 2E_1 E_2 e^{-i(\omega_1+\omega_2)t} + c.c. + && \text{(SFG)} \\ & + 2E_1 E_2^* e^{-i(\omega_1-\omega_2)t} + c.c. + && \text{(DFG)} \end{aligned} \tag{1.17}$$

Thus, the nonlinear order of the polarization accounts for the generation of field components whose frequency is given by the doubled fundamental frequencies (*Second Harmonic generation* – SHG), their sum (*Sum Frequency generation* – SFG) or their difference (*Difference frequency generation* – (DFG)).

At each position of the crystal, the oscillating second order polarization radiates at angular frequency ω_3, with the corresponding wave vector $\mathbf{k} = n(\omega_3)\frac{\omega_3}{c}$. Macroscopic light emission is obtained only if the phase of all this microscopic waves are matched. This is equivalent to the momentum conservation $\mathbf{k}(\omega_3) = \mathbf{k}(\omega_1) + \mathbf{k}(\omega_2)$.

Energy conservation is at the origin of another nonlinear effect, the *optical parametric amplification*. Indeed, in the DFG process, for every phonon created with frequency

[2]The second order susceptibility $\chi^{(2)}_{ijk}$ has been simplified with the correspondent scalar form

$\omega_3 = \omega_1 - \omega_2$, a phonon at the higher frequency ω_1 must be annihilated and the one at lower frequency ω_2 must be created. The *optical parametric amplification* is the process used in the Optical Parametric Amplifier (OPA) and in the Non-collinear Optical Parametric Amplifier (NOPA).

1.3 Vanadium Dioxide: a controversial material

Vanadium dioxide belongs to the broad family of vanadium oxides. Many of them undergo a temperature-driven metal-to-insulator transition, which is accompanied by a drastic change of the physical properties, such as conductivity or reflectivity [NH08]. In the case of VO_2, the transition is first order and occurs at 340 K. It was first discovered in 1959 by Morin, who observed a sudden drop of conductivity by approximately 4 orders of magnitude, associated to a 2 K wide hysteresis [Mor59]. Besides the change of conductivity, VO_2 exhibits a discontinuity in the optical transmittivity and reflectivity [VBB68], and the third harmonic optical signal decreases by a factor of 30 [PYS02]. Similar changes are observed in the magnetic susceptibility, thermal expansion coefficients and Seebeck coefficients [Gat07]. At the same time, VO_2 changes its lattice structure from a high-temperature rutile phase to a low-temperature monoclinic one.

Since the work of Morin [Mor59], the nature of the MIT transition in VO_2 has been subject of debate. The critical phenomena observed are due to a subtle interplay between the structural and the electronic contributions, and it is still not clear which one is mainly responsible for driving the transition. The transformation of the unit cell at $T = T_c$ could easily lead to a description of the transition in terms of a Peierls-like distortion [Goo71]. On the other hand, it is a common feature of the transition metal oxides to have very narrow $3d$ bands. The consequent strong correlation effects can give rise to a Mott-Hubbard type of modelling [ZM75].
The issue is whether the structural transition is responsible for the opening of the gap or whether it is due to the electronic correlations alone. In the latter case the structural transition would follow. Section 1.3.1 presents the two components of the transition, describing the structural and electronic properties of vanadium dioxide, while section 1.3.2 reviews the most important points of the debate.

1.3.1 Structural, electronic, and optical properties of VO_2

In the high temperature phase, vanadium dioxide has a tetragonal rutile (R) structure of the $P4_2/mnm$ space group, with all the vanadium atoms located at the centers of an oxygen octahedron (Fig. 1.11(a)). The rutile phase is characterized by two sets of identical V−V chains along the c_r axis. All V−V distances are 2.85 Å. Upon the

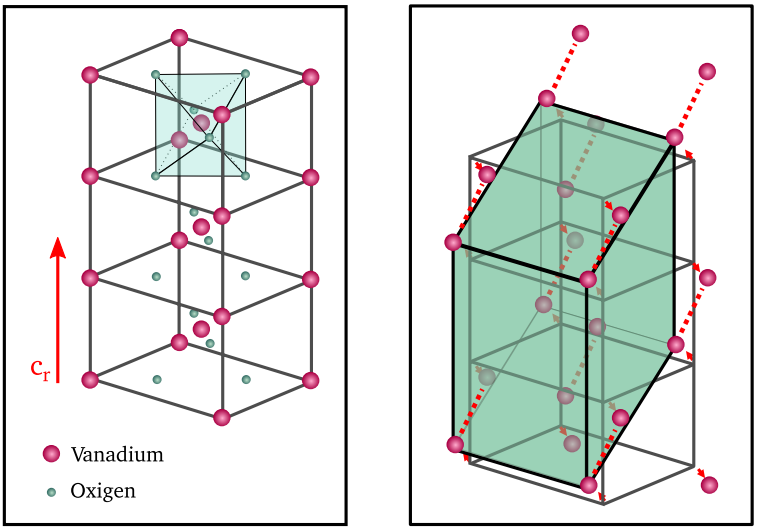

(a) The high temperature, rutile structure of VO_2. The V^{4+} ions are at the center of an O ochtaedron.

(b) The low temperature, monoclinic structure of VO_2. The tilting and pairing of the V atoms is indicated.

Figure 1.11: The lattice structures of VO_2.

transition the unit cell doubles in size and assumes a monoclinic (M_1) structure of lower symmetry, belonging to the $P2_1/c$ space group. The V^{4+} ions pair and tilt, as shown in figure 1.11(b), and the alternate distance between them is 2.61 and 3.16 Å. The oxygen atoms, on the contrary, stay almost at their original position.

The symmetry reduction results in an increase of the number of Raman active modes, from 4 in the R phase to 18 in the M_1. According to the group theoretical analysis, the high temperature modes have A_{1g}, B_{1g}, B_{2g} and E_g symmetries, while in the low temperature phase there are nine A_g and nine B_g modes. Table 1.1 lists the mea-

sured frequencies and the symmetries of the Raman-active modes, as reported in Ref. [Sch02]. The two A_g modes of the M_1 phase at 5.97 and 6.75 THz are crucial to the metal-to-insulator transition since they are associated with the stretching and tilting of the vanadium atoms.

The first modelling of the electronic structure in vanadium dioxide has been formulated by Goodenough within the molecular orbital approximation, where the electronic wavefunctions of the solid are represented by linear combinations of atomic orbitals [Goo71]. In the case of VO_2, the involved orbitals are the $3d$ of the V^{4+} ion and the $2p$ of the O^{2-} ion. The physical properties of VO_2 are determined mainly by the vanadium orbitals, whose energy is around E_f, while the oxygen orbitals are lower in energy and contribute mainly to the bonding bands.

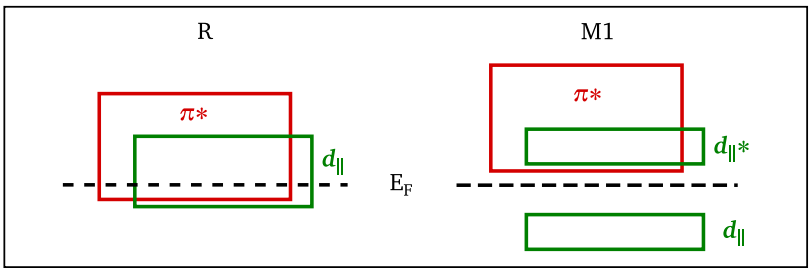

Figure 1.12: Schematic of the band structure of VO_2 in the molecular orbital picture of Ref. [Goo71]. In the rutile phase (R) the $d_{||}$ and π^* overlap at E_F and the material is metallic. In the monoclinic (M_1) phase the band gap originates from the splitting of the $d_{||}$ band into bonding and antibonding states and the lifting of π^*.

In the rutile structure the octahedral field generated by the six O surrounding the V atom splits the degeneracy of the $3d$ states of V into the threefold degenerate t_{2g} and the twofold degenerate e_g^σ orbitals. The t_{2g} state originating from the vanadium $d_{x^2-y^2}$ orbital, which points along the c_r axis, forms the $d_{||}$ band, cf. Fig. 1.12. Due to the high anisotropy of the state the band is very narrow. The other orbitals (d_{xz} and d_{yz}), forming the π^* band, are stronger hybridized with the oxygen $2p$ orbitals and the band is wider. Both $d_{||}$ and π^* bands are partially occupied and thus the R phase is metallic.

Doubling of the unit cell across the transition implies doubling of the total number of

Rutile			Monoclinic		
Wavenumber [cm^{-1}]	Frequency [THz]	Symmetry	Wavenumber [cm^{-1}]	Frequency [THz]	Symmetry
240	7.20		149	4.46	
390	11.69		199	5.97	A_g
510	15.29	A_{1g}	225	6.75	A_g
625	18.73		259	7.76	B_g
			265	7.94	B_g
			313	9.38	A_g
			339	10.16	B_g
			392	11.75	A_g
			395	11.84	B_g
			444	13.31	B_g
			453	13.58	B_g
			489	14.66	B_g
			503	15.08	A_g
			595	17.84	A_g
			618	18.53	A_g
			670	20.09	B_g
			830	24.88	B_g

Table 1.1: Frequencies and symmetry assignement of the normal modes in VO_2, from [Sch02]

3d and 2p orbitals. The effects on the band structure are shown on the right-hand-side of figure 1.12. The $d_{\|}$ band is splitted into the bonding ($d_{\|}$) and antibonding ($d^*_{\|}$) states and the π^* band is shifted above the Fermi level.

This scheme of the band structure was confirmed by the photoemission experiments of Koethe *et al.* [KHH+06]. They measured a very broad O 2p structure between 2 and 10 eV below E_F, which is very similar in both phases. On the other hand, the V 3d sates feature peaks at 0.9 eV below E_F for the M_1 and at the Fermi energy for the R phase. The photoemission spectra of the R phase also show a satellite peak at the binding energy of 1.3 eV, which disappears in the low temperature phase, attributed to a plasmon resonance [BSB81].

X-ray absorption demonstrates that the π^* band dominates the low part of the conduction band and its leading edge is shifted by 0.2 eV across the transition. Therefore the band gap was estimated to be around 0.6 eV [KHH+06].

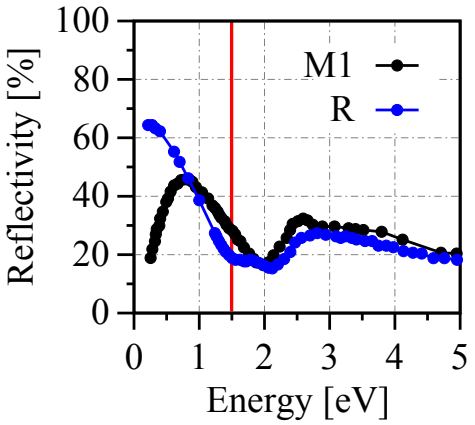

Figure 1.13: The reflectivity spectra of VO_2, from [VBB68].The red line indicates the energy we use in our experiments (800 nm), where the reflectivity is higher in the M_1 phase than in the R phase

Finally, Fig. 1.13 shows the reflectivity spectra of VO_2 in the energy range between 0.2 and 5 eV ($\simeq$ 200–4000 nm) from Ref. [VBB68]. The black curve was measured in the monocilinic phase and the blue one in the rutile phase. For most of the frequencies, the reflectivity decreases across the metal to insulator transition. In particular, the larger deviation occurs around 1.5 eV, indicated by the red line. This correspond to the energy we perform our experiments at and, therefore, we expect to observe a decrease of the signal.

1.3.2 The nature of the transition: Peierls or Mott-Hubbard?

Many different models have attempted to identify the trigger of the metal-to-insulator transition of vanadium dioxide. Most of them descend either from a Peierls-like or a Mott-Hubbard-like description. In the former, the electronic transition is due to the structural deformation, while in the latter strong electronic correlations are at the origin, and those are not necessarily followed by a structural transition. The Peierls picture is at the basis of the model proposed by Goodenough, where the opening of the band gap completely descends from the pairing and tilting of the vanadium atoms [Goo71]. In particular, the tilting favours the hybridization of the d_{xz} and d_{yz} orbitals with the O $2p$ orbitals, shifting the π^* band to higher energies. The splitting of the $d_{\|}$ band, and thus the opening of the gap, is a direct consequence of the formation of homopolar cation-cation bonds, due to V^{4+} pairing. Zylbersztejn and Mott, even recognising the importance of the tilting in lifting the π^* band, stated that no quantitative description is possible without taking into account the Hubbard U term [ZM75]. The up-shifting of the π^* band reduces the screening of the Coulomb repulsion between the strongly correlated electrons in the $d_{\|}$ band, which is then liable for a Mott-Hubbard transition.

Yet, no single model, neither Peierls nor Mott-Hubbard, is able to provide a global and coherent explanation for the transition. As Gatti explained in detail in his PhD thesis, also first-principle calculations often fail to do so [Gat07]. Local-density approximation (LDA) is able to correctly reproduce the ground state properties, but systematically underestimates or even closes the band gap, while LDA+U reproduces the experimental gap but at cost of an insulating R phase. At the same time, the Hartree-Fock calculations do not account for correlations and lead to a huge band gap (7.6 eV). In a recent first-principle calculation, Gatti *et al.* were able to reproduce the main features of the photoemission spectra of [KHH+06]. They interpret them in terms of a quasiparticle picture with a completely static description of the correlation and indicate the orbital switching of the V $3d$ states as the main responsible for the transition from the isotropic

metal to the more one-dimensional insulator [GBOR07].

In order to get more insight in the nature of the metal-to-insulator transition of VO_2, it is necessary to address the two components separately. This was made possible by the discovery of the photoinduced phase transition [RB71], since it opens the possibility of using time-resolved techniques to probe the different sub-system. Furthermore, these techniques allow to observe the dynamics of the process at early times, helping to clarify which degree of freedom of the system is responsible to trigger the MIT. A review of some of the previous time-resolved experiments performed on this compound is given in section 1.3.3.

1.3.3 The photoinduced phase transition

The possibility of triggering the transition by photoexcitation in the insulating phase of vanadium dioxide has been demonstrated by time-resolved optical experiments [BBW+96] and confirmed by X-ray defraction experiments [CTS+01]. In the latter, Cavalleri *et al.* show that both electronic and atomic-structural changes occur on a subpicosecond timescale and determine a fluence threshold of $7\,\mathrm{mJ\,cm^{-2}}$ for the transition. In a later experiment they claim the existence of a limiting timescale of 75 fs which they attribute to coherently initiated structural motion [CDC+04]. Thus, they affirm that the structural distortion is necessary for the formation of the metallic phase, even when the correlated $d_{\|}$ band is highly depleted.

In a coherent phonon analysis on a 100 nm thin film, Kim and co-workers suggest that the metal-to-insulator transition and the structural phase transition do not occur simultaneously [KLK+06]. They define an intermediate non-equilibrium state, the monoclinic and correlated metal (MCM), which is generated by photoassisted hole excitation of the low temperature phase. The structural phase transition to the R phase is due to subsequent thermal heating.

Kübler et al. were the first to perform a multi-THz measurement of VO_2 [KEH+07].

They observe a coherent modulation of the lattice polarizability at 6 THz, which is related to the motion of the V−V dimers. On the other hand, the electronic conductivity shows different behaviour below and above the fluence threshold, Φ_c =4.6 mJ cm^{-2}. In particular, above Φ_c, the conductivity settles to the characteristic value of the metallic phase after a single V−V oscillation cycle, even if the lattice is still far from equilibrium. They regard this decoupling of the electronic conductivity from the lattice motion as a direct consequence of the loss of electronic correlations due to the presence of a critical density of photoexcited lattice sites.

A time-resolved Bragg diffraction performed by Baum *et al.* shows two different timescales for the decrease in intensity of the Bragg spots [Bau07]. The intensity of the spots related to the motion along the V−V bond decreases on a fs timescale, while all other spots have a longer decay time ($\simeq$10 ps). This suggests that the breaking of the V−V bond along the bond direction precedes the tilting of the vanadium atoms to the new positions in the rutile structure. Photoexcitation primarly involves electrons coming from the $d_{\|}$-band, which are brought into an antibonding state. This causes a repulsive force on the atoms, which separate in the direction of the bond, while the transformation of the unit cell occurs on a longer timescale.

All the experiments seem to agree that the metal-to-insulator transition and the structural distortion do not occur simultaneously, however they still disagree in determining the responsible for the transition. The controversy on the nature of the transition seems to be still far away from being resolved.

2 Experimental Details

Chapter 1 concerned with the theoretical background of the thesis. Nevertheless, this is an experimental work and the setup plays an important role as well. In section 1.2 light was described as a powerful tool for perturbing and probing a material. However, not every light source is suitable for both photo-excitation and ultrafast detection. The former requires light to be intense enough to move the system away from the equilibrium, while for the latter the exposition time needs to be shorter than the detected event itself. These conditions are fulfilled by femtosecond pulsed lasers and section 2.1 describes the laser system used in our lab. Besides transient reflectivity experiments we performed a more sophisticated pump-pump-probe experiment. The setups for both experiments are described in section 2.2, together with the detection method. Finally, an experiment requires a well defined environment. Since working with oxides an ultra high vacuum environment is not necessary, the only need was to control the temperature of the system. Therefore an optical cryostat has been used, which is described in section 2.4.

2.1 The laser system

An ultrafast time resolved experiment is the spectroscopy counterpart of the photography of a moving object. In both cases the exposition time has to be shorter than the dynamics to allow for a good resolution. Resolving dynamics that occur on the femtosecond timescale is made possible by using ultrashort ($< 40\,\mathrm{fs}$) laser pulses. Moreover, the focus of this experiment is the coherent excitation of phonon modes, which requires the light pulse to be shorter than the vibrational period of the lattice. Finally, the direct consequence of the pulse duration is that their peak power is extremely high. This makes pulsed lasers the ideal choice for an experiment that requires strong photo-excitation and high time resolution.

The laser system used in our lab is a commercial setup from the company Coherent, based on a mode-locked Ti:Sapphire oscillator (Micra) and a regenerative amplifier (RegA). The generation of femtosecond laser pulses in the oscillator is explained in section 2.1.1 and their regenerative amplification in section 2.1.2.

The experiments presented in this thesis were performed using only the output light from the RegA. However, during my time in the lab I have contributed to the set up of other light sources, that use the RegA output at 800 nm to generate pulses in other spectral ranges. They are briefly introduced in section 2.1.3. The output of the regenerative amplifier has enough power to drive more than one source simultaneously, allowing different experiments to be performed at the same time. Appendix B presents the design and realization of a continuously variable switchbox, the project I was involved in along with the vanadium dioxide experiments. It allows to tune the power sent to different sources without having to use beam splitters of fixed reflectivity and transmission values.

2.1.1 Generation of ultrashort laser pulses: the mode-locked Ti:Sapphire oscillator

A laser consists of three components: an energy source, a gain medium and a cavity, which is confined by a high and a partial reflector.

The gain medium is the heart of a laser. Usually light passing through a material is rather absorbed than amplified, although both phenomena are two different aspects of the same atomic process, differing only on the initial status of the atom. If one atom is in an excited state, it can recover its ground state either by spontaneous or by stimulated light emission. In the stimulated emission, the emitted photon will have the same phase, frequency, polarization, and direction as the one of the stimulating beam, which is thereby amplified. The gain medium in the Micra is a Sapphire (Al_2O_3) crystal doped with Titanium (Ti) atoms. Its absorption ranges from 400 to 600 nm, while its emission spectrum goes from 680 to 1100 nm and has a maximum at 790 nm. Lasing

is possible only if a sufficient number of atoms is in an excited state, i.e. if a sufficient population inversion between the low and the high energy state is reached. Therefore, energy must be transferred to the system in order to raise the atoms to their excited state. This process, which is referred to as pumping, is possible in Ti:Sapphire only by absorption of the intense light of another laser source. In the Micra design light at 532 nm is used, generated by the second harmonic of a diode pumped solid state laser (Nd:YVO_4, Coherent Verdi).

Usually, a laser emits continuously and can operate at all wavelengths satisfying the condition $\lambda = \frac{n}{2}d$, where d is the length of the cavity. These wavelengths are called the *longitudinal modes* of the cavity. When several modes are lasing simultaneously they can constructively interfere and lead to the formation of an intense peak. If the phase relation between the modes is non-randomly adjusted and kept constant, the intensity of the peak will increase and lead to the emission of a short pulse. This process is referred to as *mode-locking* and is reached in Ti:Sapphire in a passive way, by exploiting the electro-optical Kerr-effect. It occurs when the refractive index of the medium is dependent on the intensity,

$$n(r,t) = n_0 + n_1 I(r,t)$$

Since the beam intensity is not spatially uniform, being higher in the center, the refraction index will have a spatial distribution and a gradient index lens is formed. Thus the more intense part of the beam is focused stronger and the process is self-sustaining. Furthermore, high intensities are required for the Kerr-lens to be formed and this can only happen upon interaction with a mode-locked pulse. The mechanism is therefore a way of narrowing the beam only for the pulses, allowing a better transmission through an aperture and the separation from the continuous wave (CW) beam. Once the high intensities needed to activate the optical Kerr-effect are reached another nonlinear process is induced, this time by the temporal intensity variations. This process is called *self phase modulation* (SPM) and contributes to widen the frequency spectrum of the pulse. Indeed, a larger bandwidth is needed to achieve short pulses, since the temporal

duration of the pulse is related to its bandwidth. For example, in case of a gaussian shaped pulse, $\Delta t \Delta \nu = \frac{1}{\pi} 2 \ln 2$.

Both optical components of the cavity and SPM generate a positive *chirp* in the pulse, i.e. the red edge travels faster than the blue one, resulting in the temporal broadening. This dispersion is compensated by a prism compressor in the resonator. Descriptively, a prism compressor is made of two dispersive prisms in a special configuration, where the red edge travels along a longer optical path than the blue one. This generates a negative chirp in the pulse which compensates the positive one caused by the optical components. Details of the working principle of this compression technique are given in [FMG84, GFM84].

For every loop in the cavity, a part of the light is coupled out of the resonator through the partial reflector. The repetition rate of the oscillator is therefore related to the length of the cavity d by $1/\tau = c/2d$. Typically, the repetition rate of the Micra is set to 80 MHz but values between 76 MHz and 82 MHz are possible. The output power is specified to be >300 mW [Coh07].

2.1.2 Amplification of laser pulses: the regenerative amplifier

The power of the pulses generated by the Micra is not sufficient for the experiments we perform and also not enough to produce the nonlinear optical exploited in the other light sources available in the lab. To amplify the pulses we use a commercial device, the RegA, also from Coherent [Coh97]. As in the oscillator the active medium in the cavity is Ti:Al_2O_3 and is pumped by the CW output of the Verdi at 532 nm.

A high speed acousto-optic modulator made of Tellerium Dioxide (TeO_2), the *cavity dumper*, is used to couple in and out the pulses coming from the oscillator, with a tunable repetition rate. They are amplified for about 27 round trips in the resonator, after which the population inversion in the Ti:Sapphire is completely depleted. To regenerate the high population inversion needed for amplification, spontaneous emission needs to be avoided. For this purpose a *quality switch* (Q-switch) – another acousto-

optic modulator – degrades the quality of the cavity during around 3–7 μs. When the population inversion is completely regenerated, the quality of the resonator is restored and a new pulse is coupled in.

The *chirped pulse amplification* technique is used to avoid changes in the pulse profile via non-linear effects or the damage of the active medium, both caused by the high peak energies generated. The ultrashort pulse is stretched before being coupled into the RegA by going through a specific arrangement of dispersing gratings. There, the pulse is positively chirped and stretched in time up to 50 to 100 ps and its intensity becomes sufficiently low to make safe amplification possible. Positive GVD is also caused to the pulse in the Q-switch during each round-trip of the amplification. An analogous set of gratings is used after amplification to remove the chirp and re-compress the pulse.

During the transient reflectivity measurements presented in section 3.1, the repetition rate of the RegA has been set to either 300 or 150 kHz. At this repetition rate the pulse energy reaches values of 6.6 or 13.3 μJ and after compression the pulses have a duration of around 40 fs.

2.1.3 Other light sources available in the lab

Sometimes it is necessary to investigate the dynamics of a material at a resonance, in which case a tunable laser source comes in handy. Even if they were not used directly in the measurements described in this work, I have contributed to the installation and alignment of the remaining beam paths completing figure 2.1 and they are briefly described in this section.

The output power of the RegA, of about 2 W, suffices to drive 3 different sources at the same time. Until setting up of the switchbox described in appendix B will be ready, the RegA output is divided by means of beam splitters of fixed values and mirrors mounted on flip-mounts, which allow to choose between the different sources.

The lab disposes of an Optical Parametric Amplifier (OPA) and a Nonlinear Optical

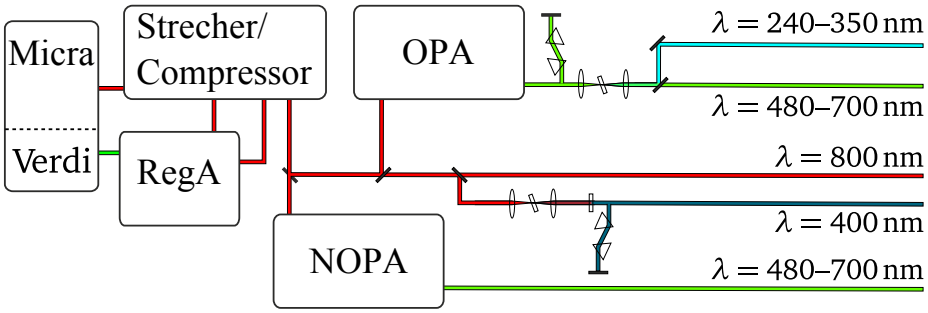

Figure 2.1: The used laser system.

Parametric Amplifier (NOPA). In both systems a white-light continuum is generated by approximately 30% of the incoming light in a sapphire or YAG crystal, and constitutes the signal beam. The rest of the 800 nm beam is doubled in frequency in a beta-barium-borate (BBO) crystal and is used as pump beam for the optical parametric amplification of the signal (Sec. 1.2.6) in a second BBO crystal. The difference between OPA and NOPA is given by the configuration in which the signal and the pump beam reach the final BBO for the amplification, being collinear in the first and non collinear in the second. The non collinearity favours phase matching between the involved photons, and permits amplification over a wider range of frequencies, without tuning the BBO angle. The function of OPA and NOPA is explained in detail in [Weg09]. The output of both parametric amplifiers is in the visible range, from 480 nm to 700 nm. The pulses of the OPA are 60 fs long, while in the second one pulses shorter than 10 fs can be obtained. The output of the OPA is further doubled by a BBO crystal to obtain light in the UV-range (240–350 nm).

At the moment, we also dispose of the second harmonic of the RegA output (400 nm) and the generation of higher harmonics (at 260 and 200 nm) is planned. The remaining light is used in the fundamental, 800 nm beam. For the presented experiments the available beam power was of about 1 W, corresponding to 3.3 µJ per pulse at a repetition rate of 300 kHz and to 6.6 µJ at 150 kHz.

2.2 The generation and detection of the signal

To perform time-resolved reflectivity measurements at least two laser beams are required: one to perturb and one to probe the system. The first one is more intense and is called the *pump* beam while the second is the *probe*. Two different configurations of the beam paths have been used and are both shown in figure 2.2.

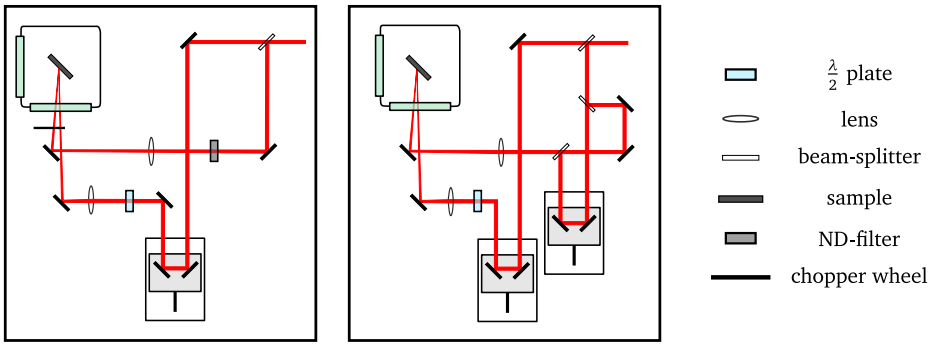

(a) Pump-Probe configuration

(b) Pump-Pump-Probe configuration

Figure 2.2: The used beam configurations

Configuration (a) provides one pump and one probe beam. The 800 nm RegA output is compressed at the grating compressor and then tubed and sent to the experiment. It is split by a 75 %–25 % beam splitter. The reflected beam, having 75 % of the total intensity, forms the pump beam. It passes through a neutral density (ND) filter, that allows to control the intensity, and is then focused onto the sample with a 300 mm lens. The angle of incidence is about 45°. The 25 % fraction constitutes the probe beam. It is first sent to a retroreflector mounted on a linear motorized translation stage, whose purpose is the control of the delay between pump and probe pulse. By moving the stage by a distance x the optical path of the beam changes by $2x$ and the pulse is delayed by $\tau = 2x/c$, where c is the speed of light. A distance $x = 1.5\,\mu\text{m}$ corresponds to a relative delay between the pulses of 10 fs.

Configuration (b) adds a Mach-Zehnder interferometer to the pump beam. It is used to

generate two different pump pulses with a fixed phase relationship. A first 50 %–50 % beam splitter creates the two pump pulses. One is sent to two mirrors in a configuration similar to a retroreflector and back to a second 50 %–50 % beam splitter. The second one is sent to the retroreflector mounted on a motorized linear stage and then recombined with the first on the second beam splitter. By analogy with the probe beam of the simple pump-probe configuration, the stage is used to control the delay between the two pump pulses. Thereby pump-pump-probe experiments can be performed, where the second pump is used to perturb the system after it is already in its excited state. When the two pulses are overlapped in time, the total intensity of the normal pump beam is restored.

In both configurations the polarization of the probe pulse is changed from *p*- to *s*-polarized whith a $\lambda/2$ plate, before being focused onto the sample with a 300 mm lens. To have different beam polarizations, allows an improved and simplified detection, whose scheme is presented in figure 2.3. The reflected beams are collected with a mirror and then focused by a lens on a photodiode. A Glan-Thompson prism is put between the lens and the detector. It is aligned to allow only the transmission of the *s*-polarized light and thereby completely remove any scattered light of the pump beam from the measured signal.

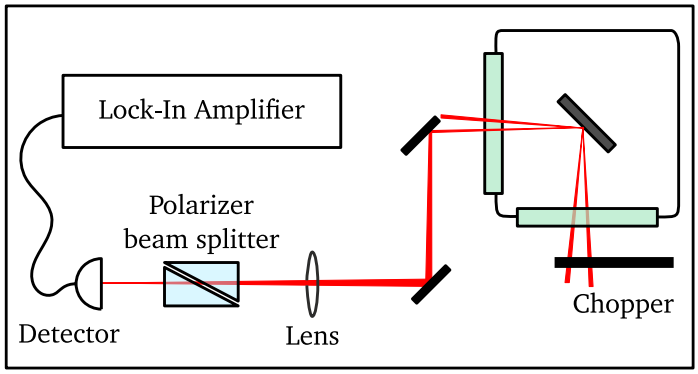

Figure 2.3: Scheme of the beam paths for detection. See the text for a detailed description.

The signal from the photodiode is measured by a lock-in amplifier and therefore has to be modulated before reaching the sample. The modulation is achieved with help of a rotating optical chopper. The blade of the chopper has two concentric series of apertures, allowing to chop the pump and the probe beam at different frequencies. The

lock-in amplifier is set at the difference frequency between the two. In this way only the pump induced signal is detected and the signal to noise ratio is further improved than in the case where only the probe beam is chopped.

2.3 Spatial and Spectral characterization of the pulse

An ideal monochromatic light pulse is described by multiplying a plane wave with a bell-shaped function. Usually, two different envelopes are used to describe intensities of real pulses: the gaussian and the secans hyperbolicus squared functions

$$E(t) = E_0 e^{-\Gamma t^2} e^{i\omega_0 t} \qquad \text{Gaussian} \tag{2.1}$$

$$E(t) = E_0 \frac{1}{\cosh^2(\Gamma t)} \qquad \text{sech}^2 \tag{2.2}$$

The Fourier transform shows that, unlike the plane wave, such a wave-packet consists of more frequencies centred on a maximum. The width of the spectrum is given by the Full Width Half Maximum (FWHM). Spectral and temporal FWHM are related by the universal inequality $\Delta t \Delta\omega \geq \frac{1}{2}$, where the equality can be reached only for Gaussian time and spectral envelopes. For all other envelopes a similar equality can be written but with a larger proportionality constant depending on the shape of the pulse. When the equality holds, the pulse is called transform limited and has the shortest possible duration for the given bandwidth [Boy08].

To characterize the spectral shape of the RegA, the spectrum was measured and is shown in Fig. 2.4. The spectrum was fitted with both the Gaussian and the sech^2 function and the obtained spectral FWHM of the RegA pulse, calculated limit duration, and the proportionality constant $k = \Delta t \Delta\omega$ are reported in table 2.1.

The pulse has been measured with a GRENOUILLE[1] and the retrieved pulse calculated from the algorithm is shown in figure 2.5. The GRENOUILLE is a simplified version

[1] GRENOUILLE ("frog", french) stays for *GRating-Eliminated No-nonsense Observation of Ultrafast Incident Laser Light E-fields*.

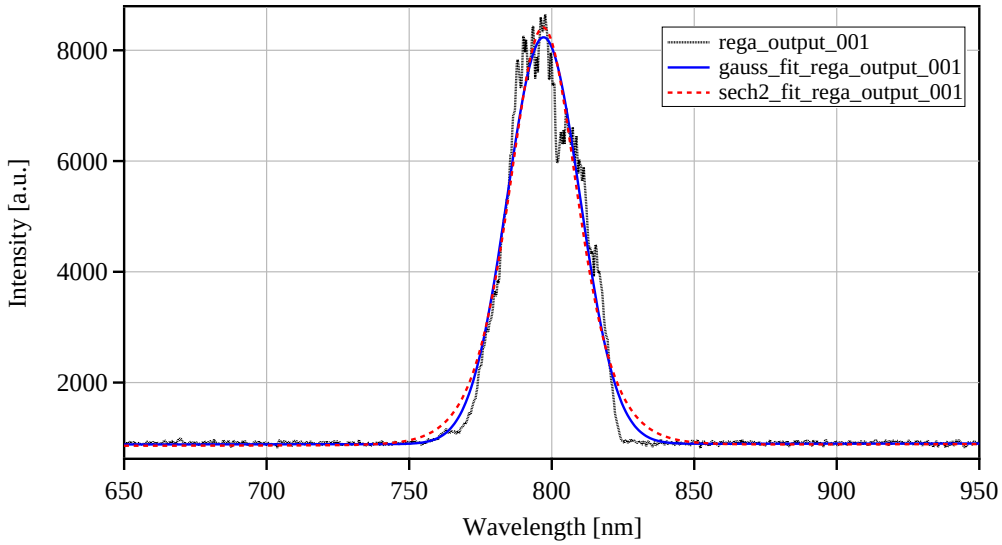

Figure 2.4: The spectrum of the RegA after the compressor and the fit with gauss function and secans hyperbolicus squared

	central wavelength [nm]	FWHM [nm]	$\Delta\omega$[THz]	Δt [fs]	k
Gaussian	797.17	30.13	89.00	31.03	2.77
$sech^2$	796.99	28.48	84.50	23.42	1.98

Table 2.1: Spectral and temporal FWHM from the spectrum shown in figure 2.5. The temporal FWHM has been calculated from the proportionality constant k

of a FROG[2], an autocorrelator-like measurement in which the autocorrelation signal is spectrally resolved. Thus, instead of measuring the autocorrelator signal energy vs. delay, FROG involves measuring the signal spectrum vs. delay [Tre00]. The 2D panel shows the spectral and temporal distribution of the pulse. In the upper panel the calculated distribution of the electric field intensity is plotted as a function of time, while in the right panel it is spectrally resolved. Both intensities are normalized to unity. The gaussian fit of the field distributions results in a temporal FWHM of 39.8 fs and a spectral FWHM of 22.9 nm.

[2]FROG: Frequency-Resolved Optical Grating

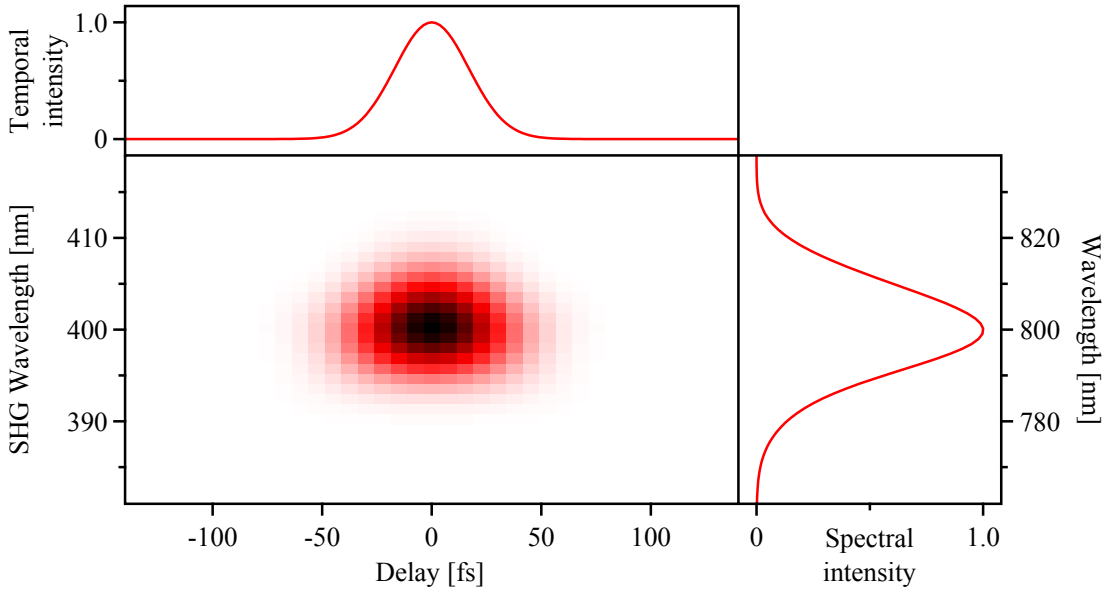

Figure 2.5: The retrieved pulse after frog measurement. The upper panel shows the temporal intensity of the electric field and the right panel the spectral one. Both are given in arb. units and normed to one.

Besides the temporal and spectral characterization it is also necessary to know the spatial properties of the pulse and the fluence irradiating on the sample. The fluence is defined as the pulse energy per unit area

$$\mathrm{F} = \frac{\Pi_{av}}{\mathrm{RR} \cdot \mathscr{A}} \tag{2.3}$$

where Π_{av} is the average measured power, RR is the repetition rate of the laser and $\mathscr{A}$ is the area. It is usually given in $[\mathrm{mJ\,cm^{-2}}]$.

To calculate the spot area, a picture of the spot is taken with a CCD camera together with a reference for dimensioning and the image is fitted with a two dimensional gaussian,

$$f(x,y) = z_0 + A\exp\left\{-\frac{1}{2\left(1-c^2\right)}\left[\frac{\left(x-x_0\right)^2}{\Delta x^2} + \frac{\left(y-y_0\right)^2}{\Delta y^2} - \frac{2c\left(x-x_0\right)\left(y-y_0\right)}{\Delta x \cdot \Delta y}\right]\right\} \tag{2.4}$$

where Δx is the width along the x-axis, Δy along the y- and c is the cross-correlation. Figure 2.6 shows a typical 2D plot with the corresponding gaussian fit and the obtained values of the parameters.

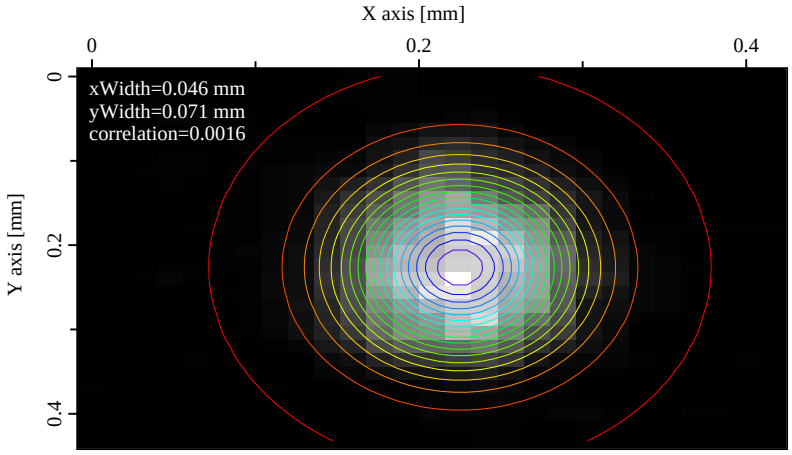

Figure 2.6: 2D plot of a typical beam spot on the sample. The contours indicate the intensity of the gaussian fit. The obtained values of the parameters are reported.

The beam area is considered to be the area at which the intensity of the beam is reduced to $I = \frac{1}{\sqrt{e}} I_{max}$. Solving equation (2.4) for this value, it reduces to the canonical equation of an ellipse $AX^2 + BXY + CY^2 = 1$, where $X = x - x_0$,$Y = y - y_0$ and

$$A = \frac{1}{(1-c^2)\,\Delta x^2}$$
$$B = -\frac{2c}{(1-c^2)\,\Delta x \Delta y}$$
$$C = \frac{1}{(1-c^2)\,\Delta y^2}$$

The area is finally given by

$$\mathscr{A} = \frac{2\pi}{\sqrt{4AC - B^2}} = \pi\sqrt{1-c^2}\Delta x \Delta y \tag{2.5}$$

Table 2.2 reports the calculated areas for all the pump and probe spots used in the measurements reported in section 3.1. The spots are numbered in pairs and in the following I will refer to the numbers introduced here to indicate a spot. The first column reports the area calculated from equation (2.5). In the second column the area is approximated to $\mathscr{A}_{app} = \pi \Delta x \Delta y$, thus not considering any tilting. The third column reports the deviation of the approximation from the real value, calculated as $\delta = (\mathscr{A} - \mathscr{A}_{app})/(\mathscr{A})$.

The size of pump and probe 1 are those of the experiment at 300 kHz and are approximately 2.5 times smaller than the spots at 150 kHz. We attribute this difference in an

spot number	$\mathscr{A}[\times 10^{-5}\,\mathrm{cm}^2]$	$\mathscr{A}_{app}[\times 10^{-5}\,\mathrm{cm}^2]$	$c[\times 10^{-2}]$	$\delta[\%]$
pump 1	4.0	4.0	9.6	4.6×10^{-1}
probe 1	3.7	3.7	-0.1	8.9×10^{-5}
pump 2	10.0	0.1	9.9	4.9×10^{-1}
probe 2	7.1	7.1	-3.4	5.7×10^{-2}
pump 3	0.1	0.1	0.2	1.4×10^{-4}
probe 3	7.6	7.7	10.0	5.0×10^{-1}

Table 2.2: Calculated values of the spot area. See text for description of the formulas used.

incorrect position of the camera with respect to the normal. In fact, to guarantee a good evaluation of the spot size, the axis of the camera has to be parallel to the sample normal. In the case of pump and probe nr. 1 we have estimated the angle between the axis of the camera and the normal of the sample to be $(40 \pm 10)^\circ$. This would correspond to a correction of $1/\cos(40^\circ)$ to the area, leading to a spot size for both pump and probe of $5(2) \times 10^{-5}\,\mathrm{cm}^2$.

From the values of the deviation we can conclude that the error introducted by neglecting the tilting of the spot, represented by c, in the calculation of the area is small and can be ignored.

2.4 The sample environment

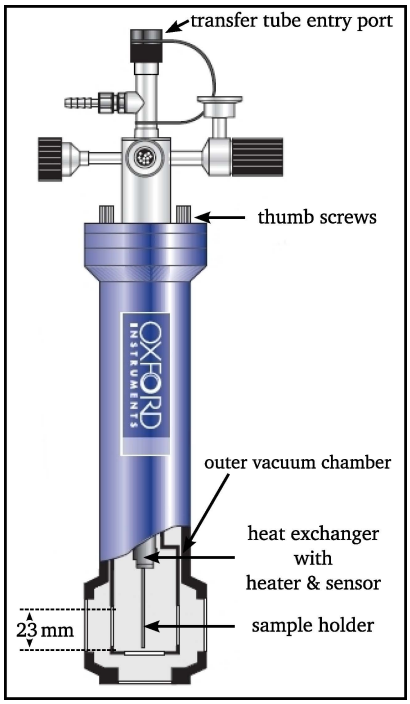

Figure 2.7: Drawing of the cryostat adapted from [Oxf05].

The sample is kept in a OptistatCF-V cryostat from Oxford Instruments that is fixed to an x, y, z translational stage on the optical table by an in-house-made support. The stage allows for alignment of all the translational degrees of freedom, while the tilting is controlled by tightening the screws of the support. The OptistatCF-V cryostat is shown in figure 2.7. It is a continuous flow cryostat, i.e. it has no internal reservoir for storing the cryogenic liquid and the sample is in a vacuum. The cooling liquid is supplied from an external canister through an insulated transfer tube and is delivered to the heat exchanger. The gas returning from the heat exchanger is used to cool the radiation shield of the cryostat and then flows along the flexible section of the transfer tube to the exhaust port, thereby shielding the incoming liquid from thermal radiation. Either liquid helium or nitrogen can be used. Liquid nitrogen allows to reach temperatures down to about 77 K, while using helium it is possible to maintain temperatures around 4.2 K by continuously pumping the transfer tube. The measurements taken for this work were all performed either with liquid nitrogen or without cooling. The temperature sensor and the heater are mounted in the heat exchanger and are both controlled by an external temperature controller, the Oxford Instruments ITC503. The temperature controller can also control the flow of cryogenic liquid in the cryostat by acting on the motorized needle valve at the bottom of the dewar leg of the transfer tube.

It is important to remark that below 90 K nitrogen tends to collect in the heat exchanger and boil only intermittently. In this case the temperature measured can be slightly

different from the actual sample temperature, since the heat sensor is placed in the heat exchanger as well.

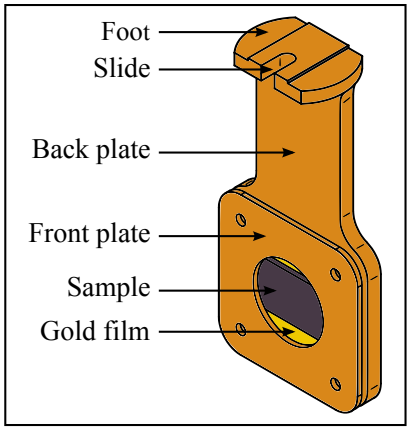

Figure 2.8: The sample holder

The sample is fixed to a sample holder, which is directly screwed on the bottom of the heat exchanger of the cryostat by a retaining screw. A groove in the cold finger prevents the sample holder from rotating during adjustment. The angular alignment with respect to the windows is chosen when closing the cryostat. Eight different positions are possible: parallel to each of the windows or forming a 45° angle with respect to a couple of windows. The sample holder has been self-designed and produced at the mechanical workshop of the Fritz Haber Institute. Figure 2.8 describes the principal parts of the sample holder. The main part is constituted by the back plate, which has been milled from a single piece of copper. The foot presents a protrusion, matching the groove in the cryostat heat exchanger, and a slide, where the retaining screw is inserted. This allows to adjust the distance between the sample and the windows. The sample is clamped between back and front plate, and a gold film has been inserted between it and the back plate to improve the thermal contact. A second version of the sample holder, with a window in the back plate as well, has been designed to allow measurements in transmission.

2.5 Characterization of the sample

The VO_2 sample used is a 200 nm thin film grown by Haglund and coworkers[3] using Pulsed Laser Deposition (PLD) onto *n*-doped silicon cut along the (100) surface. The *c* axis of the vanadium dioxide cell is directed perpendicular to the surface, i.e. the exposed VO_2 surface is the (001).

It is demonstrated that the thickness of the films [PV10, NH08], the presence of chemical impurities [CK10, SCH+04], as well as the formation of surface defects and cracks during the thermal induced transition can influence the transition temperature and the width of the hysteresis, which can eventually disappear. Therefore, the width and the position of the hysteresis curve represent a good way to characterize the sample.

To avoid local heating effects due to the high pulse intensity of the pump, a negative time delay of −500 fs is applied, i.e. the probe pulse reaches the sample before the pump. During the measurement the temperature is changed in the range between 323 K and 350 K. A voltage of 12 V, corresponding to the 30% of the maximum voltage, is applied to the heater and the sample is counter-cooled with liquid nitrogen at 16% of the needle-valve aperture.

The temperature dependence of the reflectivity of the 200 nm sample is plotted in figure 2.9. During heating (red curve) the insulator to metal transition occurs at a critical temperature $T_c^{\mathrm{up}} = 343\,\mathrm{K}$, while during cooling (green curve) the metal to insulator transition occurs at $T_c^{\mathrm{down}} = 333\,\mathrm{K}$, resulting in a 10 K wide hysteresis curve. The different absolute value of the reflectivity in the insulating phase, being lower if the sample is being cooled, is probably due to the position of the temperature sensor. Indeed, if we repeat the measurement after waiting for the temperature to stabilize at 320 K, the curve of Fig. 2.9 is reproduced. Due to its position between the cooling head and the sample holder, the sensor can measure a lower temperature than the one at the sample surface. Thus, the measured reflectivity corresponds to the value at

[3]Department of Physics and Astronomy, Vandebilt University, Nashville, Tennessee (USA)

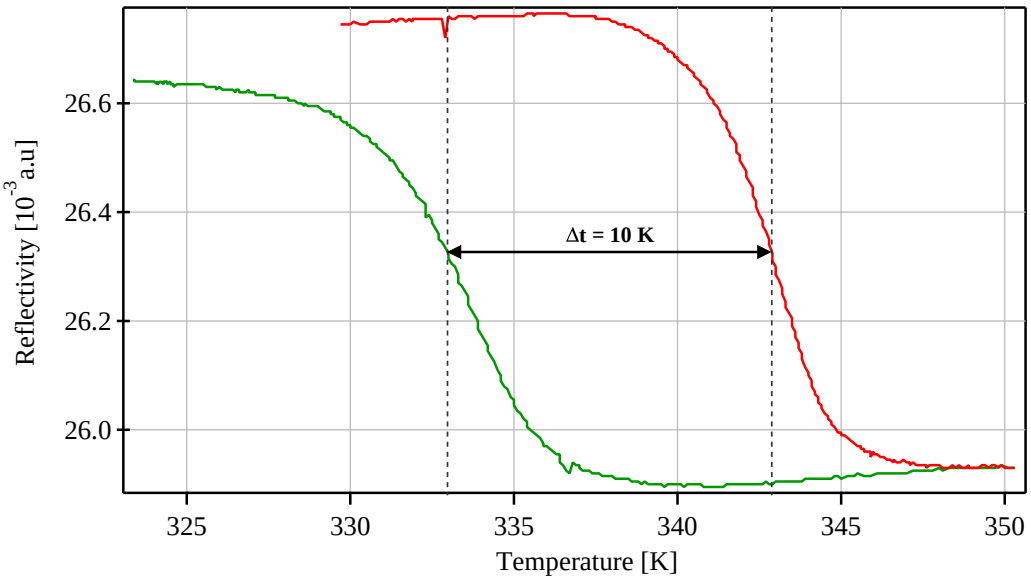

Figure 2.9: The hysteresis curve of the VO_2 sample is 10 K wide. (red curve) Heating process: the transition occurs at 343 K. (Green curve) Cooling process: the transition is at 333 K.

higher sample temperatures. This does not occur in the high temperature part of the curve because the temperature gradient between heat exchanger and sample holder is smaller during the heating process [Oxf05]. Another explanation for the difference between the absolute values of the reflectivity, which is sometimes encountered in literature [VBB68], is that the lower final reflectivity is due to defects and cracks forming on the sample after the phase transition. This is less plausible in thin films since they are usually more resistant to the phase transition than bulk crystals [NH08].

3 Experimental results and discussion

The transition from metallic to insulating vanadium dioxide occurs in our sample at 333 K on cooling, as shown in section 2.5. The reverse transition, from the monoclinic to the rutile phase, can be induced by photoexcitation (Sec. 1.3.3). There are still many open questions regarding the mechanism driving the transition and the nature of the photoinduced phase. As will be shown in the following, ultrafast time-resolved optical experiments can help to answer some of them.

In this work we measure the pump-induced changes in the reflectivity as a function of excitation fluence. The measured traces exhibit a modulation due to coherent lattice excitations. From the analysis of these coherent phonons dynamics we gain insight into the changes of the lattice symmetry of VO_2 at the onset and during the phase transition. To have access to the oscillatory part, we have removed the incoherent contributions to the reflectivity by fitting a double exponential decay, which results into a fast and a slow component (cf. 3.1.1). The fast component is related to the electronic sub-system and the slow one to the lattice sub-system. The amplitude of the reflectivity changes as a function of excitation fluence, because the two components show different dynamics . While the fast component increases linearly over the whole range, the slow part shows a discontinuity at a fluence threshold of $\Phi_c = (6.5 \pm 0.4)\,\mathrm{mJ\,cm^{-2}}$, after which it increases abruptly. In analogy to Ref. [CTS+01, KEH+07], we associate this threshold with the occurrence of the phase transition. This is supported by the dynamics of the coherent part, as shown in Sec. 3.1.2. In the Fourier transform of the oscillations we observe, for excitation below threshold, four optical modes that correspond to the four lowest A_g modes of the monoclinic phase. Close to the threshold these modes become undetectable, while a broad peak emerges, with amplitude and damping rate one order of magnitude larger than the low fluence modes. It will be proposed that

the electronic excitation is sufficient to modify the crystal potential (cf. sec 3.1.2). The initial response of the lattice is therefore no longer defined. This picture will be supported by the pump-pump-probe experiments shown in Sec. 3.2.

3.1 Transient Reflectivity on VO_2

The transient reflectivity measurements were performed at room temperature using the configuration described in Fig. 2.2(a) of Sec. 2.2. The experiments have been carried on at two different repetition rates, 150 and 300 kHz. Due to the difficulties in determine the pulse area of the high repetition rate spot explained in section 2.3, the analysis has been done on the low repetition rate data. Furthermore, at a higher repetition rate, we cannot exclude local heating effects, since the maximum average power is around 500 mW. Nevertheless, the 300 kHz data are qualitatively presented in section 3.3. The transient reflectivity traces are shown in figure 3.1(a). The changes

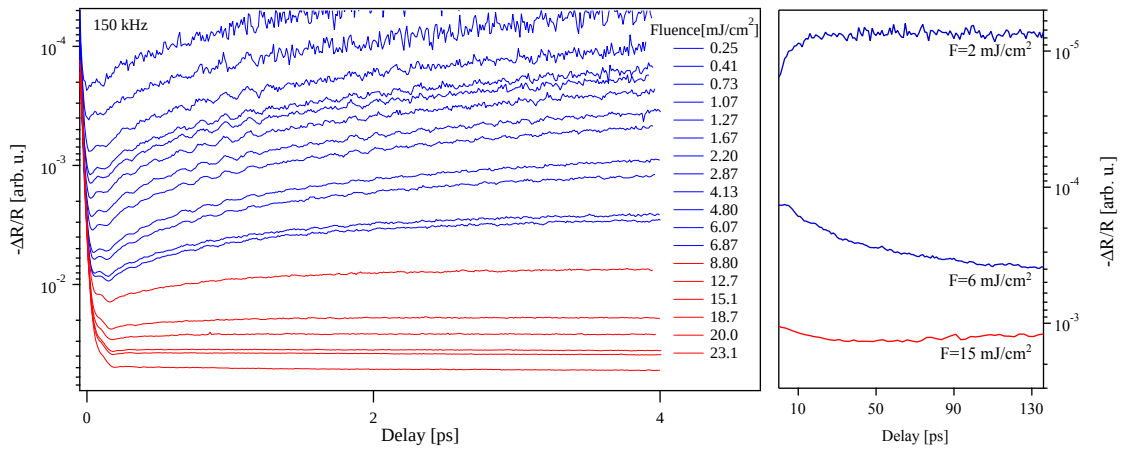

Figure 3.1: Time dependence of the reflectivity of VO_2 for different fluences. The values of the fluence are reported in the legend. The different colours indicate fluences below (blue) and above (red) the threshold for the phase transition, according to the definition discussed below and in analogy to Ref. [CTS+01, KEH+07] .

in the reflectivity are plotted on a logarithmic scale versus the delay between pump and probe pulse. The fluence was varied between 0.25 and 23 mJ cm^{-2} and the values for each curve are reported in the legend. The different colors indicate traces measured above (red) and below (blue) a fluence threshold, which has been defined in analogy to Ref. [CTS+01, KEH+07], as described below.

In all traces, we observe a fast rise at time zero, followed by a slow decay that lasts over several hundreds of picoseconds, as confirmed from the traces in panel (b). They show the transient reflectivity scans at longer time delay for three selected frequencies, reported in the figure. The prompt rise is due to the excitation of the electronic system due to the incident laser pulse. The electrons, then, couple to the lattice, causing an additional change in the reflectivity. The reflectivity transients due to the two sub-systems can be related to the amplitude of the signal measured at 60 fs and 1 ps, respectively. These values are plotted as a function of fluence in figure 3.2. The reflec-

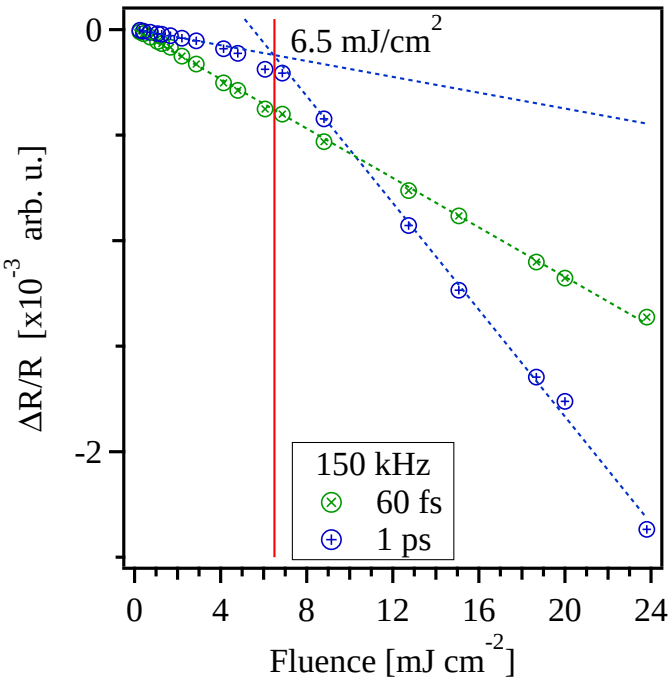

Figure 3.2: Fluence dependence of the reflectivity at 60 fs and 1 ps, measured with 150 kHz repetition rate. The early amplitude shows a linear dependence, while the amplitude at 1 ps shows a discontinuity at a fluence threshold of (6.5 ± 0.4) mJ cm^{-2}.

tivity change is reported on the left axis, while the bottom one represents the values of the fluence. Their fluence dependence exhibits different trends. The fast component is linear over the whole fluence range, as previously shown e.g. by Leitenstorfer and co-workers [KEH+07]. The slow component instead, grows linearly until a critical fluence value, where its slope changes abruptly. A similar behaviour was observed in Ref. [KEH+07] for the THz conductivity and has been related to the occurrence of the photoinduced transition.

The *fluence threshold*, or critical fluence, is calculated as the intercept between the two dependencies and the obtained value is $\Phi_c = (6.5 \pm 0.4)\,\mathrm{mJ\,cm^{-2}}$[1]. The value obtained is slightly larger than the one found in Ref. [KEH+07] and it is most likely due to the larger sample thickness.

At a close observation, the transient reflectivity traces are modulated by high amplitude oscillations, due to the coherent excitation of the lattice by the ultrashort laser pulse. In order to be able to analyse these oscillations the incoherent response has to be subtracted.

[1] The error is calculated comparing the threshold with the value obtained from the fits of the amplitudes discussed in Sec. 3.1.1

3.1.1 The incoherent component

The incoherent contributions in the traces of Fig. 3.1 have been fitted with a double exponential decay

$$\Delta R(t) = \Theta(t)\left[R_e e^{\frac{-t}{\tau_e}} + R_l\left(1 - e^{\frac{-t}{\tau_e}}\right)e^{\frac{-t}{\tau_l}}\right] \tag{3.1}$$

Here R_e and τ_e are, respectively, the amplitude and decay of the fast component and R_l and τ_l the ones of the slow component. As mentioned in the previous section, they are associated to the electronic and lattice response, correspondingly. In this picture R_e and τ_e represent the amplitude and the decay time of the reflectivity change due to the electrons which have been excited by the laser pulse. The electronic system couples to the lattice, causing an additional change in the reflectivity R_l, which decays with time constant τ_l. The function $\Theta(t)$ is an error function defined as

$$\Theta(t) = \frac{1}{2}\left[1 + \mathrm{erf}\left(\frac{t}{\tau_r}\right)\right] \tag{3.2}$$

and is used to approximate the rising edge due to the correlation between the pump and probe pulse at $t = 0$. Here τ_r represents the duration of the pulses.

Figure 3.3 shows the fits of the incoherent contributions for three different values of the fluence, being much lower, close to and higher than the fluence threshold. These curves are representative of three different fluence regimes, which we refer to as low, intermediate and high fluence regime.

On the left axis are reported the values of the reflectivity change in arbitrary units, while on the bottom axis the time delay between pump and probe pulse is shown in picoseconds.

The data is displayed by the blue circles and the fits are depicted as red solid line. The contribution of the fast and the slow component to the incoherent background is shown by the dotted blue lines. They confirm that the electronic (fast) response is responsible for the abrupt change at zero time delay and then decays rapidly to zero. On the same timescale the slow component increases, due to the energy transfer

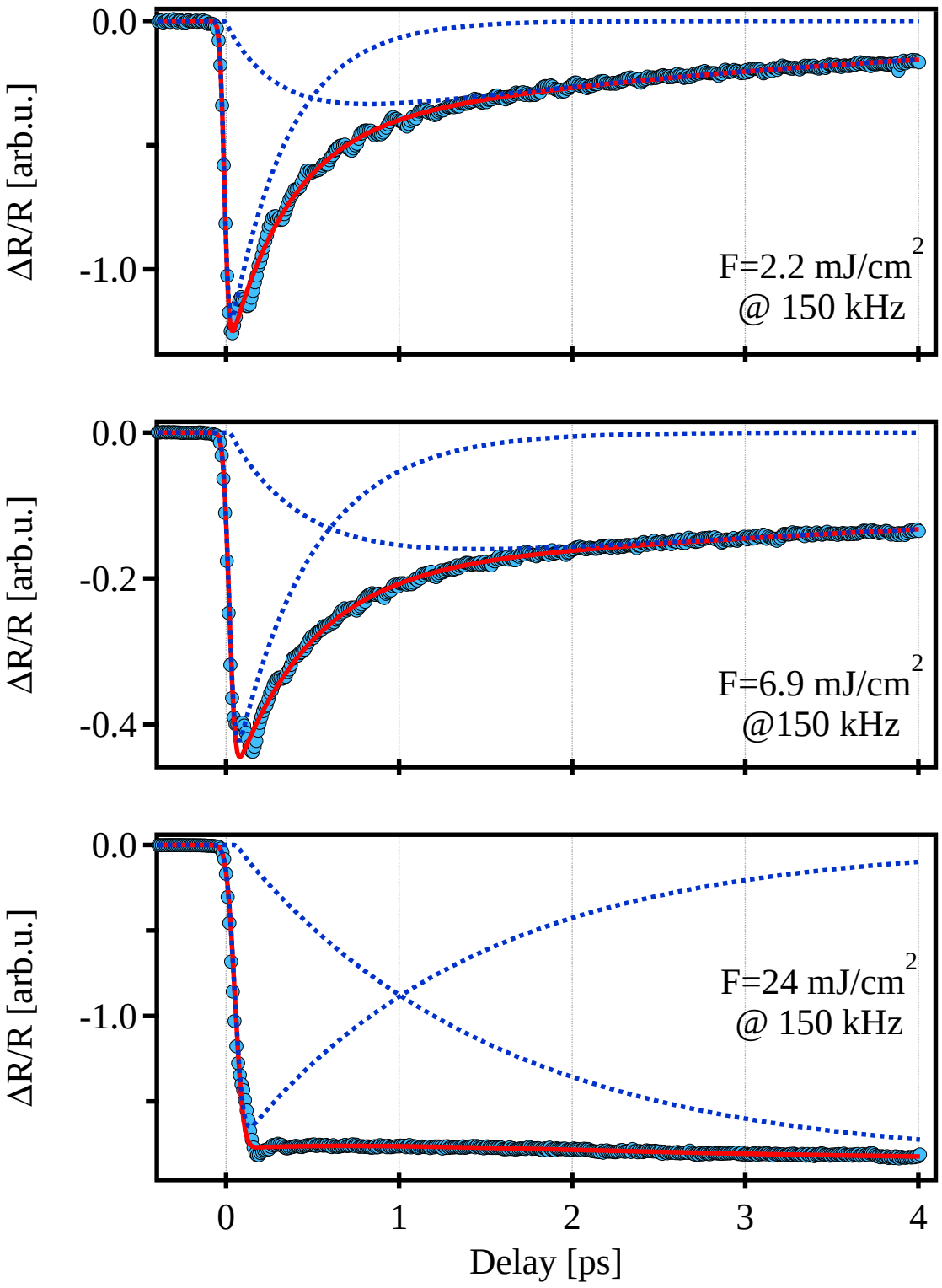

Figure 3.3: Fits of the incoherent contributions with Eq.(3.1) for three different frequency regimes: low, intermediate and high. The dotted blue lines indicate the fast and the slow components, related respectively to the electronic and lattice contribution.

between electronic and lattice system, and the long-lived excited state relaxes on the much longer timescale τ_l.

The results of the fit for the amplitudes R_e and R_l are reported as a function of fluence in Fig. 3.4. As expected, the electronic and the lattice component exhibit the same fluence dependence than the amplitudes at 60 fs and 1 ps, respectively. The blue line indicates the value of the fluence threshold. Again we calculate the intercept between the linear extrapolation of the points before and after the discontinuty to determine the value of the critical fluence, which in this case was found to be slightly higher than the one reported above. This deviation has been used to define the error bar for Φ_c.

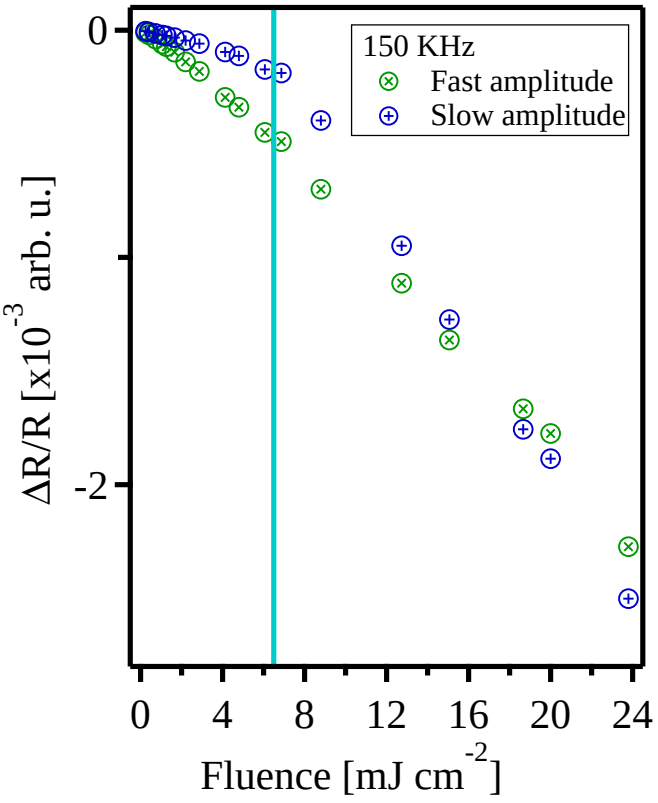

Figure 3.4: Fit results for the fast (electronic) and slow (lattice) amplitudes as a function of fluence. They exhibit the same behaviour as the 60 fs and 1 ps amplitudes respectively. The vertical line indicates the fluence threshold.

Figure 3.5 shows the decay times as a function of fluence for the fast and the slow

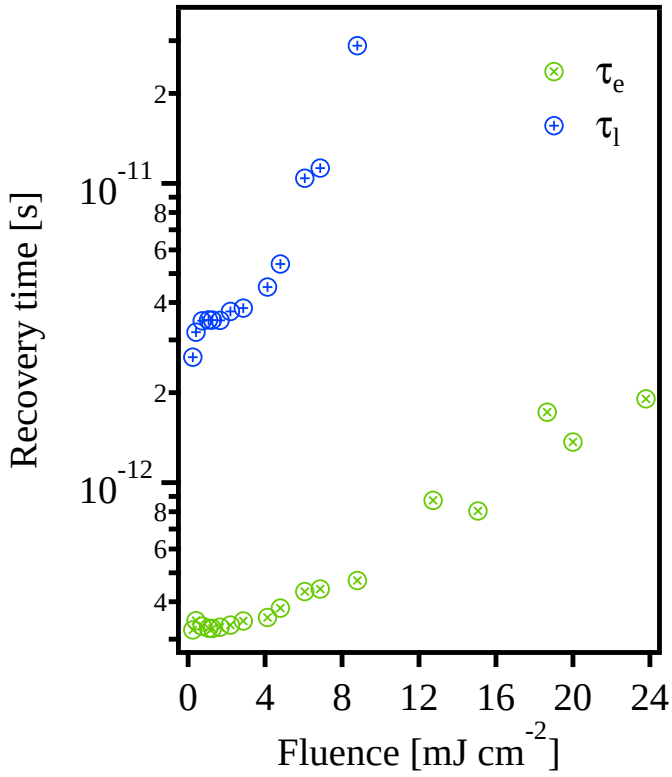

Figure 3.5: Fit results for the fast (electronic) and slow (lattice) decays as a function of fluence. They show a divergence above the threshold fluence indicating a change in the dynamics of both electron and lattice system above the transition.

component, respectively. The values of τ_l beyond $10\,\mathrm{mJ\,cm^2}$ are not shown since the duration of the time scans is not sufficient to fit this parameter. Both time constants increase slowly until the threshold fluence is reached and then increase rapidly. This divergence is indicative of a change in the dynamics across the phase transition.

3.1.2 Generation of coherent phonons

The traces in Fig. 3.3(a)–(c) show that the reflectivity is modulated by oscillations of high amplitude. This is due to the coherent excitation of phonon modes of the system. To study the dynamics of the oscillations the fit of the incoherent contribution has been subtracted from the raw data.

The left-hand panels of figure 3.6 show the background-subtracted oscillations and the right-hand panels the modulus squared of the Fourier transform (FT). Qualitatively, the amplitude of the oscillations increases with fluence. Furthermore, above fluence threshold, a large amplitude oscillation appears in the early dynamics. It persists only for a few cycles. Then, just the low-amplitude oscillations appear in the traces. This is supported by the Fourier transforms, which show four peaks in the low fluence regime. They have been labeled following the frequencies of the normal modes measured in Ref. [Sch02] and reported in table 1.1. In the intermediate regime, i.e. close to the fluence threshold, only the most intense Q_2 and Q_3 modes are detected and a wider peak appears. It has been labelled Q_{HF} to distinguish it from the phonons of the monoclinic

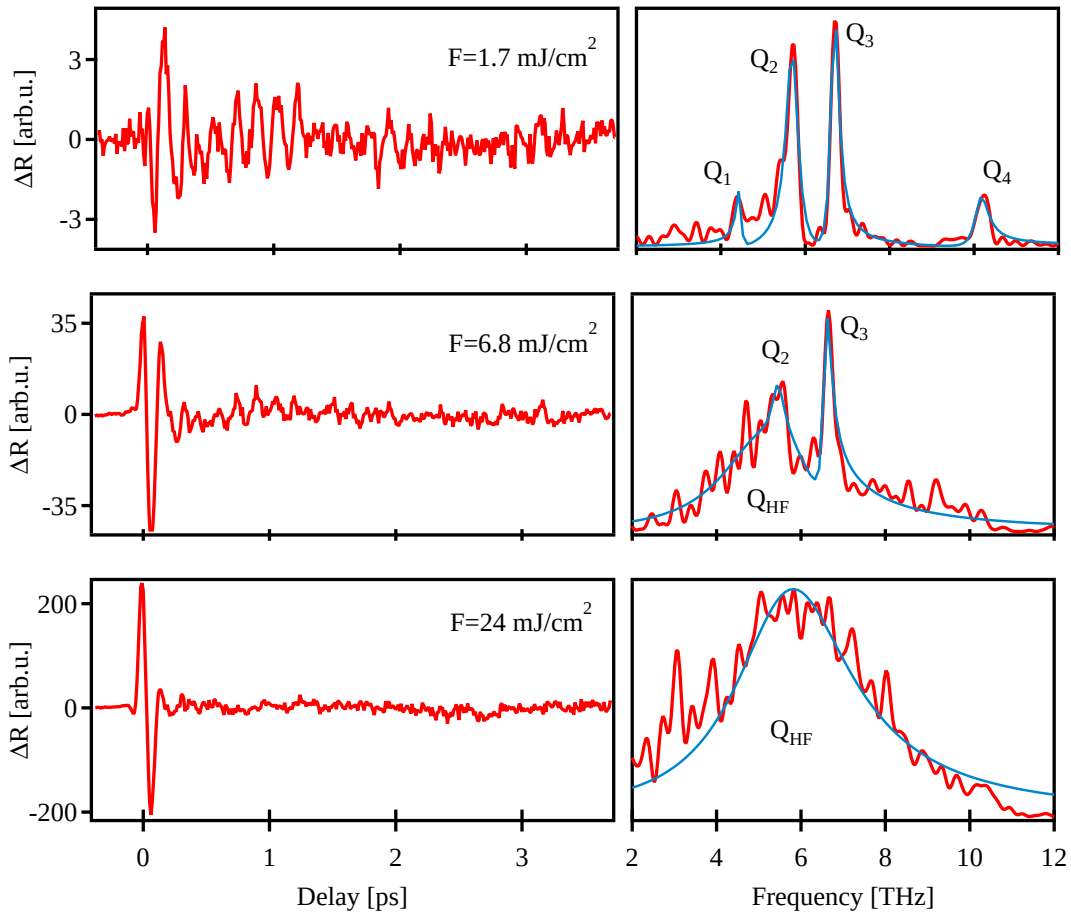

Figure 3.6: Oscillations in the reflectivity (left panels) and the corresponding modulus squared of the Fourier transform. The blue lines show the Lorentzian fits.

phase. This broad peak is the only one visible in the high fluence regime.

The quantitative analysis has been performed by fitting the squared absolute value of the FT with a sum of Lorentzians,

$$|F(\omega)|^2 = \left| \sum_j \frac{A_j^2(\omega - \frac{\Gamma_j}{2\pi} i)}{\omega^2 - \omega_j^2 - (\frac{\Gamma_j}{2\pi})^2 + \omega \frac{\Gamma_j}{2\pi} i} \right|^2 . \tag{3.3}$$

where A_j is the amplitude of the mode of frequency ω_j and Γ_j its damping rate. A maximum of five modes was used to fit the FT spectra. The fitting has been carried on iteratively. On a first step the fit interval was constrained to a finite region of the FT spectrum and all parameters were allowed to vary. Due to the overlapping of the wings of the Lorentzians, the fit of a mode influences all the neighbouring peaks. Thus, a final optimization was performed, allowing only the amplitudes to vary. In some spectra of the intermediate and high fluence regime, sharp peaks can be observed, which do not show any systematic dependence on the fluence, either for the frequency, the amplitude or the damping rate. Their frequency does not correspond to any of the modes of VO_2 suggesting that they were arising from noise. Indeed, they disappear if we shift of only a few points the range on which the Fourier transform is calculated.

In the low fluence regime four different phonon modes can be observed at 4.47, 5.6, 6.65 and 10.1 THz, in good agreement with the lowest A_g modes of the monoclinic phase measured in Ref. [Sch02]. None of these modes can be assigned to the rutile phase. This strongly suggest that in the low fluence regime no major change is induced in the symmetry of the potential and only modes of the monoclinic phase can be excited. Figure 3.7 shows the coherent phonon frequencies resulting from the fits as a function of fluence, reported on a logarithmic scale.

The full markers put in evidence those modes which appear stronger in the Fourier transform. They are the Q_2 and Q_3 modes, corresponding to the modes at 5.72 and 6.69 THz of the M_1, and the Q_R in Fig. 3.6. Looking at their fluence dependence one can see that Q_2 and Q_3 are present over the whole low and intermediate fluence range, but disappear at high fluence. At the same time a new peak appears, having a fre-

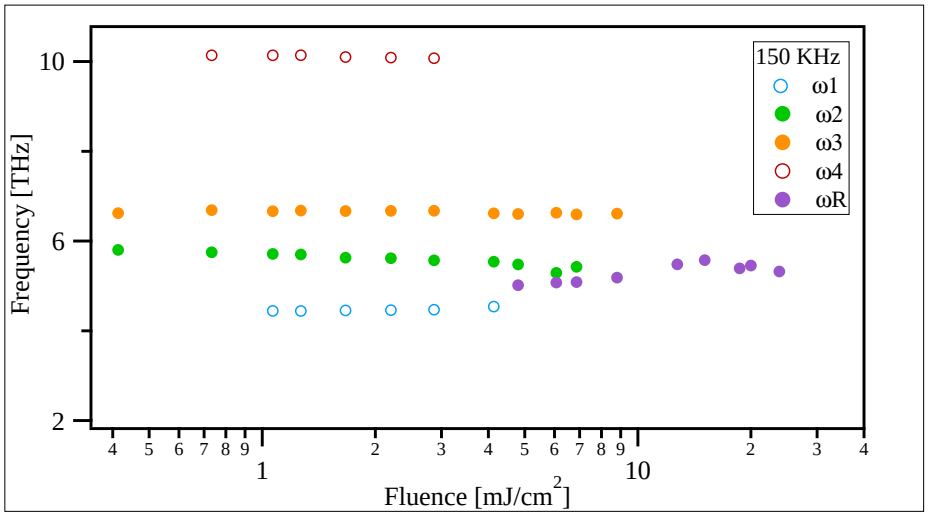

Figure 3.7: Coherent phonons frequencies obtained from the Lorentzian fit of $|F(\omega)|^2$. Full markers indicate those modes which are stronger in the Fourier transform and visible over the whole low and intermediate fluence range.

quency around (5.3 ± 0.3) THz. Before this point, the frequency of all the modes is approximately constant, with only the Q_2 mode showing a small redshift for increasing fluence[2].

Mayor details on the origin of the broad peak and the disappearing of the modes related to the monoclinic phase can be obtained by looking at the fluence dependence of the amplitude and the damping rate.

The behaviour of the amplitudes can be seen in figure 3.8. Again, the fluence is plotted on a logarithmic scale and the labelling and colour scheme reflect those of the previous plot. To improve the visibility, the markers have been connected by lines. It is remarkable that the amplitude of the low-fluence modes increases monotonically whith fluence until the broad high-fluence peak appears. Its amplitude is about one order of magnitude larger and continues rising with the fluence, while the low-fluence modes suddently become undetectable.

[2]Due to the different film thickness the frequencies obtained differ from those in Ref. [KLK+06]. We plan to repeat the experiment on thinner films to compare the results.

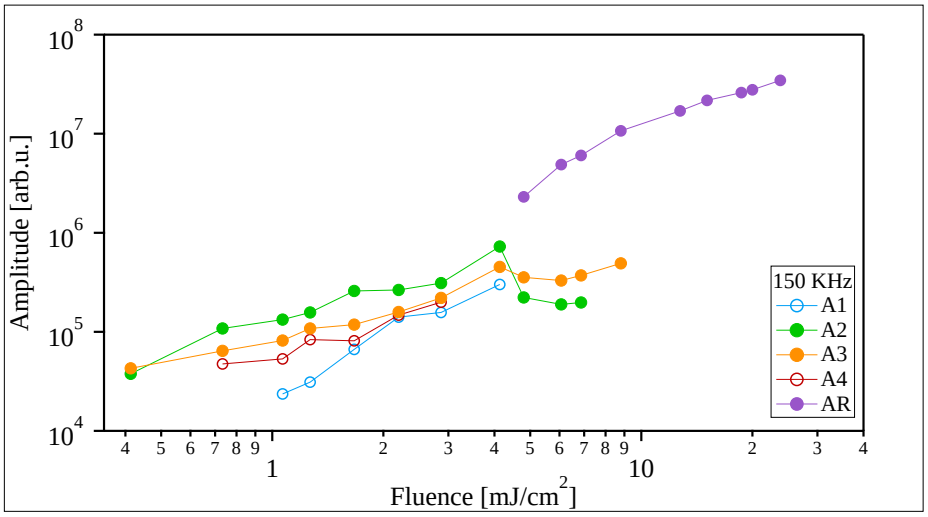

Figure 3.8: Amplitudes of the coherent phonon oscillations obtained from the fit with eq. 3.3. The markers follow the same notation as in Fig. 3.7. All amplitudes increase monotonically with fluence.

The most important considerations arise after analysing the behaviour of the damping rates, which are plotted in figure 3.9. The damping rate of the Q_2 and Q_3 modes is Γ_i =0.19(4) and 0.12(2) ps^{-1}, respectively, and do not depend on the fluence. The

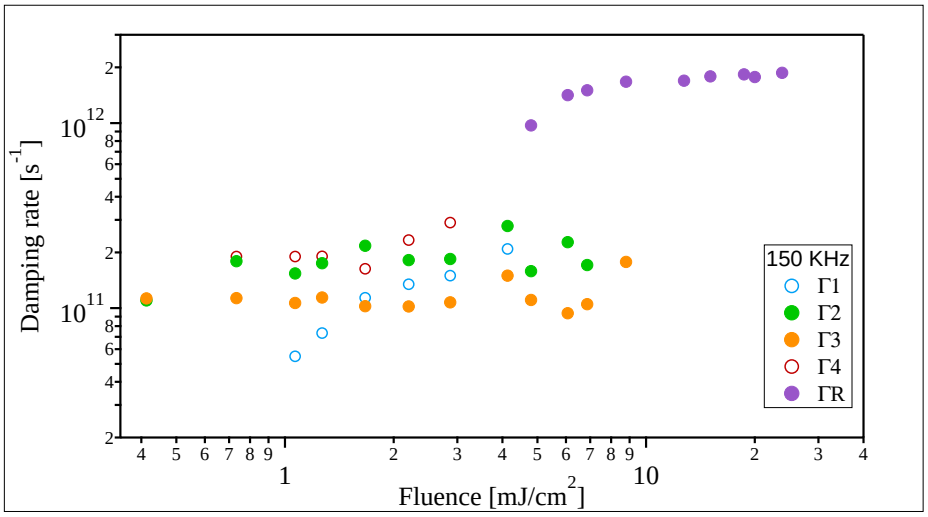

Figure 3.9: Damping rate of the coherent phonon oscillations obtained from the fit with eq. 3.3. The markers follow the same notation as in Fig. 3.7. All damping rates are almost constant. The high-fluence mode has a damping rate almost one order of magnitude larger.

damping rate of the Q_{HF} mode is instead $1.6(3)\,ps^{-1}$, again one order of magnitude larger than those of the low-fluence modes. The fluence dependence of Γ_1 and Γ_2 strongly suggests that a dephasing of the M_1 phonons due to electron-phonon scattering is not causing the appeareance of the broad peak. Thus, the phase transition must be at its origin.

Although the damping rate of the high-fluence mode is consistent with the modes observed in the rutile phase, its frequency does not correspond to any of these modes, since the lowest is at 7.2 THz. We strongly believe that it is due to the projection of the initially excited M_1 modes onto the coordinates defined by a new lattice potential. A more detailed discussion is given at the end of this section.

To determine the excitation mechanism for the coherent phonons, we have fitted the oscillations curves for amplitudes below threshold with a sum of damped cosine oscillations of the form

$$\Delta R = \Theta(t) \sum A_j e^{-\Gamma_j t} \cos(2\pi\omega_j) \tag{3.4}$$

The frequency ω_j was set to the results of the Fourier transform, while the amplitude A_j and damping rate Γ_j were allowed to vary. The best fit was found to be when there is no phase shift from a cosine behaviour, indicating that the excitation mechanism is displacive. This confirms the previous observations on VO_2 [KLK+06]. Figure 3.10 shows an example for a trace at a fluence of $1.7\,mJ\,cm^{-2}$.

Summarizing, below the fluence threshold, we find four phonon modes whose frequency and damping rate are almost independent on fluence and whose amplitude monotonically grows with fluence. The frequency of these modes is in agreement with the lowest A_g modes of the monoclinic phase. At the threshold a new mode appears. Its amplitude is one order of magnitude larger and continue increasing with fluence, while the other phonons are suddenly undetectable.

What do this results tell about the metal-to-insulator transition?
At low fluences we are in a situation where the excited electrons exert forces on the lattice, which responds oscillating with modes of frequency dictated by the symmetry of

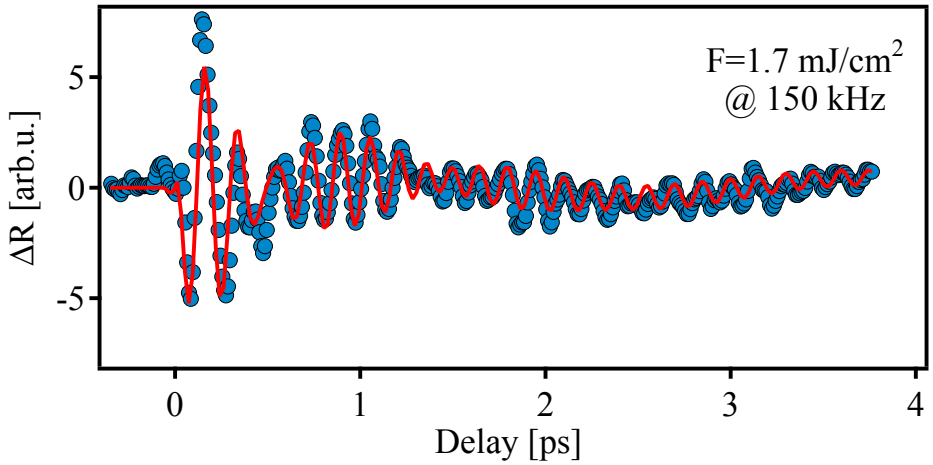

Figure 3.10: Example of the fit with damped cosine oscillations of a low fluence trace measured at 150 kHz. The best agreement was found to be when there is no phase shift from the cosine behaviour, showing that the excitation mechanism is displacive.

the lattice potential. The fact that the all excited modes correspond to normal modes of the M_1 phase means that the electrons perturb only weakly the lattice potential. Since the damping rate of the M_1 phonons does not increase with fluence, we cannot attribute the broad peak above threshold to a dephasing of the low-fluence modes due to electron phonon scattering. Therefore, above threshold a phase transition must be triggered, which raises the symmetry of the potential and reduces the number of Raman-active modes. Two scenarios could be proposed for explaining the origin of this transition.

In the first, the electrons are not responsible of the transition, which is triggered by a temperature increase of the lattice. The energy transferred from the electronic to the lattice system increases the lattice temperature above the critical temperature T_c for the transition. Once the system is above T_c, the lattice potential changes and the phonons of the M_1 phase are no longer defined. In this scenario, the initially excited normal modes of the monoclinic phase should exhibit an increasing broadening. For sufficiently high fluence, the damping would be fast enough to make them overlap in frequency space, forming a single broad peak. The time t_c necessary to reach the critical temperature depends on the initial temperature difference between the two

systems and thus decreases for increasing fluence. Broadening occurs only if $t_c < 1/\Gamma$. Therefore this model is not supported by the experimental results: Ref. [Bau07] shows that it takes several hundreds of picoseconds for the lattice ions to reach their final position and we do not observe any change in the damping rate of the low-fluence phonons. Furthermore, the appearance of Q_R occurs suddenly with the fluence and it is not a gradual variation in amplitude, as it would be expected in a thermal scenario.

The second scenario assumes that the electronic excitation is sufficient to modify the lattice potential. In this case the potential changes even before the lattice ions have started their motion. Phonons of the M_1 phase are excited by the rising edge of the pulse until the absorbed fluence crosses the threshold for the transition. At this point the symmetry of the potential is changed and the original restoring forces at the M_1 phase frequencies are no longer defined. The lattice motion originally generated by the laser pulse is transformed into a superposition of the modes defined by the new potential, resulting in the broad peak observed in the Fourier transform. This scenario would imply that, already at times close to time zero, it would be impossible to excite the modes of the M_1 phase again. In order to prove that, we have performed a double-pump experiment, which is the subject of the next section.

3.2 Switching the phonons on and off: a pump-pump-probe experiment

To perform the two-pump experiment we have used the setup of figure 2.2b, which adds a Mach-Zehnder interferometer to the pump path. The sample was excited successively by two collinear pump pulses with variable delay. The experiments have been performed at a repetition rate of 150 kHz.

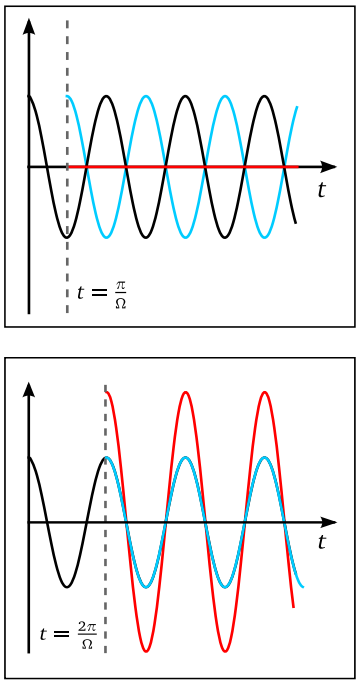

Figure 3.11: Schematic illustration of coherent control. See text for details.

We have focused our attention on the Q_3 phonon of the monoclinic phase, having a period of around 150 fs (ω_3 =6.65(4) THz). The first pump excites the sample and generates coherent phonons at the Γ point. They accumulate phase with time and can interfere constructively or destructively with the phonons generated by the second pump, depending on the time delay between the two pump pulses. Destructive interference is expected for a delay of 75 fs and it should result in a reduction of the phonon amplitude in the Fourier transform. In case of in-phase excitation, Δt =150 fs, the amplitude should increase. A schematic of this technique, called *coherent control*, is given in figure 3.11. The curves in the top panel illustrate the out-of-phase situation, i.e. the second pump is delayed by $\Delta t = \pi/\Omega$, where Ω is the angular frequency of the phonon mode. The black curve represents the amplitude of the phonons generated by the first pump pulse, while the blue curve the amplitude of those generated by the second. The resulting amplitude, shown by the red line, vanishes. In the bottom panel the in-phase excitation is represented. Again the black

and blue curves represent the amplitude of the phonons excited by the first and second pump pulse, respectively. The delay between the pulses is $\Delta t = 2\pi/\Omega$ and the resulting amplitude (red curve) is doubled.

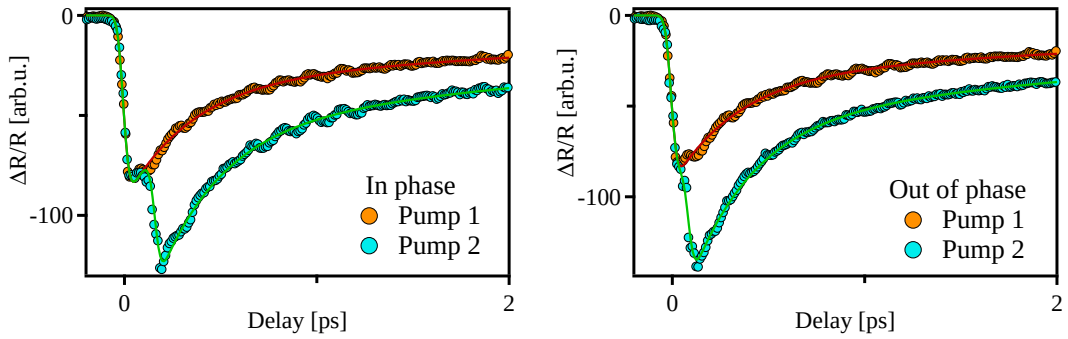

(a) Pump 2 in phase **(b)** Pump 2 out of phase

Figure 3.12: Transient reflectivity traces of the double pump experiment for excitation below fluence threshold. Coherent phonons excitation modulate the transient reflectivity if the sample is excited in phase and do not if it is excited out of phase.

The transient reflectivity traces measured at a fluence below Φ_c are plotted versus time in figure 3.12. Panel (a) depicts the case where the second excitation is in-phase. The orange circles label the measurements done with one single pump pulse and the blue ones the double pump measurement. Both the single pump trace and the double pump trace are modulated by strong oscillations. The out-of-phase case is presented in panel (b). Again the orange trace is measured with single pump excitation and the blue one with double pump. While the oscillations are visible in the first case, in the second they are strongly reduced. It is important to remark that the coherent control acts only on the Q_3 mode and the oscillations due to the other modes should still be visible.

To confirm our qualitative observation, the transient reflectivity traces have been fitted with two copies of equation (3.1), shifted by the proper time delay. They are plotted as green and red curves in figure 3.12. The results of the fits have been subtracted from the raw data to obtain the background subtracted oscillations shown in Fig. 3.13. Panel (a) shows the single pump response. Here, the laser pulse excites coherent modes at

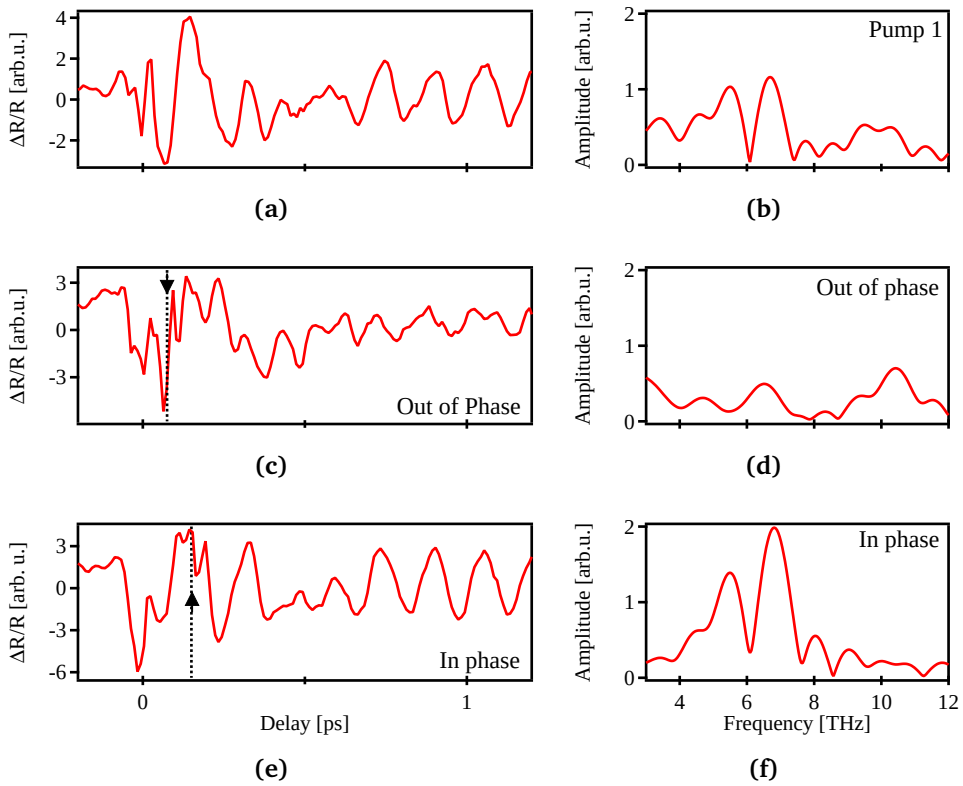

Figure 3.13: Background-subtracted oscillations in the double pump experiment and the corresponding Fourier transforms for excitation below fluence threshold. (a)–(b) Single pump excitation for comparison. (c)–(d) The 2nd pump reaches the sample out of phase (Arrow at $\Delta t = 75\,\text{fs}$). The oscillation is quenched. (e)–(f) The 2nd pump reaches the sample in phase (arrow at $\Delta t = 150\,\text{fs}$. The oscillation is amplified.

$t = 0$, which start oscillating. These oscillations are at the maximum displacement after half a period. If the second pump reaches the sample exactly at that time (75 fs) the ionic equilibrium position is shifted in such a way that any further motion is suppressed. This case is presented in panel (c), where the arrow indicates the time at which the second pump reaches the sample. The oscillations that are still visible in the trace correspond to the motion associate to the other phonon modes. Indeed, the peak at around 6.6 THz, related to Q_3, disappears from the Fourier transform, as shown in panel (d). On the other hand, if after the first excitation the phonons are allowed to oscillate for a full period of 150 fs before the second pulse arrives, the situation is

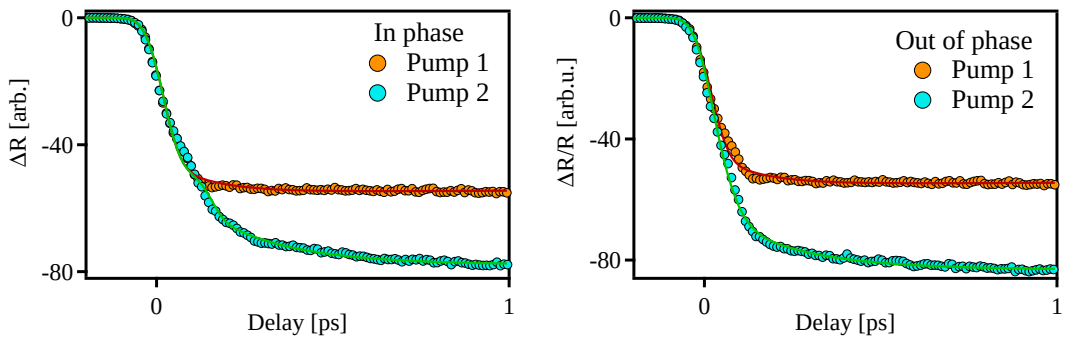

(a) Pump 2 in phase

(b) Pump 2 out of phase

Figure 3.14: Transient reflectivity traces of the double pump experiment for excitation above fluence threshold. No evident difference can be seen between the traces.

completely different. Here, the ions are again at the minimum displacement and the shift of the equilibrium position increases the amplitude of the oscillations. This can be seen in panel (e): after the line indicating Δt =150 fs the oscillations are more visible. The 6.6 THz peak in the Fourier transform doubles approximately in amplitude with respect to the single pump case, confirming the observations.

The same experiment has been performed for excitation above fluence threshold. In this case it was not possible to have the same intensity in both the pump beams, since the system would have not recovered within the repetition rate of the laser. Thus, the fluence of the first pump pulse was set to be 20 mJ cm^{-2}, well above the transition threshold, and the one of the second pump was reduced (F =4 mJ cm^{-2}). The transient reflectivity traces are shown in Fig. 3.14 (a) for in-phase excitation and (b) for out-of-phase pumping.

The same color code as in figure 3.12 has been used: orange indicates the single pump response and blue the double pump one. The red and green lines represent the corresponding fits. Qualitatively, there is no major change between the single and the double pump excitation, for both the in-phase and out-of-phase cases. In addition the dynamics shows a continuous decrease in the reflectivity, being very different from the exponential recover observed below the critical fluence.

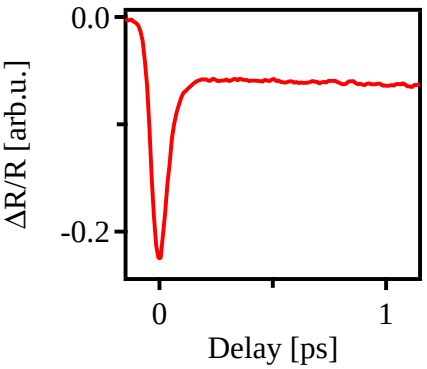

Figure 3.15: The transient reflectivity of the metallic phase. After the sharp spike at time zero the reflectivity decreases continously

This behaviour strongly resembles the one of the time-resolved reflectivity measured in the metallic phase at a temperature T =450 K (Fig. 3.15). There the system reacts with a sharp peak at time zero, followed by a continuous decrease of the reflectivity. This suggests that the first pump modifies the symmetry of the crystal to the one of the rutile phase.

The background subtracted oscillations and their Fourier transforms are used to quantify our qualitative observations. In analogy to the low-fluence experiment, the upper row of figure 3.16 shows the single pump response. The second and third row show the response to the second pulse excitation at Δt =75 fs and Δt =150 fs, respectively. Both the oscillatory traces and the Fourier transform confirm that the second pump does not modify the coherent response at either delay. This supports the suggestion that the first pump above fluence threshold has modified the lattice potential. If the symmetry would have stayed the same, the second pump would produce a second broad oscillation. If this were the case then the broadening would be due to an increase in damping. Instead, no coherent phonon are generated by the second pump.

The experiment is thus supporting the second scenario proposed in section 3.1.2, where the excited electronic distribution induces a distortion of the lattice potential, in opposition to a thermal scenario. The distortion of the potential causes the restoring forces for the phonon modes of the M_1 phase to disappear. Above fluence threshold, we observe that no coherent oscillations can be re-excited, demonstrating that the loss of the monoclinic phase phonons is not the result of an increased de-phasing and suggesting that the symmetry change *has* occurred.

To clarify the mechanism it is useful to refer to the model of the bi-atomic linear chain.

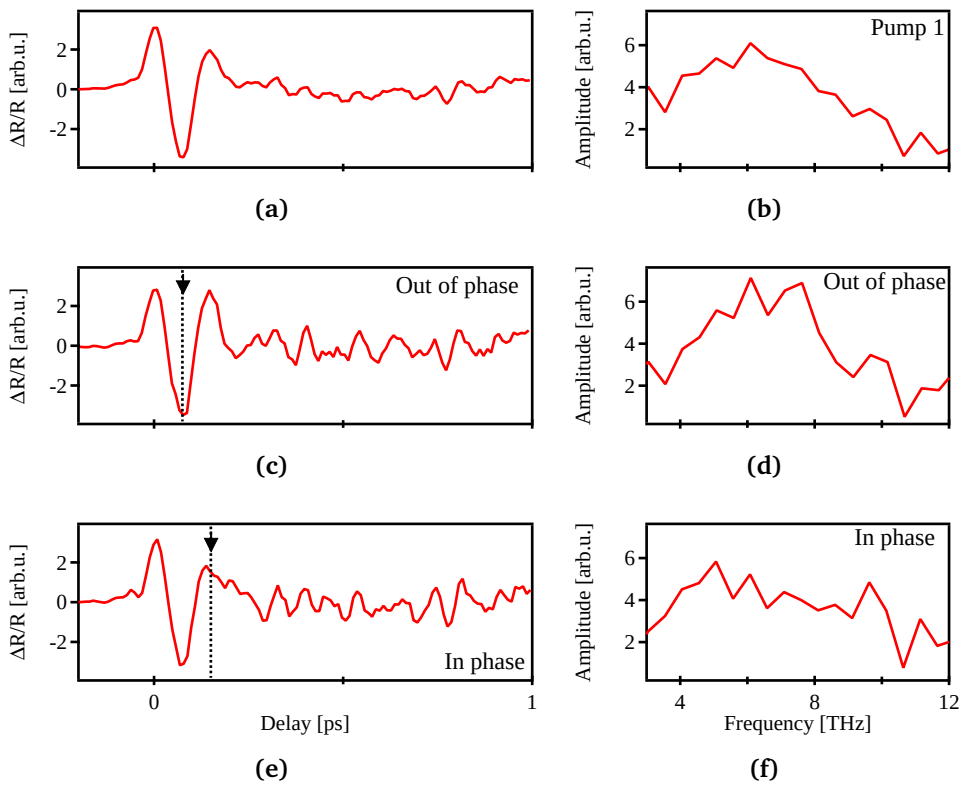

Figure 3.16: Background-subtracted oscillations in the double pump experiment and the corresponding Fourier transforms for excitation above fluence threshold. (a)–(b) Single pump excitation for comparison. (c)–(d) The 2nd pump reaches the sample out of phase (Arrow at $\Delta t = 75\,\text{fs}$). (e)–(f) The 2nd pump reaches the sample in phase (arrow at $\Delta t = 150\,\text{fs}$. In both cases no major change is noticeable either in the oscillation or in the Fourier transform.

Its phonon dispersion relation is shown in figure 3.17. An acoustical and an optical branch are obtained if the chain is formed by atoms with different masses. They are separated by a gap at the Brillouin zone (BZ) boundary. The gap, however, closes when the two masses are the same and the optical branch is no longer defined, preventing the excitation of the phonon modes associated to it. In this case, the symmetry of the system has raised and the BZ is double as large. In VO_2 the situation is analogous. The symmetry change, due to the excitation of the electrons by the laser pulse, leads to a raise in symmetry associated to a doubling of the BZ. This implies that the optical branches can be no longer defined. Indeed, the number of Raman active modes in VO_2

reduces from 18 to 5 upon the transition (cf. Sec. 1.3.1).

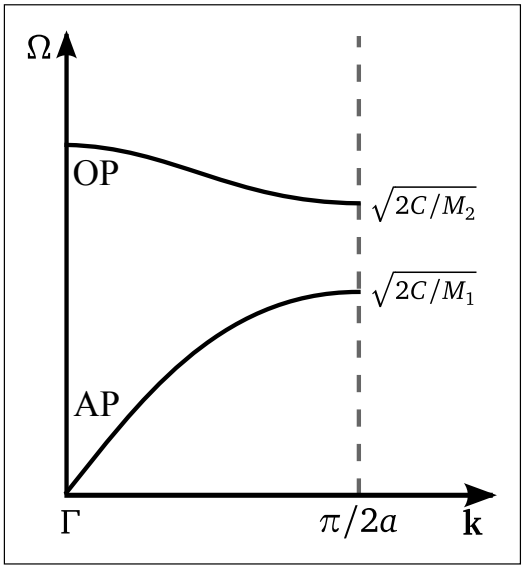

Figure 3.17: Acoustical and optical phonon branches of a bi-atomic linear chain of lattice constant $2a$. The limit frequencies at $\mathbf{K} = \pi/2a$ are reported. If the masses are the same, the symmetry of the system raises and the optical branch is no longer defined [Kit66].

Altough the potential has changed on an ultrafast timescale (<150 fs) the position of the ions is still far away from reaching the equilibrium position of the rutile phase. The system is in an highly non-equilibrium phase, the photoinduced phase. Both the lattice and the electronic properties continue to evolve separately over hundreds of picosecond, while the system thermalizes into the equilibrium metallic phase.

This experiment shows that the highly excited electronic distribution is at the origin of the photoinduced phase transition in VO_2. However we have neither demonstrated the nature of the gap nor given any response regarding the nature of the static, thermally driven transition.

3.3 High repetition rate measurements

The experiments presented in section 3.1 have been performed also at a repetition rate of 300 kHz. This section gives a qualitative comparison between the results obtained in the two data sets, although the fitting procedure for the high repetition rate is still not optimally concluded. Furthermore the results presented in this section are affected by a large error on the fluence determination, as discussed in section 2.3. We suppose that the camera used for measuring the spot size was forming an angle of $(40 \pm 10)°$. This implies that the spot area has to be corrected by dividing the original value by $\cos(40°)$ and the result obtained is $\mathscr{A} = 5(2) \times 10^{-5}\,\mathrm{cm}^2$. The corrected values of the fluence are in the range between 0.11(3) and 26(8) $\mathrm{mJ\,cm^{-2}}$.

The transient reflectivity traces are plotted as a function of time in figure 3.18. The

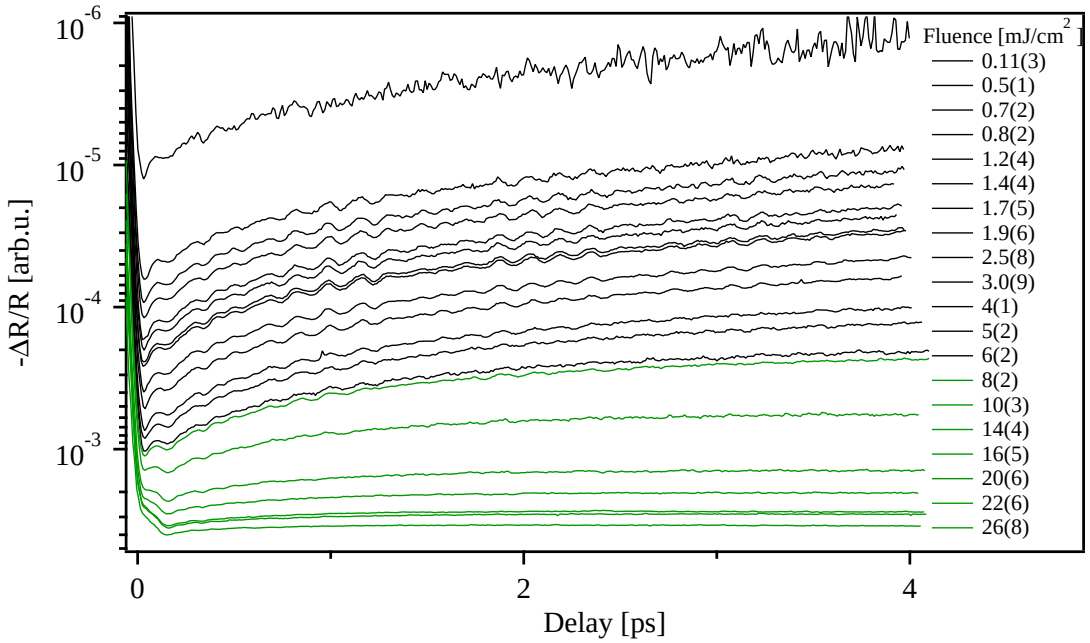

Figure 3.18: Time dependence of the reflectivity of VO_2 for different fluences. The values of the fluence are reported in the legend. The different colours indicate fluences below (black) and above (green) the threshold for the phase transition, according to the definition discussed in the text and in analogy to Ref. [CTS+01, KEH+07].

green traces indicate traces measured above fluence threshold and the black ones below. The traces follow the same qualitative behaviour as those presented in figure 3.1. They show a fast rise at time zero followed by a long decay that lasts over several picoseconds.

As discussed in section 3.1.1, we measure the change in reflectivity at 60 fs and 1 ps, since they are related to the electronic and lattice response of the system. Their fluence dependence is shown in figure 3.19(a) and matches the one found previously: the fast component amplitude grows linearly with fluence, while the slow component shows a critical behaviour.

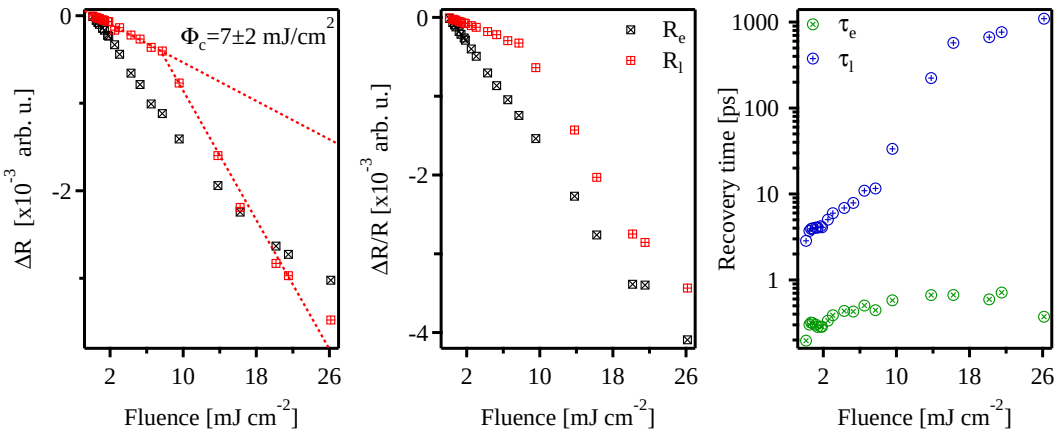

Figure 3.19: Fluence dependence for (a) the measured amplitudes at 60 fs and 1 ps, (b) the reflectivity amplitudes R_e and R_l resulting from the fit and (c) the decay times of the slow and fast components.

The value of the fluence threshold obtained in this case is $(7 \pm 2)\,\mathrm{mJ\,cm^2}$, since it is affected by the additional error due to the fluence evaluation. All traces have been fitted with Eq. (3.1), following the same procedure as described in section 3.1.1. Figure 3.19(b) and (c) present the results for the fit parameters. Panel (b) reports the values for R_e and R_l. As expected they follow the same trend as the amplitude at 60 fs and 1 ps and match the results presented in figure 3.4. Concerning the decays τ_e and τ_l, presented in figure (c), more discussion is needed. τ_l shows the same fluence

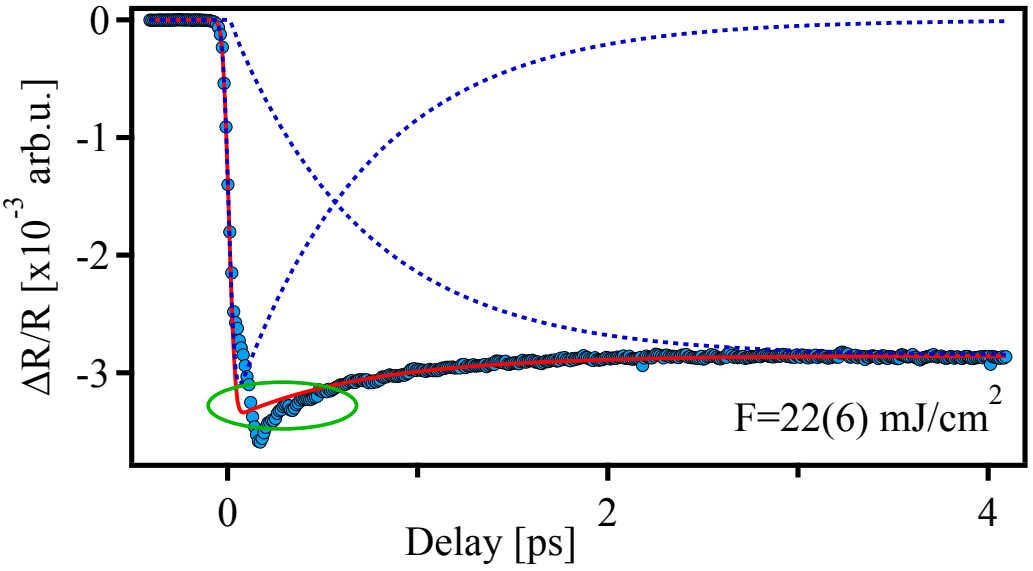

Figure 3.20: A sample fitting of the incoherent background for the high fluence regime at 300 kHz.

dependence as those calculated for the low repetition rate. Instead, τ_e seems to settle to a constant value for high fluences. This is an artifact of the fitting, which is yet to be optimized for this data set. The decay of the fast component is strongly related to its amplitude and to the fitting of the rising edge. Thus, the fit has to be carried on iteratively until all the connected parameters converge to a reasonable value. I clarify this concept discussing figure 3.20.

The figure shows the change in the relectivity measured at a fluence of $22(6)\,\mathrm{mJ\,cm^{-2}}$, thus in the high fluence regime. The red curve shows the results of the fit, while the dashed lines report the contribution of the fast and the slow component respectively. Focusing the attention to the area contained by the green circle one can see that the fit remains too low in the whole area. This derives from the fact that, at this values of the fluence, the oscillations overlap with the rising edge, influencing the result obtained for the amplitude of the fast component. In fact, if R_e were lower, then the resulting relaxation time would be longer. Instead, a too high R_e corresponds to an underestimation of the time necessary for the electronic sub-system to transfer the energy to the lattice. The fitting of the incoherent background, especially at high

fluences, has to be carried on iteratively, adressing at the beginning the three parts (rising edge, fast component and slow component) separately and then making all the parameters converge to a consistent picture. Figure 3.20 demonstrates that there is still room to improve the fitting routine for the 300 kHz data set. Since the evaluation of the coherent response is strongly related to the subtracted background, also the oscillatory traces have to be improved and therefore, are not presented in this thesis. Although no quantitative conclustion can be extracted from the data presented in this section, we show that there is a qualitative agreement between the two data sets.

4 Summary and Outlook

In this thesis the generation of coherent phonons was used as a tool for probing the changes in the lattice symmetries on an ultrafast timescale. We applied this technique to study the metal-to-insulator transition in vanadium dioxide, a transition which was a matter of controversy ever since its discovery in 1959. None of the previous theoretical or experimental work has been able to determine the nature of the transition and it is still discussed whether it is due to the lattice distortion or to the strong correlation effects in the *d* band.

We performed transient reflectivity measurements as a function of laser fluence, as described in section 3.1 and 3.1.1. The experiments have been carried out at two different repetition rates, 150 and 300 kHz, and the obtained results show the same qualitative behaviour in both cases. A threshold for the transition was determined at a critical fluence of $(6.5 \pm 0.4)\,\mathrm{mJ\,cm^{-2}}$. All transient reflectivity traces show an abrupt change at zero time delay and a subsequent recovery which lasts over several hundreds of picoseconds. The fluence dependence of the amplitude of the fast component, related to the electronic sub-system, was found to be linear over the whole range. On the other hand, the dependence of the slow component amplitude, which is related to the response of the lattice sub-system, showed an abrupt change at the fluence threshold. This implies a change in the dynamics and was considered a sign for the occurring phase transition.

Modulation of the signal due to coherent phonon excitation has been observed at all the fluences (cf. sec. 3.1.2). The analysis of the phonon dynamics demonstrates that, for excitation below the threshold, the five lowest A_g modes of the monoclinic phase of VO_2 are excited. The obtained frequency and damping rates are independent of the fluence, while the amplitudes grow monotonically over the whole range. Around the

threshold these modes suddenly disappear, disclosing a broader peak. The frequency of this peak was found to be 5.3(3) THz at low repetition rate, coinciding neither with the modes ot the monoclinc phase nor with those of the rutile phase. Furthermore, its amplitude and damping rate were found to be an order of magnitude larger than those of the monoclinic phase modes.

It is proposed that, above the fluence threshold, the electronic excitation suffices to distort the lattice potential in such a way that the restoring forces for the phonons of the monoclinic phase are no longer present. Thus, the modes which have been excited from the rising edge of the pulse are transformed into a superposition of the modes defined by the new potential, giving rise to the broad peak.

To support this model we have performed a pump-pump-probe experiment (see sec. 3.2). The system is brought into an excited state by the first pump pulse, while the pump-probe pair is used to measure the response of the system in the traditional way. Below the fluence threshold, we were able to perform coherent control of the monoclinic modes by re-pumping the system either in phase or out-of-phase with respect to the lattice oscillation considered. Above the fluence threshold, instead, no changes are detected, neither in the time dependent oscillatory traces nor in their Fourier transform. These results suggest a new description of the photoinduced phase transition: the ultrafast excitation of the electronic system induces a change in the symmetry of the potential, which in turn modifies the response of the lattice. The fact that the symmetry of the potential changes on the ultrafast timescale does not mean that the ions have reached the equilibrium position that fast. Indeed, the material is still in an highly non-equilibrium state and the evolution of the electronic and lattice properties continues over several hundreds of picoseconds, after which the system has thermalized in the high temperature rutile structure. Furthermore, showing that the highly excited electronic distribution is at the origin of the photoinduced phase transition, does not give any response regarding the nature of the static, temperature driven, transition.

The technique presented in this thesis opens new possibilities to the study of ultrafast

phase transitions, since it allows to measure the lattice properties with the same time resolution as the electronic ones. It can be applied to any material where an ultafast transition is related to a change in the Raman spectrum.

A The Hubbard model

The purpose of the Hubbard model was to determine the properties of the narrow energy bands, in which the free electron gas is not a good model and theories of correlations are needed in order to take into account the atomistic nature of the solid. Indeed it was found experimentally that the d-electrons of transition metals show both the characteristics of the band model and the atomic model and that the degree of atomic behaviour depends on the strength of the correlations.

A particular feature of the model is that the exact solution can be obtained in the limit of very weekly interacting electrons, where the band theory applies, as well as in the limit of strong interaction [Hub63, Hub64a].
For mathematical simplicity the model is applied to an s-band with two states per atom.

The model is developed in the Wannier functions basis given by:

$$\Phi(x) = N^{-\frac{1}{2}} \sum_k \Psi_k(x) \qquad \Psi_k(x) = N^{-\frac{1}{2}} \sum_i e^{ikR_i} \Phi(x - R_i) \,, \tag{A.1}$$

with R_i the atomic positions and N the number of atoms. In this basis the dynamics of the electrons of the band can be described by the following Hamiltonian:

$$\begin{aligned} H = \sum_{i,j} \sum_{\sigma} T_{ij} c^{\dagger}_{i\sigma} c_{j\sigma} + \frac{1}{2} \sum_{ijkl} \sum_{\sigma\sigma'} \left\langle ij \middle| \frac{1}{r} \middle| kl \right\rangle c^{\dagger}_{i\sigma} c^{\dagger}_{j\sigma'} c_{l\sigma'} c_{k\sigma} \\ - \sum_{ijkl} \sum_{\sigma} \left[2 \left\langle ij \middle| \frac{1}{r} \middle| kl \right\rangle - \left\langle ij \middle| \frac{1}{r} \middle| lk \right\rangle \right] \nu_{jl} c^{\dagger}_{i\sigma} c_{k\sigma} \,, \end{aligned} \tag{A.2}$$

where

$$T_{ij} = \frac{1}{N} \sum_k \epsilon_k e^{ik(R_i - R_j)} \tag{A.3a}$$

$$\left\langle ij \middle| \frac{1}{r} \middle| kl \right\rangle = e^2 \int \frac{\Phi^*(x - R_i)\Phi(x - R_k)\Phi^*(x' - R_j)\Phi(x' - R_l)}{|x - x'|} dx dx' \tag{A.3b}$$

The operators $c^{\dagger}_{i,\sigma}$, $c_{i,\sigma}$ and $n_{i,\sigma}$ are the creation, annihilation and number operator referring to an electron with spin σ in the orbital $\Phi(x - R_i)$ of the i-th atom.
In order to simplify the Hamiltonian, a crucial approximation is introduced: only interactions between electrons within the same atom are considered. Since the integral $\langle ii \big| 1/r \big| ii \rangle = I$, representing the interaction energy between electrons on the same atom, is much larger than all the inter-site integrals in (A.3b), they are neglected and the Hamiltonian becomes:

$$H = \sum_{i,j} \sum_{\sigma} T_{ij} c^{\dagger}_{i\sigma} c_{j\sigma} + \frac{1}{2} U \sum_{i,\sigma} n_{i\sigma} n_{i,-\sigma} - U \sum_{i,\sigma} \nu_{ii} n_{i\sigma} \tag{A.4}$$

Since $\nu_{ij} = N^{-1} \sum_k \nu_k e^{ik(R_i - R_j)}$, with ν_k being the occupation numbers of the states in the band, the last term reduces to a constant and is omitted. Defining

$$t_{ij} = N^{-1} \sum_k (\epsilon_k - T_0) e^{ik(R_i - R_j)} \tag{A.5a}$$

and

$$T_0 = N^{-1} \sum_k \epsilon_k \tag{A.5b}$$

and recalling the definition of T_{ij} from equation (A.3a), the Hamiltonian can be finally written as:

$$H = \sum_{i,j} \sum_{\sigma} t_{ij} c^{\dagger}_{i,\sigma} c_{j,\sigma} + T_0 \sum_{i,\sigma} n_{i,\sigma} + \frac{1}{2} U \sum_{i,\sigma} n_{i,\sigma} n_{i,-\sigma} \ , \tag{A.6}$$

corresponding to equation (1.1) of section 1.1.2. The term containing T_0 gives the atomic binding energy and the one containing U the interaction energy, while the terms with t_{ij} are responsible for the hopping of the electrons within the same lattice site.

In his paper from 1964, Hubbard developed the theory in terms of Green's functions and studied in detail the special case of a half-filled s-band with the same number of electrons for each spin, in which case the density of states has a parabolic form centered on T_0 with bandwith Δ [Hub64b]. He demonstrated that the nature of the solutions for the energy depends only on the ratio Δ/U.

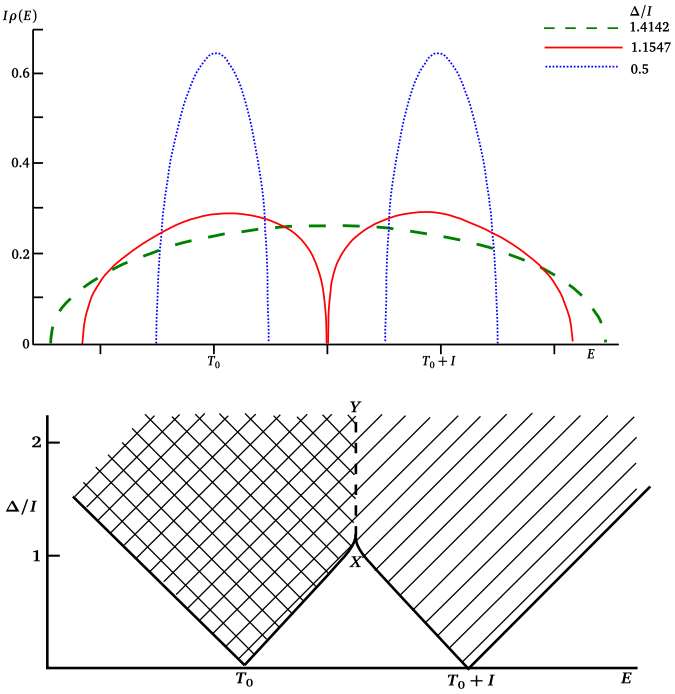

Figure A.1: Density of states as a function of the ratio Δ/U. (From [Hub64b])

Top: The density of states for three different ratios Δ/U, with $\Delta/U = 1.1547$ being the critical one.

Bottom: Boundaries of the bands as a function of Δ/U. Hatched region corresponds to non vanishing density of states.

Figure A.1(top) shows the density of states for three different values of the ratio while A.1(bottom) shows the spectrum more explicitly. The bands are plotted as a function of Δ/U and the hatched region corresponds to a non vanishing density of states. For the half-filled band case discussed in the model, the states will be, at the absolute zero temperature, occupied in the double-hatched region and empty in the rest. The point X indicates the critical ratio, which for this special case is $\Delta/U = 1.1547$. For smaller values there are one full and one empty band and the system is insulating, while for larger values the Fermi surface coincides with the XY line and the system is conductor.

B Design and realization of a continuously variable switchbox

Sometimes it is necessary to measure the properties of a material at a resonance. In order to do so it is useful to have a tunable laser source. In our lab, tunability is allowed by the multiple sources presented in section 2.1. When such a complex system is used, one of the issues is how to optimally distribute the power of the amplified oscillator beam between the different sources. Usually, this is done by using the appropriate set up of flip-mirrors and beam splitters. The biggest disadvantage of this kind of solution is that the power reaching each source is defined by the combination of beam splitters chosen. If some different value is needed, the whole optics has to be substituted. When I started designing the switchbox, we decided it would be useful to be able to tune the incoming power of each source depending on the needs of the performed experiment.

The solution we thought about, was to use a proper combination of thin film polarizers and $\lambda/2$ plates. Turning the $\lambda/2$ plate we can tune how much light is transmitted or reflected by the polarizer. One of the outputs, however, has a different polarization and a second waveplate has to be used to turn the polarization back to the original one.

Our goal was to have three different sources working on the same time, thus for having *p*-polarized light in every output of the switchbox, three waveplates and three polarizer filters were needed. The polarizers were purchased from the Altechna company and were specified for transmitting 98 % of the *p*-polarized light and reflect more than 85–90 % of the *s*-polarised light. All the substrates of the optics are made of fused silica, a material that does not absorb in the 800 nm range but causes positive GVD. To have all the outputs streched by the same GVD, it is therefore important that all the beams go through the same amount of fused silica.

There were two main challenges in the project. The first is that the commercial polarizers for the 800 nm range work under an angle of 72°. This implies the need of a complicated design, since the reflected beam forms an angle of 36° with the transmitted one, and we wanted the outputs to be all either parallel or perpendicular. The second problem is that the space between the RegA, the compressor and the OPA, where the switchbox is supposed to stay, was only of (32×60)cm. Furthermore the position of the input beam and two of the outputs was fixed by the surrounding table geometry. The Moreover, no effect had to be caused to the spectral and temporal shape of the pulse and the power loss had to be minimized.

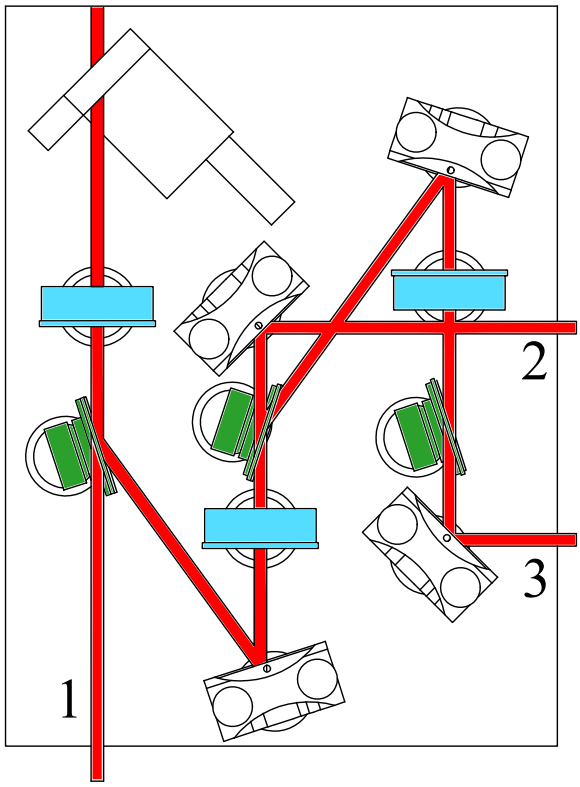

Figure B.1: The switchbox setup: in green the polarizer filters and in blue the $\lambda/2$ plates.

Figure B.1 shows the solution proposed. The $\lambda/2$ plates are shown in blue and the polarizers in green. A first waveplate changes the polarization of the originally *p*-polarized beam coming from the RegA, thus tuning the amount of light transmitted or reflected at the first polarizer. The transmitted light constitutes the first output. The reflected *s*-polarized light is deflected on an High Reflective (HR) mirror at an angle of incidence of 18° and sent to a second waveplate. This waveplate rotates the polarization of the beam again, so that a part of the light is *p*-polarized and can be transmitted by the second polarizer. The mechanism of the third output is the same. In this case we want all the remaining part of the beam to be transmitted and therefore the third waveplate always turns completely the polarization, from incoming *s*-polarized to *p*-

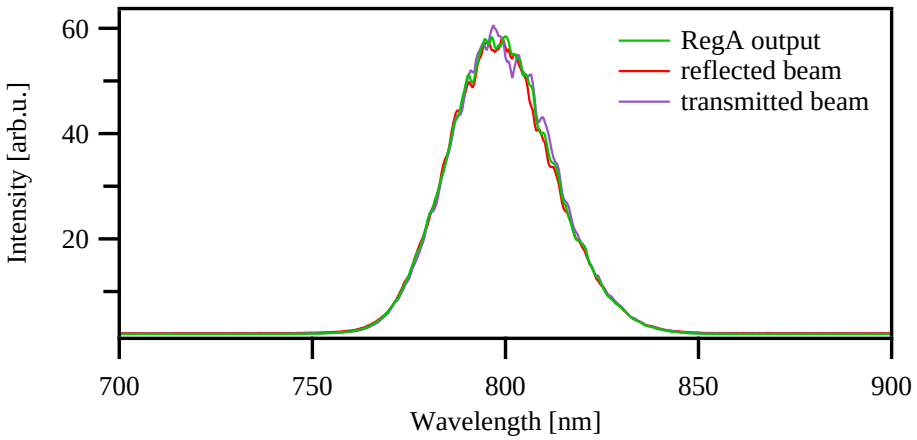

Figure B.2: The spectra of the reflected (*s*-polarized - red) and transmitted (*p*-polarized - violet) beams after a waveplate and a polarizer, compared to the spectrum of the RegA output. No major changes are visible.

polarized. The comfortable alignment was guaranteed by the use of top actuated mounts for all the optics.

The first test performed was on the quality of the output spectra, both in reflection and in transmission. The results, shown in Fig. B.2, demonstrate that no changes of the spectrum are caused by the optics.

To investigate whether the switchbox optics is causing any group velocity dispersion to the pulses, we have measured the output pulses of the switchbox using the FROG. The reference measurement for the RegA pulse alone is shown in section 2.3, where the duration obtained was of 39.8 fs. We have tested the effects of the first branch alone measuring the pulse transmitted by a single waveplate and polarizer. The obtained temporal FWHM was of 43.3 fs before compression and 40.2 fs after. To exclude that the reflection was causing higher orders of GVD, which are not compressable, we have measured the pulse duration for the second beam used alone. This corresponds to the situation were all the light is reflected at the first polarizer and transmitted at the second. The obtained results are 42 fs before compression and 40.4 fs after the optimization of the compressor. No tests were needed for the third beam since the

output ratio	angle 1	angle 2	angle 3	output 1 [%]	output 2 [%]	output 3 [%]	lost power [%]
1:0:0	0°	45°	45°	99.7	–	–	0.3
0:1:0	45°	45°	45°	5.9	88.7	0.4	5
0:0:1	45°	0°	45°	6.2	6.2	78.2	9.4
$\frac{1}{3}:\frac{2}{3}:0$	20.9°	45°	45°	33.4	61.7	–	4.9
$\frac{1}{3}:0:\frac{2}{3}$	20.9°	0°	45°	33.5	4.4	54.4	7.7
$\frac{1}{3}:\frac{1}{3}:\frac{1}{3}$	20.9°	21.5°	45°	33.6	29.7	29.7	7

Table B.1: Output power from each of the switchbox branches for given values of the angle. See text for description.

light goes in every output through the same amount of glass.

The setup has been tested for different distributions of power between the outputs in order to evaluate how much power loss we have in each case. The results are presented in table B.1. The first column reports the theoretical output ratio. The numbers label each branch of the switchbox and the corresponding $\lambda/2$ plate. A rotation angle of 0° corresponds to no change of the polarization and a rotation of 45° a complete change. The values reported for the angles have been experimentally obtained by measuring the desired output on the powermeter.

The results obtained stress an important point: there is always some power going in transmission. Furthermore, the more times the beam is reflected, the more power is lost. Therefore, no output, apart from the 3rd, can be blocked without loss of power. Thus, it is important to assign the beam coming out from the first and second output to the most frequently used sources or to those which can eventually require the full power disposable for a particular experiment.

C Derivation of some of the equations

Equation 1.8

The power Π_{abs} absorbed by a material can be calculated starting from the Poynting's theorem

$$\left\langle \frac{d\Pi_{abs}}{dV} \right\rangle = \langle \mathbf{J} \cdot \mathbf{E} \rangle \tag{C.1}$$

where $\mathbf{J}$ is the current, given by the sum of the currents due to the polarization and those due to free carriers, $\mathbf{J} = \mathbf{J}_p + \mathbf{J}_f$. From the current due to a variation in the polarization the following is obtained:

$\mathbf{J}_p = \frac{\partial \mathbf{P}}{\partial t}$ with $\mathbf{P} = P_0 e^{-i\omega t}$ and $\mathbf{E} = E_0 e^{-i\omega t}$

$$\Rightarrow \left\langle \frac{d\Pi_{abs}}{dV} \right\rangle = \frac{1}{2}\mathfrak{Re}\left[\mathbf{J_p} \cdot \mathbf{E}\right] = \frac{1}{2}\mathfrak{Re}\left[-i\omega P_0 e^{-i\omega t} \cdot E_0 e^{i\omega t}\right] =$$

inserting Eq. (1.4b)

$$= \frac{1}{2}\mathfrak{Re}\left[-i\omega\chi\epsilon_0 E_0 \cdot E_0^*\right] = \frac{1}{2}\omega\left|E_0\right|^2 \mathfrak{Re}\left[-i\epsilon_0\chi\right] =$$

$$= \frac{1}{2}\epsilon_0\omega\left|E_0\right|^2 \mathfrak{Im}(\epsilon)$$

The same calculation can be done for the current due to the free charges, which is given by $\mathbf{J_f} = \sigma\mathbf{E}$ and it follows

$$\left\langle \frac{d\Pi_{abs}}{dV} \right\rangle = \frac{1}{2}\mathfrak{Re}\left[\mathbf{J_f} \cdot \mathbf{E}\right] = \frac{1}{2}\mathfrak{Re}\left[\sigma E_0 e^{-i\omega t} \cdot E_0^* e^{i\omega t}\right] =$$

$$= \frac{1}{2}\left|E_0\right|^2 \mathfrak{Re}(\sigma)$$

Thus, Eq. (1.8) is obtained as

$$\left\langle \frac{d\Pi}{dV} \right\rangle = \langle \mathbf{J} \cdot \mathbf{E} \rangle = \frac{1}{2}\omega\left|E_0\right|^2 \mathfrak{Im}[\epsilon(\mathbf{x}, \omega)] + \frac{1}{2}\left|E_0\right|^2 \mathfrak{Re}[\sigma(\omega)]$$

Equation 1.14

Starting from the equation of motion for the harmonic oscillator with $\omega_0 = 0$

$$m\ddot{x} + m\gamma\dot{x} = -eE_0e^{-i\omega t} \tag{C.2}$$

where $E = E_0e^{-i\omega t}$ is the time dependence of the electric field,

$$m\dot{\mathrm{v}} + \frac{m\mathrm{v}}{\tau} + = -eE_0e^{-i\omega t} \tag{C.3}$$

is obtained by substituting $\dot{x} \rightarrow \mathrm{v}$, where v is the velocity of the electrons, and $\gamma \rightarrow \frac{1}{\tau}$, where τ is the damping time.

If the temporal dependence $\mathrm{v}(t)$ of the electron velocity is given by $\mathrm{v}(t) = \mathrm{v}_0e^{-i\omega t}$ Eq. (C.3) results in

$$\mathrm{v}(t) = -\frac{e}{m}\frac{\tau}{(1 - i\omega\tau)}E_0e^{-i\omega t}$$

Recalling that the current density j can be expressed as

$$j = -ne\mathrm{v} = \sigma E_0e^{-i\omega t} \tag{C.4}$$

equation (1.14) is obtained from

$$\begin{aligned} j &= -\frac{ne^2}{m}\frac{\tau}{(1 - i\omega\tau)}E_0e^{-i\omega t} = \sigma E_0e^{-i\omega t} \\ \Longrightarrow &\sigma(\omega) = \frac{ne^2\tau}{m}\frac{1}{1 - i\omega t} \end{aligned}$$

Bibliography

[AKP74] ANISIMOV, S.I. ; KAPELIOVICH, B.L. ; PEREL'MAN, T.L.: Electron emission from metal surfaces exposed to ultrashort laser pulses. In: *Sov. Phys. - JETP* 39 (1974), S. 375–377

[Bau07] BAUM, Peter: 4D visualization of transitional structures in phase transformations by electron diffraction. In: *science* 318 (2007), S. 788. http://dx.doi.org/10.1126/science.1147724. – DOI 10.1126/science.1147724

[BBW+96] BECKER, Michael F. ; BUCKMAN, A. B. ; WALSER, Rodger M. ; LÉPINE, Thierry ; GEORGES, Patrick ; BRUN, Alain: Femtosecond laser excitation dynamics of the semiconductor-metal phase transition in VO_2. In: *Journal of Applied Physics* 79 (1996), Nr. 5, 2404-2408. http://dx.doi.org/10.1063/1.361167. – DOI 10.1063/1.361167

[Boy08] BOYD, Robert W.: *Nonlinear Optics*. Academic Press, 2008

[BSB81] BIANCONI, A. ; STIZZA, S. ; BERNARDINI, R.: Critical behavior of the plasmon resonance at the metal-insulator transition in VO_2. In: *Phys. Rev. B* 24 (1981), Oct, Nr. 8, S. 4406–4411. http://dx.doi.org/10.1103/PhysRevB.24.4406. – DOI 10.1103/PhysRevB.24.4406

[BV37] BOER, J H. ; VERWEY, E J W.: Semi-conductors with partially and with completely filled 3 d -lattice bands. In: *Proceedings of the Physical Society* 49 (1937), Nr. 4S, 59. http://stacks.iop.org/0959-5309/49/i=4S/a=307

[CDC+04] CAVALLERI, A. ; DEKORSY, Th. ; CHONG, H. H. W. ; KIEFFER, J. C. ; SCHOENLEIN, R. W.: Evidence for a structurally-driven insulator-to-metal transition in $VO2$: A view from the ultrafast timescale. In: *Phys. Rev. B* 70 (2004), Oct, Nr. 16, S. 161102. http://dx.doi.org/10.1103/PhysRevB.70.161102. – DOI 10.1103/PhysRevB.70.161102

[CK10] CHAE, Byung G. ; KIM, Hyun T.: Effects of W doping on the metal-insulator transition in vanadium dioxide film. In: *PHYSICA B-CONDENSED MATTER* 405 (2010), JAN 15, Nr. 2, S. 663–667. http://dx.doi.org/{10.1016/j.physb.2009.09.083}. – DOI 10.1016/j.physb.2009.09.083. – ISSN 0921–4526

[Coh97] COHERENT, INC. (Hrsg.): *RegA Model 9000 Laser Operator's Manual*. Coherent, Inc., 1997

[Coh07] COHERENT, INC (Hrsg.): *Micra Laser Operator's Manual*. Coherent, Inc, 2007

[CTS+01] CAVALLERI, A. ; TÓTH, Cs. ; SIDERS, C. W. ; SQUIER, J. A. ; RÁKSI, F. ; FORGET, P. ; KIEFFER, J. C.: Femtosecond Structural Dynamics in VO2 during an Ultrafast Solid-Solid Phase Transition. In: *Phys. Rev. Lett.* 87 (2001), Nov, Nr. 23, S. 237401. http://dx.doi.org/10.1103/PhysRevLett.87.237401. – DOI 10.1103/PhysRevLett.87.237401

[EPS63] EHRENREICH, H. ; PHILIPP, H. R. ; SEGALL, B.: Optical Properties of Aluminum. In: *Phys. Rev.* 132 (1963), Dec, Nr. 5, S. 1918–1928. http://dx.doi.org/10.1103/PhysRev.132.1918. – DOI 10.1103/PhysRev.132.1918

[FMG84] FORK, R. L. ; MARTINEZ, O. E. ; GORDON, J. P.: Negative dispersion using pairs of prisms. In: *Opt. Lett.* 9 (1984), Nr. 5, 150–152. http://ol.osa.org/abstract.cfm?URI=ol-9-5-150

[Gat07] GATTI, Matteo: *Correlation effects in valence-electron spectroscopy of*

transition-metal oxides : many-body perturbation theory and alternative approaches, ÉCOLE POLYTECHNIQUE, Diss., December 2007

[GBOR07] GATTI, Matteo ; BRUNEVAL, Fabien ; OLEVANO, Valerio ; REINING, Lucia: Understanding Correlations in Vanadium Dioxide from First Principles. In: *Phys. Rev. Lett.* 99 (2007), Dec, Nr. 26, S. 266402. http://dx.doi.org/10.1103/PhysRevLett.99.266402. – DOI 10.1103/PhysRevLett.99.266402

[GFM84] GORDON, JP ; FORK, RL ; MARTINEZ, OE: Negative Dispersion From Prisms. In: *Journal Of The Optical Society Of America B-Optical Physics* 1 (1984), Nr. 3, 437. http://www.opticsinfobase.org/DirectPDFAccess/DD6476F7-BDB9-137E-C85FC1ECFD97A5E6_8213.pdf?da=1&id=8213&seq=0. – ISSN 0740–3224

[Goo71] GOODENOUGH, John B.: The two components of the crystallographic transition in VO2. In: *Journal of Solid State Chemistry* 3 (1971), Nr. 4, 490 - 500. http://dx.doi.org/DOI:10.1016/0022-4596(71)90091-0. – DOI DOI: 10.1016/0022–4596(71)90091–0. – ISSN 0022–4596

[HBS+10] HELLMANN, S. ; BEYE, M. ; SOHRT, C. ; ROHWER, T. ; SORGENFREI, F. ; REDLIN, H. ; KALLÄNE, M. ; MARCZYNSKI-BÜHLOW, M. ; HENNIES, F. ; BAUER, M. ; FÖHLISCH, A. ; KIPP, L. ; WURTH, W. ; ROSSNAGEL, K.: Ultrafast Melting of a Charge-Density Wave in the Mott Insulator $1T - TaS_2$. In: *Phys. Rev. Lett.* 105 (2010), Oct, Nr. 18, S. 187401. http://dx.doi.org/10.1103/PhysRevLett.105.187401. – DOI 10.1103/PhysRevLett.105.187401

[Hub63] HUBBARD, J.: Electron Correlations in Narrow Energy Bands. In: *Proceedings of the Royal Society of London. Series A. Mathematical and Physical Sciences* 276 (1963), Nr. 1365, 238-257. http://dx.doi.org/10.1098/rspa.1963.0204. – DOI 10.1098/rspa.1963.0204

[Hub64a] HUBBARD, J.: Electron Correlations in Narrow Energy Bands. II. The Degenerate Band Case. In: *Proceedings of the Royal Society of London. Series A. Mathematical and Physical Sciences* 277 (1964), Nr. 1369, 237-259. http://dx.doi.org/10.1098/rspa.1964.0019. – DOI 10.1098/rspa.1964.0019

[Hub64b] HUBBARD, J.: Electron Correlations in Narrow Energy Bands. III. An Improved Solution. In: *Proceedings of the Royal Society of London. Series A. Mathematical and Physical Sciences* 281 (1964), Nr. 1386, 401-419. http://dx.doi.org/10.1098/rspa.1964.0190. – DOI 10.1098/rspa.1964.0190

[IFT98] IMADA, Masatoshi ; FUJIMORI, Atsushi ; TOKURA, Yoshinori: Metal-insulator transitions. In: *Rev. Mod. Phys.* 70 (1998), Oct, Nr. 4, S. 1039–1263. http://dx.doi.org/10.1103/RevModPhys.70.1039. – DOI 10.1103/RevModPhys.70.1039

[Jon34] JONES, H.: Applications of the Bloch Theory to the Study of Alloys and of the Properties of Bismuth. In: *Proceedings of the Royal Society of London. Series A - Mathematical and Physical Sciences* 147 (1934), Nr. 861, 396-417. http://dx.doi.org/10.1098/rspa.1934.0224. – DOI 10.1098/rspa.1934.0224

[Kam06] KAMPFRATHKAM06, Tobias: *Charge Carrier Dynamics in Solids and Gases Observed by Time-Resolved Terahertz Spectroscopy*, Freie Universität Berlin, Diss., 2006. http://users.physik.fu-berlin.de/~femtoweb/newfemtos/cgi-bin/ax.cgi?../docs/thesis/Dissertation_Kampfrath.pdf

[KEH+07] KÜBLER, C. ; EHRKE, H. ; HUBER, R. ; LOPEZ, R. ; HALABICA, A. ; HAGLUND, R. F. ; LEITENSTORFER, A.: Coherent Structural Dynamics and Electronic Correlations during an Ultrafast Insulator-to-Metal Phase Transition in

*VO*2. In: *Phys. Rev. Lett.* 99 (2007), Sep, Nr. 11, S. 116401. http://dx.doi.org/10.1103/PhysRevLett.99.116401. – DOI 10.1103/PhysRevLett.99.116401

[KHH+06] KOETHE, T. C. ; HU, Z. ; HAVERKORT, M. W. ; SCHÜSSLER-LANGEHEINE, C. ; VENTURINI, F. ; BROOKES, N. B. ; TJERNBERG, O. ; REICHELT, W. ; HSIEH, H. H. ; LIN, H.-J. ; CHEN, C. T. ; TJENG, L. H.: Transfer of Spectral Weight and Symmetry across the Metal-Insulator Transition in VO_2. In: *Phys. Rev. Lett.* 97 (2006), Sep, Nr. 11, S. 116402. http://dx.doi.org/10.1103/PhysRevLett.97.116402. – DOI 10.1103/PhysRevLett.97.116402

[Kit66] KITTEL, Charles: *Introduction To Solid State Physics*. 3rd. John Wiley & Sons, 1966

[KLK+06] KIM, Hyun-Tak ; LEE, Yong W. ; KIM, Bong-Jun ; CHAE, Byung-Gyu ; YUN, Sun J. ; KANG, Kwang-Yong ; HAN, Kang-Jeon ; YEE, Ki-Ju ; LIM, Yong-Sik: Monoclinic and Correlated Metal Phase in $VO2$ as Evidence of the Mott Transition: Coherent Phonon Analysis. In: *Phys. Rev. Lett.* 97 (2006), Dec, Nr. 26, S. 266401. http://dx.doi.org/10.1103/PhysRevLett.97.266401. – DOI 10.1103/PhysRevLett.97.266401

[LBB06] LIANG, Shi-Dong ; BAI, Yi-Hong ; BENG, Bo: Peierls instability and persistent current in mesoscopic conducting polymer rings. In: *Phys. Rev. B* 74 (2006), Sep, Nr. 11, S. 113304. http://dx.doi.org/10.1103/PhysRevB.74.113304. – DOI 10.1103/PhysRevB.74.113304

[LL60] LANDAU, L.D. ; LIFSHITZ, E.M.: *Course of theoretical physics*. Bd. 8: *Electrodynamics of continuous media*. Pergamon press, 1960

[Mor59] MORIN, F. J.: Oxides Which Show a Metal-to-Insulator Transition at the Neel Temperature. In: *Phys. Rev. Lett.* 3 (1959), Jul, Nr. 1, S. 34–36. http://dx.doi.org/10.1103/PhysRevLett.3.34. – DOI 10.1103/PhysRevLett.3.34

[Mot61] MOTT, N. F.: The transition to the metallic state. In: *Philosophical Magazine* 6 (1961), S. 287–309. http://dx.doi.org/10.1080/14786436108243318. – DOI 10.1080/14786436108243318

[MP37] MOTT, N F. ; PEIERLS, R: Discussion of the paper by de Boer and Verwey. In: *Proceedings of the Physical Society* 49 (1937), Nr. 4S, 72. http://stacks.iop.org/0959-5309/49/i=4S/a=308

[NH08] NAG, Joyeeta ; HAGLUND, R.F. J.: Synthesis of vanadium dioxide thin films and nanoparticles. In: *Journal of physics: Condensed Matter* 20 (2008), S. 264016. http://dx.doi.org/10.1088/0953-8984/20/26/264016. – DOI 10.1088/0953–8984/20/26/264016

[Oxf05] OXFORD INSTRUMENTS (Hrsg.): *OptistatCF-V Product guide*. Oxford Instruments, 2005. http://www.oxford-instruments.com/products/low-temperature/opticaland-spectroscopy/optistatcf-v/Pages/optistatcf-v.aspx

[Pei55] PEIERLS, R. E.: *Quantum theory of solids*. Oxford : Clarendon Pr., 1955

[Pei91] PEIERLS, R.: *More Surprises in Theoretical Physics*. Princeton Univ. Pr., 1991 (Princeton series in physics)

[PLL+08] PERFETTI, L ; LOUKAKOS, P A. ; LISOWSKI, M ; BOVENSIEPEN, U ; WOLF, M ; BERGER, H ; BIERMANN, S ; GEORGES, A: Femtosecond dynamics of electronic states in the Mott insulator 1T-TaS 2 by time resolved photoelectron spectroscopy. In: *New Journal of Physics* 10 (2008), Nr. 5, 053019. http://stacks.iop.org/1367-2630/10/i=5/a=053019

[PV10] PERGAMENT, Alexander ; VELICHKO, Andrei: Metal-insulator transition in thin films of vanadium dioxide: The problem of dimensional effects. In: *THIN SOLID FILMS* 518 (2010), JAN 1, Nr. 6, S. 1760–1762. http://dx.doi.org/{10.1016/j.tsf.2009.11.085}. – DOI 10.1016/j.tsf.2009.11.085. – ISSN 0040–6090

[PYS02] PETROV, G. I. ; YAKOVLEV, V. V. ; SQUIER, J. A.: Nonlinear optical microscopy analysis of ultrafast phase transformation in vanadium dioxide. In: *Opt. Lett.* 27 (2002), Nr. 8, 655–657. http://ol.osa.org/abstract.cfm?URI=ol-27-8-655

[Rad06] RADU, Ilie E.: *Ultrafast Electron, Lattice and Spin Dynamics on Rare-Earth Metal Surfaces investigated with linear and nonlinear optical techniques*, Freie UniversitÃ¤t Berlin, Diss., 2006. http://www.diss.fu-berlin.de/diss/receive/FUDISS_thesis_000000002216

[RB71] ROACH, W. R. ; BALBERG, I.: Optical induction and detection of fast phase transition in VO2. In: *Solid State Communications* 9 (1971), Nr. 9, 551 - 555. http://dx.doi.org/DOI:10.1016/0038-1098(71)90144-X. – DOI DOI: 10.1016/0038–1098(71)90144–X. – ISSN 0038–1098

[RSP+10] RADU, I. ; STAMM, C. ; PONTIUS, N. ; KACHEL, T. ; RAMM, P. ; THIELE, J.-U. ; DÜRR, H. A. ; BACK, C. H.: Laser-induced generation and quenching of magnetization on FeRh studied with time-resolved x-ray magnetic circular dichroism. In: *Phys. Rev. B* 81 (2010), Mar, Nr. 10, S. 104415. http://dx.doi.org/10.1103/PhysRevB.81.104415. – DOI 10.1103/PhysRevB.81.104415

[RTD+07] RINI, Matteo ; TOBEY, Ra'anan ; DEAN, Nicky ; ITATANI, Jiro ; TOMIOKA, Yasuhide ; TOKURA, Yoshinori ; SCHOENLEIN, Robert W. ; CAVALLERI, Andrea: Control of the electronic phase of a manganite by mode-selective vibrational excitation. In: *Nature* 449 (2007), September, Nr. 7158, 72–74. http://dx.doi.org/10.1038/nature06119. – ISSN 0028–0836

[Sch02] SCHILBE, Peter: Raman scattering in VO2. In: *Physica B: Condensed Matter* 316-317 (2002), 600 - 602. http://dx.doi.org/DOI:10.1016/S0921-4526(02)00584-7. – DOI DOI: 10.1016/S0921–4526(02)00584–7. – ISSN 0921–4526

[SCH+04] SOLTANI, M. ; CHAKER, M. ; HADDAD, E. ; KRUZELECKY, R. V. ; MARGOT, J.: Effects of Ti–W codoping on the optical and electrical switching of vanadium dioxide thin films grown by a reactive pulsed laser deposition. In: *Applied Physics Letters* 85 (2004), Nr. 11, 1958-1960. http://dx.doi.org/10.1063/1.1788883. – DOI 10.1063/1.1788883

[Seg61] SEGALL, Benjamin: Energy Bands of Aluminum. In: *Phys. Rev.* 124 (1961), Dec, Nr. 6, S. 1797–1806. http://dx.doi.org/10.1103/PhysRev.124.1797. – DOI 10.1103/PhysRev.124.1797

[SJ64] SOUERS, P. C. ; JURA, G.: Negative Temperature Coefficient of Resistance in Bismuth I. In: *Science* 143 (1964), S. 467–469

[SKM02] STEVENS, T. E. ; KUHL, J. ; MERLIN, R.: Coherent phonon generation and the two stimulated Raman tensors. In: *Phys. Rev. B* 65 (2002), Mar, Nr. 14, S. 144304. http://dx.doi.org/10.1103/PhysRevB.65.144304. – DOI 10.1103/PhysRevB.65.144304

[Tre00] TREBINO, Rick: *Frequency-Resolved Optical Gating: The measurement of ultrashort laser pulses*. Kluwer Academic Publishers, 2000

[TT01] TAYAGAKI, Takeshi ; TANAKA, Koichiro: Photoinduced Phase Transition to a New Macroscopic Spin-Crossover-Complex Phase. In: *Phys. Rev. Lett.* 86 (2001), Mar, Nr. 13, S. 2886–2889. http://dx.doi.org/10.1103/PhysRevLett.86.2886. – DOI 10.1103/PhysRevLett.86.2886

[VBB68] VERLEUR, Hans W. ; BARKER, A. S. ; BERGLUND, C. N.: Optical Properties of VO_2 between 0.25 and 5 eV. In: *Phys. Rev.* 172 (1968), Aug, Nr. 3, S. 788–798. http://dx.doi.org/10.1103/PhysRev.172.788. – DOI 10.1103/PhysRev.172.788

[VS83] VARMA, C. M. ; SIMONS, A. L.: Strong-Coupling Theory of Charge-Density-Wave Transitions. In: *Phys. Rev. Lett.* 51 (1983), Jul, Nr. 2, S. 138–

141. http://dx.doi.org/10.1103/PhysRevLett.51.138. – DOI 10.1103/PhysRevLett.51.138

[Weg09] WEGKAMP, D: *Schnelle Elektronendynamiken an Grenzflächen untersucht mit einer NOPA-basierenden Femtosekunden-Lichtquelle*. http://users.physik.fu-berlin.de/~wegkamp/Diplomarbeit.pdf. Version: 2009

[Wig34] WIGNER, E.: On the Interaction of Electrons in Metals. In: *Phys. Rev.* 46 (1934), Dec, Nr. 11, S. 1002–1011. http://dx.doi.org/10.1103/PhysRev.46.1002. – DOI 10.1103/PhysRev.46.1002

[Wil31] WILSON, A. H.: The Theory of Electronic Semi-Conductors. In: *Proceedings of the Royal Society of London. Series A* 133 (1931), Nr. 822, 458-491. http://dx.doi.org/10.1098/rspa.1931.0162. – DOI 10.1098/rspa.1931.0162

[ZM75] ZYLBERSZTEJN, A ; MOTT, Nf: Metal-insulator transition in vanadium dioxide. In: *Physical Review B* 11 (1975), Nr. 11, S. 4383–4395. http://dx.doi.org/10.1103/PhysRevB.11.4383. – DOI 10.1103/PhysRevB.11.4383. – ISSN 0163–1829

Aknowledgments

At this point I would like to thank all the persons who made this thesis possible.

In first place I thank Julia Stähler for being such a great supervisor, transmitting me not only scientific knowledge but also all the passion she has for her job. Furthermore I am grateful for the support she gave me for getting over moments of discouragement and also for the atmosphere she was able to create in the group, being not only a leader but also a friend. Definitely the champions league games watched together and the celebration beers have contributed to make me feel at home. Lastly I don't want to forget how helpful it can be, sometimes, to have a woman in the group.

I am certainly indebted with Martin Wolf for giving me the opportunity to work in his group. Moving to Berlin was definitely worth it.

Jan-Christoph Deinert, Sebastian Hagen, Simon Wall and Daniel Wegkamp have contributed to make this year a really pleasant one, creating the perfect atmosphere inside and outside the lab. In particular my gratitude goes to Simon and Daniel, who I shared the experiment with, for being always ready to explain things once again.

To the rest of the group a big thanks for being always willing to help me with all the small practical issues and to show me the meanders of the institute.

Also Daniele, Fabio, Francesca and Rosaria have somehow contributed to this thesis by being my piece of Italy in Berlin. I will never forget our lasagne, ravioli and tiramisú, or our dancing and joking and singing. Mille grazie!

I owe a sign of esteem and gratitude to Niccoló and Giovanni, for sharing with me all the joys and pains of the first two years of university as well as a lot of pleasant evenings

and tasty dinners. I thank Niccoló for all the never-ending afternoons spent together in the lab course and on theoretical physics or mathematics exercises. Giovanni, for introducing me to the world of computers: from my first C++ "hello world" program to the first time I was able to install and configure linux all alone.

My girls, the two Valentina, the two Elisa, Sofia and Erica, have played a big role, probably without even noticing. They have always been at my side, even if 1500 km are now separating us. There are no enough words to thank them.

Spasibo Misha. For the always useful remarks and corrections, for teaching me the appropriate use of serifs, for having my same taste regarding meat and for allowing me to behave, sometimes, as a kid.

Last but not least, I am enormously grateful to my parents and my family, who have always supported me, both economically and emotionally. Among them a special mention goes to my grandmother who is always a model for me. Most of the goals I have achieved in the last years would have never been possible without her example.

I want to express my parents my great appreciation for having accepted all my decisions regarding my studies and my work, thereby demonstrating once again how much they believed in me. I hope I have been able to reward for their trust.

Eidesstattliche Erklärung gemäß §17 Abs. 7 DPO

Ich versichere hiermit an Eides Statt, dass diese Arbeit von niemand anderem als meiner Person verfasst worden ist. Alle verwendeten Zitate sind als solche kenntlich gemacht und die entsprechenden Quellen sind im Literaturverzeichnis angegeben. Die Arbeit wurde bisher in gleicher oder ähnlicher Form keiner anderen Prüfungskommission vorgelegt und auch nicht veröffentlicht.